DEFECT STRUCTURES, PHASE RELATIONS AND PHASE TRANSFORMATIONS OF LOW TEMPERATURE IRON SULFIDE COMPOUNDS

by

THAO ANH NGUYEN

S.B., Mathematics and Physics, Boston College
(1981)

SUBMITTED IN PARTIAL FULFILLMENT OF THE
REQUIREMENTS OF THE DEGREE OF

DOCTOR OF PHILOSOPHY

IN MATERIALS SCIENCE

at the

MASSACHUSETTS INSTITUTE OF TECHNOLOGY

June 1987

Signature redacted

Signature of Author_____
Department of Materials Science and Engineering
May 1, 1987

Signature redacted

Certified by_____
Linn W. Hobbs
Thesis Supervisor

Signature redacted

Accepted by_____
Samuel M. Allen
Chairman, Departmental Committee on Graduate Students

DEFECT STRUCTURES, PHASE RELATIONS AND PHASE TRANSFORMATIONS OF LOW TEMPERATURE IRON SULFIDE COMPOUNDS

by

THAO ANH NGUYEN

Submitted to the Department of Materials Science and Engineering
on May 1, 1987 in partial fulfillment of the requirements for
the Degree of Doctor of Philosophy in Materials Science

ABSTRACT

The structures, phase relations and phase transformations of pyrrhotite, $Fe_{1-x}S$, in the composition and temperature ranges from FeS to $Fe_{0.92}S$ and from 298 K to 550 K have been investigated by a series of *in situ* heating and cooling experiments, conventional and high resolution transmission electron microscopies and electron and x-ray diffraction.

A phase diagram has been constructed from the results of the *in situ* heating experiments and electron and x-ray diffraction studies. This phase diagram differs significantly from the phase diagrams reported in the literature. We have found two solvuses in the composition range of FeS and $Fe_{0.92}S$. The first solvus separates the $Fe_{1-x}S$ (1C) phase and a two-phase mixture of FeS (2C) and $Fe_{1-x}S$ (1C). The second solvus demarcates the 1C and 1C phases. The 1C phase has an incommensurate superstructure. The positions of the superstructure reflections of the 1C phase vary with composition and temperature. The iron vacancies in the 1C phase appear to order locally in the iron planes.

From a series of *in situ* cooling experiments, the phase transformation mechanism of reaction $Fe_{1-x}S$ (1C) $\longrightarrow$ FeS (2C) + $Fe_{1-x'}S$ (1C) (x < x') has been found to be nucleation and growth. The growth rate of the length of lenticular-shape FeS precipitates obeys a linear rate law. The growth rate appears to be controlled by the interfacial reaction. The growth rate of the side walls of the FeS (2C) precipitates is linear initially and eventually becomes parabolic. The growth mechanism in the parabolic regime appears to be a diffusion-controlled reaction. The dependency of the growth rate on undercooling agrees qualitatively with that predicted by the continuous growth model.

High resolution transmission electron microscopy has been used to study the structure of the FeS(2C)/$Fe_{1-x}S$(1C) interface. The FeS/$Fe_{1-x}S$ interface is coherent. The tip of the FeS precipitate is almost atomically sharp. Away from the tip, the FeS/$Fe_{1-x}S$ interface is smooth.

Diffraction patterns of $Fe_{1-x}S$ during the initial stage of the phase transformation $Fe_{1-x}S$ (1C) $\longrightarrow$ FeS (2C) + $Fe_{1-x'}S$ (1C) (x < x') have been found to be

either identical or similar to that of the "intermediate" pyrrhotite. This suggests that the "intermediate" $Fe_{1-x}S$ compounds might be artifactual.

Thesis Supervisor: Professor Linn W. Hobbs
Professor of Ceramics and Materials Science

TABLE OF CONTENTS   Page

LIST OF FIGURES

LIST OF TABLES

14

ACKNOWLEDGEMENTS

CHAPTER 1

INTRODUCTION

Pyrrhotite, $Fe_{1-x}S$, is a series of iron sulfide compounds with composition ranging from FeS to $Fe_{0.875}S$ (Figure 1.1). Beside being an important system in mineralogy, pyrrhotite is very well known for its ability to accommodate a large concentration of iron vacancies, and for the fact that the iron vacancies order and form superstructures at low temperature. Pyrrhotite is also known to possess intriguing magnetic and electrical properties which are physically interesting as well as industrially important (Ward 1970).

The low temperature phase relations of pyrrhotite have been investigated extensively over the past six decades. Despite these efforts, conflicting reports on the stability of low temperature phases, the phase transformation mechanisms and major disagreements among proposed phase diagrams remain unresolved. Many of the disagreements have been attributed to the uncertainty in composition and thermal history of the materials studied, slow diffusion kinetics and complex phase relations which gives rise to microscopic inhomogeneities in defect structures and intergrowth. The latter is compounded by the spatial limitation of the investigative tools so far employed which, at best, average over significant inhomogeneities in the defect structures.

A systematic study of the phase relations, phase transformations and defect structures of $Fe_{1-x}S$ crystals in the composition range of FeS to $Fe_{0.875}S$ has been carried out in order to:

1) resolve controversial and problematic aspects of the low temperature phase relations.

2) gain detailed information on the extent and modes of iron vacancy ordering.

3) gain information on the phase transformation mechanisms to better understand the thermodynamic and kinetic aspects in relation to the microstructures of the $Fe_{1-x}S$ crystals.

This study has been carried out using synthetic and natural $Fe_{1-x}S$ crystals. Investigations of the phase relations, phase transformations and defect structures were conducted through the use of conventional and high resolution transmission electron microscopies, *in situ* heating and cooling experiments, and x-ray diffraction.

This thesis is organized into eight chapters. Chapter 2 provides the background and reviews relevant literature. Chapter 3 describes the major issues addressed by this thesis. The experimental procedure and data analysis are delineated in Chapters 4 and 5. Chapters 6 and 7 present the experimental results and discussion. Chapter 8 summarizes the major conclusions. Chapter 9 suggests topics for future research.
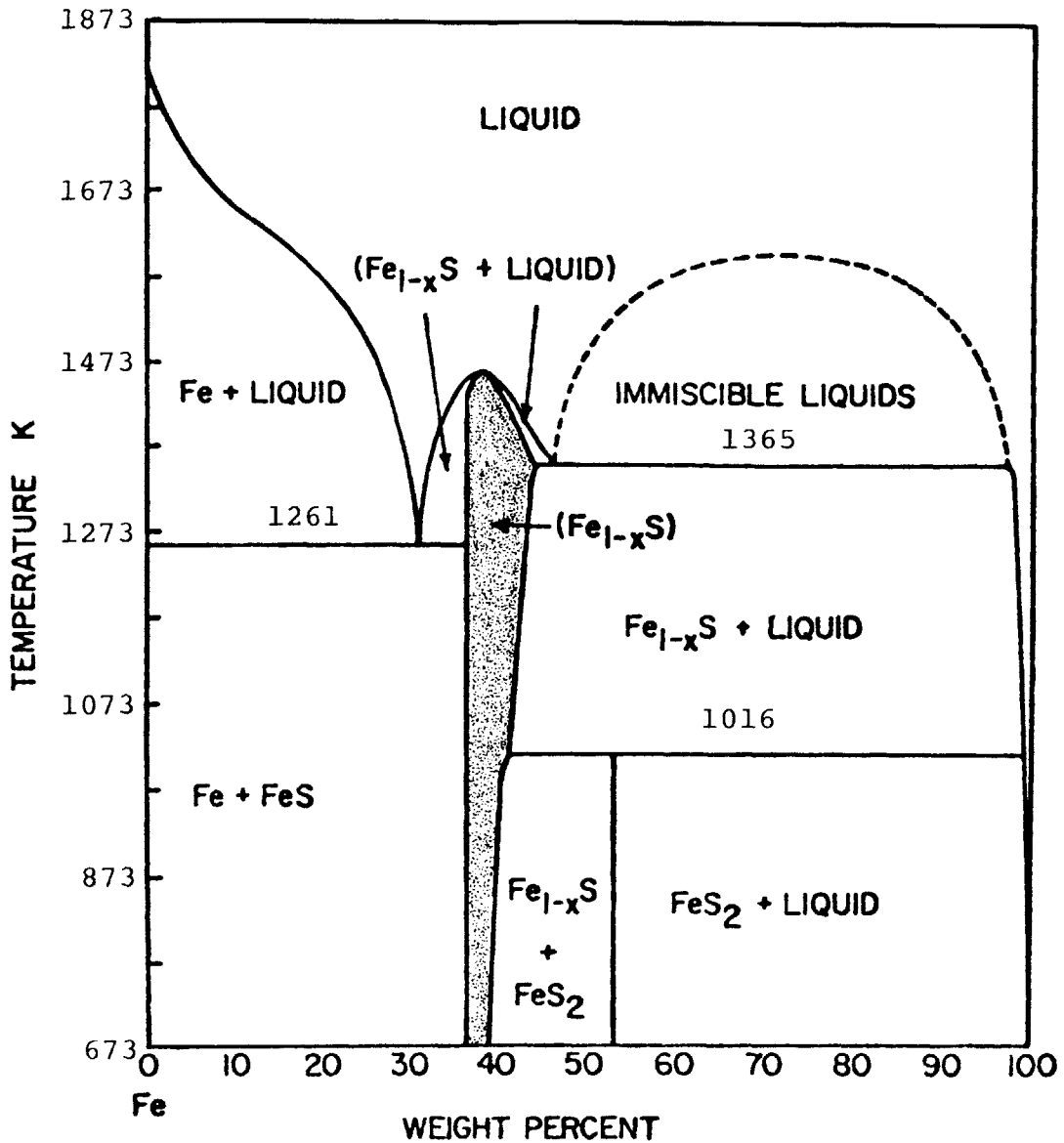
Figure I.I. Relations among condensed phases in the Fe–S system above 673 K. This thesis investigated the phase relations of Fe$_{1-x}$S, 0<x<0.125, (shaded area) at temperatures below 673 K. (From Ribbe, 1976, after Kullerud, 1967).

References

Scott, S. D. in _Sulfide Mineralogy_, P. H. Ribbe editor, BookCrafters Inc. Chelsea, Michigan (1982).

Ward, J. C., Rev. Pure Appl. Chem. _20_, 175-206 (1970).

CHAPTER 2

BACKGROUND AND SURVEY OF RELEVANT LITERATURE

This chapter begins with a description of the NiAs structure, the parent structure of all iron sulfide compounds. Important items of the nomenclature and notation convention will be dealt with next. The bulk of the chapter is then devoted to the survey of relevant literature. This includes a review of

1) phase relations of iron sulfide compounds in the composition range of FeS to $Fe_{0.875}S$.

2) structures of the two end members, FeS and $Fe_{0.875}S$.

3) structures of "intermediate" iron sulfide compounds.

This chapter will end with brief discussions of the magnetic properties and diffusion kinetics that are relevant to this thesis.

2.1 THE NiAs STRUCTURE

Iron sulfide compounds of composition $Fe_{1-x}S$, $0 < x < 0.125$, have a basic NiAs structure (Alsen 1925, Figure 2.1) in which the electro-negative atoms form an almost close-packed hexagonal sublattice and the electro-positive atoms occupy the octahedral interstices in the close-packed array. A special feature of the NiAs structure is that FeS_6 octahedra share faces along the c-axis and share edges normal to the c-axis (Figure 2.2). FeS_4 tetrahedra also share faces forming trigonal bipyramids. These unique features suggest the possibilities of : (1) large deviation from stoichiometry due to the low ionicity. The nonstoichiometry is

21

accommodated by cation vacancies (Laves 1930 ; Hagg and Sucksdorf 1933) and (2) cation occupation of the trigonal bipyramid sites (Goodenough, 1978).

2.2 NOMENCLATURE AND NOTATION CONVENTION

Some of the nomenclature used in the iron sulfide literature has come to have several meanings. In order to avoid possible misunderstanding, we will define the terms used in this study.

Pyrrhotite or pyrrhotite group : All iron sulfide compounds, $Fe_{1-x}S$, that possess the NiAs substructure.

Troilite *: Stoichiometric FeS with space group $P\overline{6}2C$ (see Section 2.4).

Monoclinic pyrrhotite : Pyrrhotite that exhibits 4C structure (see Section 2.5) by diffraction and has space group F 2/d.

Hexagonal pyrrhotite : All pyrrhotites that exhibit hexagonal symmetry by diffraction, excluding superstructure reflections. This term is equivalent to the "intermediate" pyrrhotite defined by Morimoto et al. (1975).

Commensurate structure : structure whose superstructure reflection distances are commensurate with those of the substructure reflections.

Incommensurate structure : superstructure that is not a commensurate structure.

The pyrrhotite superstructures are designated following the convention of Wuensch (1963). The dimensions of the superstructure, denoted by lower case letters, are expressed as multiples of the NiAs substructure dimensions, which are denoted by capital letters. A superstructure is usually referred to by its "c "or "a" cell dimension. For example, monoclinic pyrrhotite is designated 4C because its cell dimensions are $c = 4C$, $a = 2A$, $b = 2\sqrt{3}A$. Diagramatic sketches of the reciprocal

22

$\underline{A}^*\underline{C}^*$ planes of the most frequently reported superstructures are shown in Figures 2.3 and 2.4.

2.3 PHASE RELATIONS OF $Fe_{1-x}S$, $0<x<0.125$

Figures 2.5 and 2.6 depict the current understanding of the phase relations in the $Fe_{1-x}S$ system (Nakazawa and Morimoto 1970, Kissin and Scott 1982). The phase relations between the maximum melting temperature 1463 K and 583 K appear to be straighforward and generally well accepted (by well accepted we mean a general agreement among most workers in this field and this agreement has been quoted in books and major review papers). The entire phase field is occupied by a single solid solution, $Fe_{1-x}S$. This solid solution has a NiAs (1C) structure in which the iron atoms and vacancies are randomly distributed on the cation sites. Only one conflicting result was reported by Desborough and Carpenter (1965). They observed a hexagonal a = 2A, c = 7C structure in the temperature range from 583 K to 923 K.

Below 583 K, the phase relations are highly controversial. In the composition range from FeS (50 at % Fe) to $Fe_{0.94}S$ (48.45 at % Fe) and the temperature range from 583 K to T_α (see Figure 2.5 for definition of T_α), according to Nakazawa and Morimoto (1970), Sugaki and Shima (1977), the 1C phase extends from 583 K to a transformation temperature T_α. Below T_α the 1C phase decomposes to troilite (FeS, 2C; see Section 2.4) and an iron poor 1C phase. Kissin and Scott used the results of Sugaki and Shima in their phase diagram. Desborough and Carpenter (1965) and Yund and Hall (1968), however, reported that the stable phase above T_α is the hexagonal a = 2A, c = 5C structure (see Section 2.7). King and Prewitt (1982) and Putnis (1975a,b) in their heating studies of the stoichiometric FeS structure reported that troilite FeS did not transform to the NiAs 1C structure

above $T\alpha$. King and Prewitt (1982) reported that troilite FeS (2C) transforms to a MnP-type structure at 415 K. At 573 K the MnP-type structure transforms to the 1C structure. Putnis reported that under heating by the electron beam, troilite transforms into the NiAs structure. However, upon cooling the high temperature 1C phase continuously transforms to an a = 2A, c = 1C phase. Upon further cooling, the 2C FeS structure appears and coexists with the 2A, 1C phase. Putnis suggested that the a = 2A, c = 1C structure is a metastable phase.

Conflicting results on the decomposition products of the phase separation at temperature below T_α were also reported. At the stoichiometric end and below T_α, the stability of troilite FeS is very much disputed. In the mineralogical literature, synthetic and natural troilite FeS are reported to be both stoichiometric and stable. However, other investigations have found that FeS is unstable and decomposes into two compounds, one on each side of the stoichiometric composition. Work on synthetic crystals by Sparks et al. (1962) indicated that $Fe_{1-x}S$ is stable in the range from x = 0.004 to x = 0.006. They suggested that when cooled below 415 K FeS actually separates into two phases, one of which is magnetic. Mössbauer studies by Thiel and Van den Berg (1968, 1970) of synthetic FeS also indicated the existence of two different phases. Their attempt to detect the tetrahedrally-coordinated iron atoms in the iron rich phase was inconclusive. Putnis (1975 a, b), using electron microscopy, reported that meteoritic FeS undergoes a phase separation to both sides of the stoichiometric composition upon annealing at temperature between 363 K and 388 K. He asserted that the iron-poor phase has a modulated structure based on an a = 2A, c = 1C supercell which is formed by vacancy ordering. The iron-rich phase has the troilite superstructure with excess iron in the bipyramid interstices. At the other end, the composition of the decomposition product extends to $Fe_{0.92}S$ (47.91 at % Fe). Disagreement still exists on the stability and structure of this end product. Yund and Hall (1968)

24

maintained that the structure is an a = 2A, c = 5C superstructure. Morimoto amd Nakazawa (1970,1978) reported a 6C superstructure in a slowly-cooled experiment with the crystal's iron composition more than $Fe_{0.94}S$. They also reported that by rapid cooling of $Fe_{0.95}S$ from high temperature (above 375 K) to 367 K the structure changes from a 1C structure to a metastable nonintegral type 4.5C superstructure.

In the composition range from $Fe_{0.94}S$ to $Fe_{0.875}S$ and below 583 K, the phase relations of $Fe_{1-x}S$ are enigmatic. From x-ray sudies of natural and synthetic pyrrhotite, Nakazawa and Morimoto (1970,1978) (see Figure 2.5) reported that $Fe_{1-x}S$ is stable as the NC structure (see Section 2.7) in the composition and temperature ranges from $FeO_{.94}S$ to $Fe_{0.91}S$ and from T_{NC} (see Figure 2.5 for definition of T_{NC} and T_{NA}) to 373 K. The value of "N" varies as a function of composition and temperature. N increases as the vacancy content decreases. As temperature increases, however, N was reported to decrease. Upon cooling, N remains invariant (Figure 2.7). From $Fe_{0.91}S$ to $Fe_{0.9}S$, the high temperature 1C structure transforms to a NA phase at temperature T_{NA} . This NA phase subsequently was reported to tranform to the NC structure at about 483 K. Below 373 K, Morimoto and Nakazawa indicated that the NC phase transforms to a homologous compositional series: $Fe_{11}S_{12}$ (6C), $Fe_{10}S_{11}$ (11C) and Fe_9S_{10} (5C). The nature of the transformation remains unclear. In the composition range from $Fe_{0.9}S$ to $Fe_{0.875}S$, there is a miscibility gap between the NC or NA phase and the 4C phase for temperature below 563 K. Nakazawa and Morimoto also maintained that the composition of the 4C phase is Fe_7S_8. From 563 K to 578 K, $Fe_{1-x}S$ is stable as a mixture of the 1C and MC phases (see Figure 2.5). This two phase mixture transforms to a mixture of 1C and pyrite phases before transforming to the 1C phase.

The phase relations of $Fe_{1-x}S$ in the composition range from $Fe_{0.92}S$ to FeS_2 were also investigated by Kissin and Scott (1982) using a hydrothermal

25

recrystallization technique (Figure 2.6). At temperatures below 483 K, there are three two-phase field regions separating the 1C and NC phases, NC and 4C phases. and 4C and pyrite phases. In the temperature range from 483 K to 539 K, three other two-phase field regions separate the 1C, NA, 4C and pyrite phases. There are two two-phase field regions at temperature from 539 K to about 583 K. These miscibility gaps separate the MC phase from 1C and pyrite phases. Kissin and Scott reported that monoclinic pyrrhotite (4C phase) exists over a range of compositions. Kissin and Scott did not investigate the phase relations at temperature below 373 K.

In addition to reports by Kissin and Scott and Nakazawa and Morimoto, numerous other studies have also been carried out to investigate the structures and stabilities of $Fe_{1-x}S$ in the composition range from $Fe_{0.92}S$ to $Fe_{0.875}S$. Sugaki and Shima (1977) and Sugaki and coworkers (1977) in their hydrothermal synthesis studies reported a phase diagram that was almost identical to that of Nakazawa and Morimoto. In the temperature range from 483 K to 623 K, different structures of $Fe_{1-x}S$ at composition "Fe_7S_8" were reported by many workers. Liliental et al. (1981), Nakano et al. (1979), Keller-Besrest et al. (1983) and Fleet (1968, 1971) observed a 3C superstructure from quenched samples of composition exactly or close to Fe_7S_8 (Figure 2.12). Corlett (1968), in an *in situ* high temperature X-ray experiment, concluded that the 4C structure transforms into the 1C structure at a temperature somewhere between 488 K and 513 K. This phase transition was reversible upon slow cooling. If the cooling rate was more rapid, a "3C" superstructure was produced. Corlett subsequently noted that the spacing of the super-structure is not exactly 3C. Keller-Besrest et al. (1983), using x-ray diffraction, reported a mixture of 4C and 3C superstructures in synthetic pyrrhotite (grown by the chemical vapor transport method at 973 K and quenched). Their "single" crystal X-ray diffraction pattern also revealed strong diffuse streaks

26

in the C^* direction along the substructure reflections as well as along the superstructure reflections. They attributed this diffuse scattering to stacking faults in the sulfur sublattice. Francis and Craig (1976) using electron diffraction reported a 3C, NA structure where N may or may not be commensurate with the basic NiAs structure. (Morimoto and Nakazawa (1978) reported that the 4C structure is stable up to 573 K where it transforms to an "MC" phase. They asserted that the 3C structure is a special case of the NA structure which is only stable in the composition range from Fe_9S_{10} to $Fe_{11}S_{12}$). Using high resolution transmission electron microscopy Pierce and Buseck (1974, 1976) studied pyrrhotite with an average composition of $Fe_{0.91}S$, in which they observed a mixture of 4C, 5C and NC structures.

Intergrowths of the 4C phase with other pyrrhotite phases as well as with the 2C phase were observed by Putnis (1975) using electron diffraction and conventional electron microscopic imaging techniques. Based on the fact that the 4C phase coexists with the 2C phase, Putnis then questioned the thermodynamic stability of the intermediate compounds.

Finally, the decomposition mechanisms of the miscibility gaps have not been established clearly either. Based on the optical observation of the microstructures of annealed $Fe_{1-x}S$ (0<x<0.07) Yund and Hall (1968) suggested nucleation and growth as the phase separation mechanism of FeS and the intermediate compounds. Putnis (1975), using transmission electron microscopy to study annealed "FeS", reported a two phase microstructure that was consistent with spinodal decomposition mechanism (a microstructure similar to that observed by Putnis is shown in Figure 4.4a). He concluded that the resulting phases differ slightly in their iron content and that their compositions lie on either side of the stoichiometric composition. We note that Putnis prepared his electron transparent

27

TEM samples by ion thinning at room temperature. The decomposition mechanism that separates monoclinic pyrrhotite and the intermediate compounds is not known.

2.4 TROILITE STRUCTURE

Troilite*, FeS, is commonly found in meteorites, terrestrial deposits and is ubiquitous to all lunar samples from the Apollo 11 and 12 missions (all of these in the mineralogical jargon means that this is a stable phase because it exists for a long time). The crystal structure of troilite has been studied using X-ray diffraction by Bertaut (1956), Evans (1970) (lunar troilite) and King and Prewitt (1982) (synthetic crystals). Troilite has been found to have an $a = \sqrt{A}$, $c = 2C$ superstructure (Figure 2.8) where A and C are the dimensions of the NiAs unit cell. The space group of troilite has been determined to be P62C. The troilite unit cell contains 12 FeS formula units and has the lattice parameters of $a=b=5.963 \pm 0.0003$ Å, $c = 11.754 \pm 0.001$ Å, $\alpha = \beta = 90.00 \pm 0.01^{o}$; $\gamma = 120.01 \pm 0.01^{o}$ (King and Prewitt 1982).

The troilite structure is related to the parent NiAs structure through small displacements of iron and sulfur atoms. The Fe atoms in an NiAs-type structure are six-coordinated by S atoms with each octahedron sharing edges with six octahedra in the plane normal to $\underline{c}$ and sharing faces with two others along $\underline{c}$ (Figure 2.2). In troilite, the Fe atoms are displaced in such a way that two of the six Fe-Fe distances across those shared edges are shortened. These Fe-atom displacements link the Fe atoms into triangular groups whose normal points along the c-axis (Figure 2.9). Across the shared face, these groups are paired into six-atom prisms. Across the intra-prism shared face, the metal-metal distance along the prism is longer than that between prisms suggesting repulsive interaction between Fe-Fe. The iron displacement is 0.305 Å.

28

The distortion of the hexagonal close-packed sulfur framework is very small. Of the three symmetrically distinct S atoms, S(2) and S(3) are displaced from their ideal position (see Table 2.1). S(3) is displaced normal to c by a very small distance of 0.021Å . The S(2) atoms are displaced along the c by 0.244Å and therefore lie above and below the plane passing through the S(1) and S(3) atoms. This distortion is closely related to the formation of the Fe prism.

The displacement that draws the iron atoms into the triangular groups also moves them away from the center of the surrounding octahedron. The FeS_6 octahedron is therefore severely distorted. The fact that the bond lengths to the six nearest neighbors of the Fe atom vary as much as 0.36 Å makes its coordination nearly five fold.

The positional parameters for FeS in the troilite structure are given in Table 2.1.

2.5 MONOCLINIC PYRRHOTITE

Monoclinic pyrrhotite, the end member of $Fe_{1-x}S$ on the iron deficient side, is the most extensively studied iron sulfide compound. The iron deficiency in this compound is accommodated by iron vacancies which order at low temperature. Despite disagreements over the composition range, the mode of vacancy ordering has been worked out and generally accepted. Single crystal X-ray studies of this pyrrhotite were carried out by Bertaut (1952, 1953 ; twinned, natural sample of unknown composition), Buerger (1947) and Wuensch (1963; twinned, natural Fe_8S_9), Corlett (1964, 1968; natural Fe_7S_8) and Tokonami et al. (1972; natural sample). Results from these studies indicated that the crystal is monoclinic with vacancies ordered in alternate iron layers normal to the c-axis (Figures 2.10, 2.11). The space group is F2/d , and the unit cell contains eight Fe_7S_8 formula units. The

cell dimensions are approximately a = 2A, b = $2\sqrt{3}$A and c = 4C. Pyrrhotite with cell dimension c = 4C is usually referred to as "monoclinic" pyrrhotite. The atomic positions for the monoclinic pyrrhotite structure are listed in Table 2.2.

Studies using high-resolution transmission electron microscopy by Nakazawa and Morimoto (1974-1976) confirmed the stacking sequence of the 4C-structure. They showed that Fe_7S_8 is extensively twinned along the c-axis. Microscopic twins which contain from two to ten stacked layers are deemed responsible for the streaking observed in the diffraction patterns. White streaks in the high-resolution micrographs were attributed to out of step boundaries of orientation [102] and [114]. Other defects such as anti-phase boundaries, twins and stacking faults were predicted and observed by Van Landuyt and Amelinckx (1972).

2.6 3C STRUCTURE

The crystal structure of the 3C phase was determined by Fleet (1968) and later refined by Nakano et al. (1979). The iron vacancies have also been found to order in alternate iron layers normal to the c-axis (Figure2.12). The space group of this structure is $P3_121$ with a = 6.8652±0.0006 Å ,   c = 17.047±0.002 Å . The position parameters for this structure are listed in Table 2.3.

2.7 INTERMEDIATE PYRRHOTITE

Intermediate or hexagonal pyrrhotites are iron sulfide "compounds" with composition ranging nominally from $Fe_{0.9}S$ to $Fe_{0.92}S$.

Despite numerous reports on the occurrence of the 5C and 6C superstructures, only Morimoto, Koto and Gyobu (1975,1981) attempted to study the detailed crystal structures of these two superstructures. The space groups of the 5C and 6C

30

structures are tentatively given as C.ca and $F\frac{\overline{1}}{d}$ respectively. Koto and coworkers (1975) modeled the 5C and 6C superstructures with a filled layer of iron atoms alternating with two consecutive defective layers along the C-axis (Figure 2.13). The defective layers are assumed to be statistically filled with iron vacancies.

High-resolution transmission electron microscopic studies of the intermediate pyrrhotite have also been carried out by Nakazawa, Morimoto and Watanabe (1976) and Pierce and Buseck (1974, 1976, 1979). In their study, Nakazawa et al. interpreted their high resolution images to be the 5C structure. From their images, they also concluded that the 5C structure is an average structure consisting of a statistical distribution of iron vacancies along the c-axis. The iron vacancies are distributed in two or more successive iron layers. During their TEM observation, the electron beam increased the specimen temperature sufficiently so that a phase transformation between the nC and nA phases was observed. This transition, however, was not observed dynamically.

Using both x-ray diffraction pattern and high resolution images, Nakazawa and coworkers proposed a model for the NA structure. This structure consists of three domains related by 1/3 C glide along the a-axis (see figure 2.14).

Pierce and Buseck studied pyrrhotite with average composition of $Fe_{0.91}S$, in which they observed a mixture of 5C, 4C and NC structures. Their lattice images of the 5C structure indicated the presence of antiphase domains of ordered iron vacancies with an apparent out of step vector eqal to 1/2 $\underline{a}$. High resolution "dark field" images of incommensurate 5.1C structure showed that this structure contains a mixture of very small domains separated by antiphase boundaries. The dimension of the domain is typically five or six times the length of the C dimension of the NiAs basic structure. The 5C structure proposed by Nakazawa et al. was not observed by them.

31

Pierce and Buseck also used the Minagawa equation (Minagawa 1972) to predict the non-integral superstructure spacing when the domain sizes are not the same. Subsequently, Pierce, in his thesis, concluded that all incommensurate structures can be explained by a structural model consisting of stacking along the c-axis of plate-like antiphase domains. He also suggested that the change in vacancy concentration is accommodated by change in antiphase domain size.

Recently, Yamamoto and Nakazawa (1982) used the four-dimensional space group W_{99} to analyse the diffraction pattern of the NC-type pyrrhotite. They concluded that the Fe vacancies are distributed spirally along the c-axis.

2.8 MAGNETIC PROPERTIES OF $Fe_{1-x}S$

The magnetic phase diagram of $Fe_{1-x}S$ ($0<x<0.125$), like the compositional phase diagram, is controversial. In this section we will not review the magnetic phase relations but will describe some general magnetic properties that are relevant to this thesis. We will particularly concentrate our discussion on the magnetic properties of $Fe_{0.9}S$.

It is generally accepted that the 1C phase is paramagnetic above 600 K and antiferromagnetic below 600 K, the 2C and NC phases are antiferromagnetic, and the 4C and NA phases are ferrimagnetic. The antiferromagnetism of the 2C phase and ferrimagnetism of the 4C phase have been known to arise from the mutually antiparallel orientation of the electron spins in alternating iron layers parallel to the basal plane. In the 2C structure , every iron layer is filled and hence leads to exact cancellation of the magnetic moment. In the 4C structure, the iron vacancies order in alternate iron planes. Exact moment cancellation does not occur and therefore gives rise to ferrimagnetism.

The magnetism of $Fe_{0.9}S$ is particularly interesting and has been extensively studied (Marusak and Mulay 1979, 1980; Ovanesyan et al. 1971; Bennett and Graham 1981; Schwarz and Vaughan 1972) . $Fe_{0.9}S$ has been found to be antiferromagnetic below 460 K and above 550 K and ferrimagnetic in between these two temperatures. Evidence of the antiferromagnetic to ferrimagnetic phase transformation (known as the λ transition) can be found in the measurement of magnetization as a function of temperature (Figure 2.15). It is particularly interesting to note the slow rise and fall of the magnetization. Explanation of this event will be given in Section 7.4.

Several theories have been proposed to explained the λ transition. Lotgering (1956) explains the λ transition as follows. Above the β or antiferromagnetic-to-paramagnetic transformation (600 K) both spins and vacancies are disordered. On reducing the temperature, magnetic order sets in at 600 K but because of the vacancy disorder, exact cancellation of the two sublattice occurs, resulting in antiferromagnetism. At 550 K, the iron vacancies order and lead to imperfect magnetic sublattice cancellation and therefore ferrimagnetism. Below 460 K, the vacancies disorder and ferrimagnetism reverts back to antiferromagnetism.

Marusak and Mulay (1979,1980) agreed with Lotgering's explanation for the higher temperature part. They, however, suggested that the antiferromagnetisms is due to the 5C superstructure (see Section 2.6) and not a vacancy disordered structure. They also proposed that the ferrimagnetic phase has a 4C superstructure.

Finally, it is of interest to note that in the crystal synthesis process, Marusak found that $Fe_{0.9}S$ crystal is ferrimagnetic if it is fast-cooled to room temperature. In order to produce the antiferromagnetic phase, Marusak had to anneal the sample at 388 K for four months and then for six months at room temperature.

33

2.9 DIFFUSION IN $Fe_{1-x}S$

To date no study on diffusion in $Fe_{1-x}S$ has been carried out for temperatures below 620 K. Only one study was carried out to determine the iron self-diffusion in $Fe_{1-x}S$ at high temperature (>620 K). This study by Condit and coworkers (1974) used the radiotracer technique. They found the iron self-diffusion coefficient in $Fe_{1-x}S$ above 620K to be

$$D = D_0\delta \exp(-((81\pm4) + (84\pm20)\delta)/RT)$$

where the exponential units are kJ/mole, D_0 is $(1.7\pm0.1)\times10^{-6}$ and $(3.0 \pm 0.2)\times10^{-6}$ m^2/sec for diffusion in the a- and c-dirctions, respectively. δ is the deviation from stoichiometry as given in the formula $Fe_{1-\delta}S$ and ranges from 0.003 to 0.153.

Condit and coworkers found that iron atoms diffuse by a vacancy mechanism and the diffusion of sulfur atoms is many order of magnitude smaller than for iron.

Since there are no diffusion data available at low temperature, we will extrapolate Condit and coworkers' results to lower temperature and use them to estimate the annealing time in the study of phase relations. We will show in Section 6.4 that this undertaking is quite reasonable.

2.10 DISCUSSION

Despite contradictory reports on the structures of the $Fe_{1-x}S$ phase above T_{α}, the literature appears to accept the results reported by Nakazawa and Morimoto. No acceptable reason has been given to explain Carpenter and Desborough (1964) and Yund and Hall (1968) results. The phase transformation mechanisms also remain unresolved. Conflicting results on the phase transformation can be attributed to

the method of investigation. The study of phase transformation cannot just be based on the observation of microstructural features.

A major problem that has plagued almost all studies to date is the inability to perform *in situ* heating experiments . Studies of high temperature phase relations from quenched samples are meaningful only if the diffusion kinetics are sufficiently slow on the experiment time scale. There is little evidence that this is the case in the $Fe_{1-x}S$ system. Because of the long exposure requirement and limitation of time, the *in situ* heating x-ray diffraction studies carried out by Corlett and Nakazawa and Morimoto lacked the necessary temperature resolution required to follow a phase transformation closely. This problem, coupled with the microscopic compositional inhomogeneities, naturally causes chaos in the literature.

It is clear from previous sections that major disagreements still exist in the entire $Fe_{1-x}S$ (0<x<0.125) phase diagram and that studies of phase transformation mechanisms to date are inconclusive.

Temperature: 294 K

Pressure: 0.0001 Pa

$a = b = 5.963(1)\text{Å} \; ; \; c = 11.754(1)\text{Å}$

$\alpha = 90.00(1)^0 \; ; \; \beta = 90.00(1)^0 \; ; \; \gamma = 120.01(1)^0$

$V = 361.88(9)\text{Å}^3$

$c/A^* = 1.707$

space group $p\bar{6}2c$

Fe[12(i)], x: 0.3787(2)
y: 0.0553(2)
z: 0.12300(9)

S(1)[2(a)], x: 0
y: 0
z 0

S(2)[4(f)] x: 1/3
y: 2/3
z: 0.0208(2)

S(3)[6(h)] x: 0.6648(6)
y: -0.0041(4)
z: 1/4

Table 2.1. Unit-cell and posititional parameters for FeS in the troilite structure. (King and Prewitt 1982).

Temperature: 294K

Pressure: 0.0001Pa

a =   11.902(8) $\overset{o}{A}$; b = 6.859(5) $\overset{o}{A}$; c =   22.787(10) $\overset{o}{A}$

β =   90.26(3)°

Space group F 2/d

coordinate of equivalent positions:

(0, 0, 0; 1/2, 1/2, 0; 1/2, 0, 1/2; 0, 1/2, 1/2) +

x, y, z; 1/4 - x, y, 1/4 - z; x, y, z, 1/4 + x, y, 1/4 + z

	x	y	z
Fe1	0.3809(3)	0.3500(9)	-0.0063(2)
Fe2	0.3816(4)	0.3660(11)	0.1234(2)
Fe3	0.3587(3)	0.3975(9)	0.2501(2)
Fe4	0.3750	0.3528(12)	0.3750
S1	0.2061(5)	0.3660(16)	-0.0618(3)
S2	0.5418(6)	0.3833(15)	0.0598(3)
S3	0.2096(5)	0.3858(15)	0.1805(3)
S4	0.5425(5)	0.3645(15)	0.3087(3)

Table 2.2. Unit-cell and positional parameters for Fe_7S_8 in the 4C structure. (Tokonami et al. 1972).

Temperature: 294 K

Pressure: 0.0001Pa

a = b = 6.8652(6) Å ; c = 17.046 (2) Å

space group $P3_1 21$

	x	y	z
Fe(1)	0.0234(4)	0	1/3
Fe(2)	0.0283(4)	0	5/6
Fe(3)	0.4641(3)	0	5/6
Fe(4)	0.0085(5)	0.5268(3)	0.82504(5)
Fe(5)	0.0079(5)	0.5125(4)	0.33564(4)
S(1)	0.1641(4)	0.3380(6)	0.75301(7)
S(2)	0.1671(4)	0.8419(4)	0.74183(7)
S(3)	0.6608(6)	0.3321(6)	0.75129(12)
S(4)	0.6624(6)	0.8352(4)	0.75642(7)

Table 2.3. Unit-cell and positional parameters for Fe_7S_8 in the 3C structure (Nakano et al. 1979).
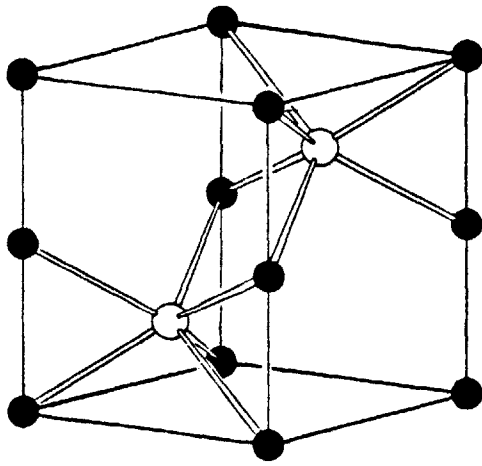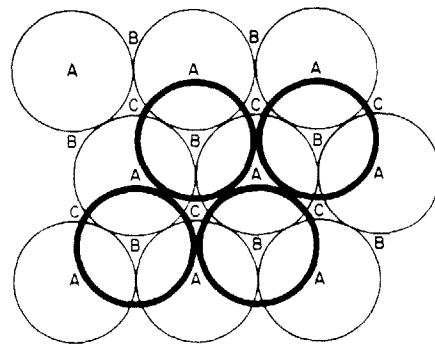
(a)   (b)

Figure 2.1. (a) The NiAs 1C structure showing linkage of ions in the unit cell.
(b) the electro-negative atoms stack in a ABAB sequence forming
a hexagonal close-packed sublattice. The electro-positive atoms
occupy the octahedral interstices (c).
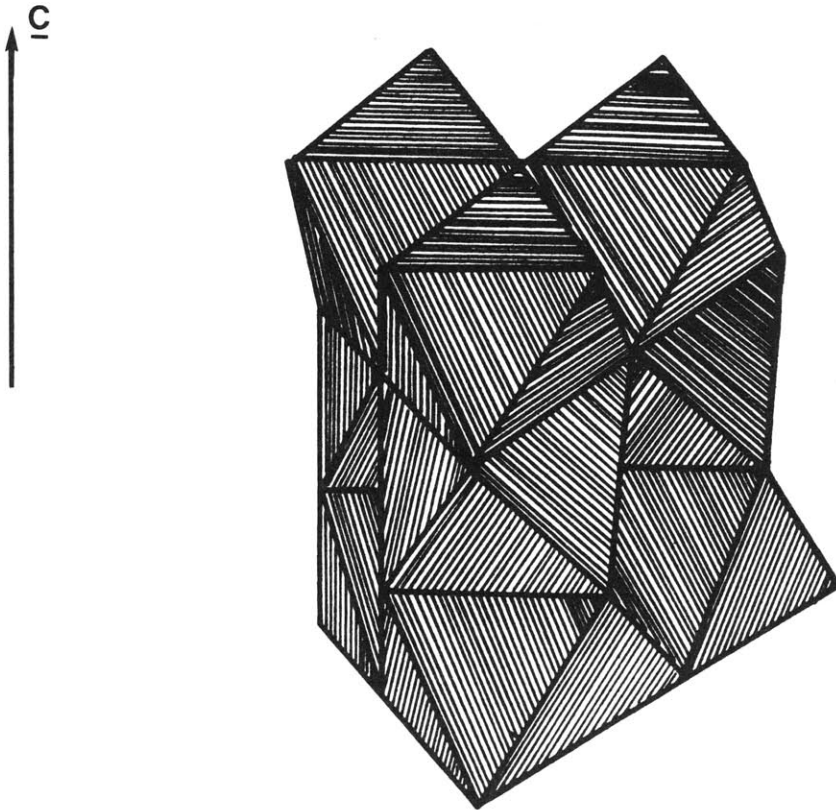
Figure 2.2. The electro-negative atoms form octahedra which share faces
along the c-axis and share edges normal to the c-axis. The
tetrahedra also share faces forming trigonal bipyramids.
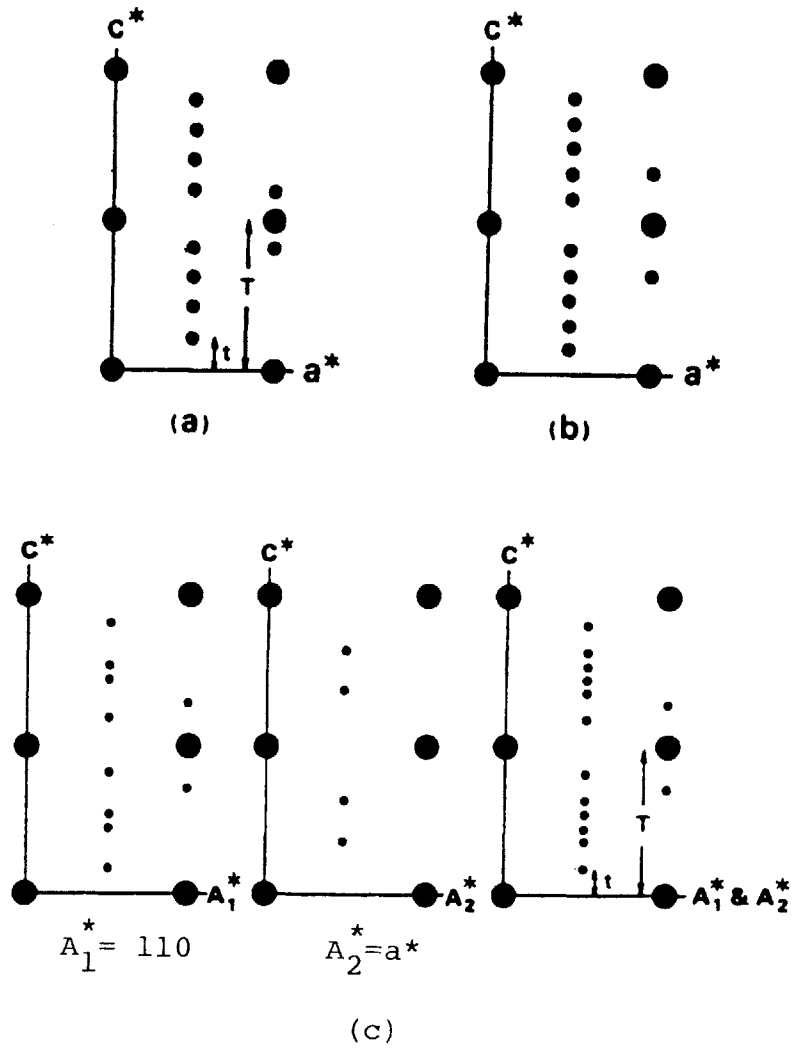
Figure 2.3. Reciprocal planes of (a) 5C, (b) 6C and (c) 11C types. Large circles represent main reflections and small circles correspond to superstructure reflections. The interval "t" is irrationally related the repeat of the main reflections "T" along the C* axis (after Nakazawa and Morimoto, 1970-1971).

41
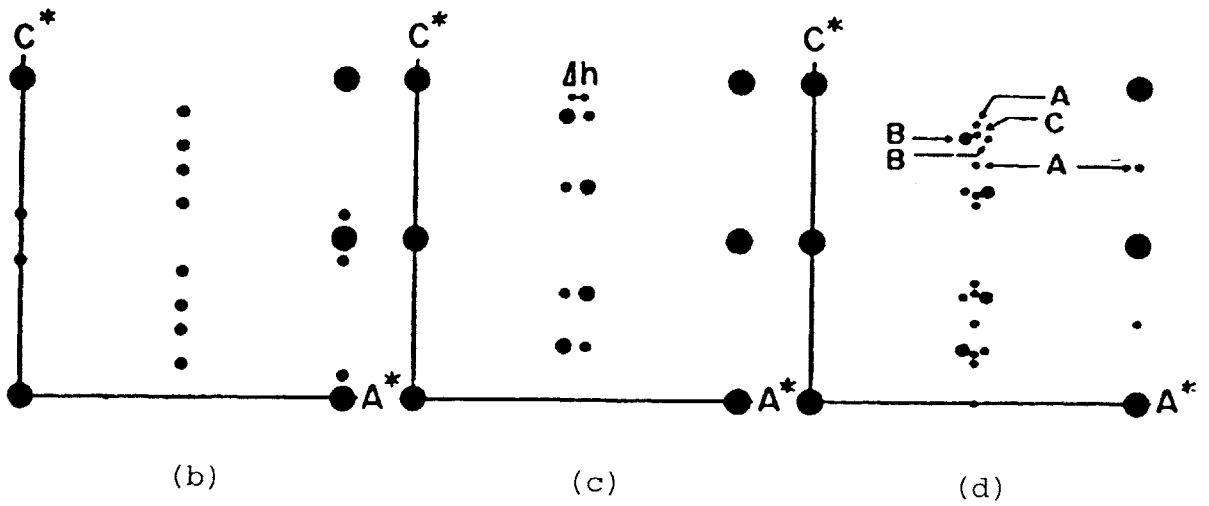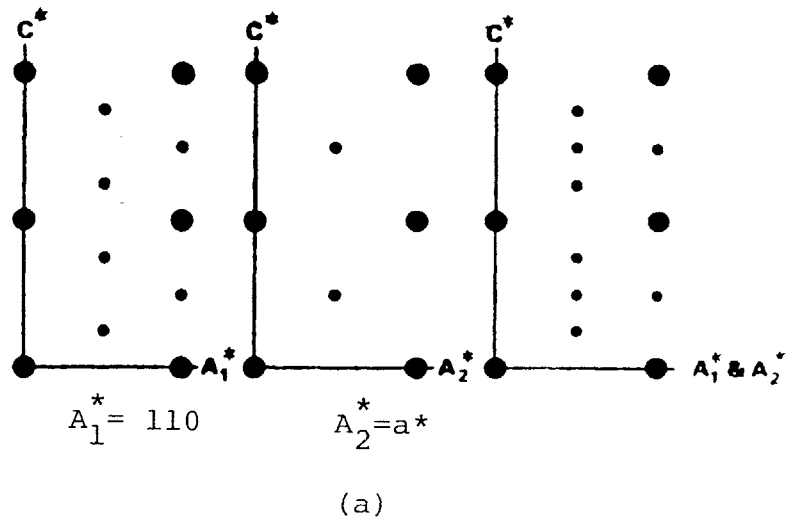
Figure 2.4. Reciprocal planes of (a) 4C, (b) NC, (c) NA and (d) 4C (A), NA (B) and MC (C) types. Large circles represent main reflections and small circles correspond to superstructure reflections (after Nakazawa and Morimoto, 1970-1971).
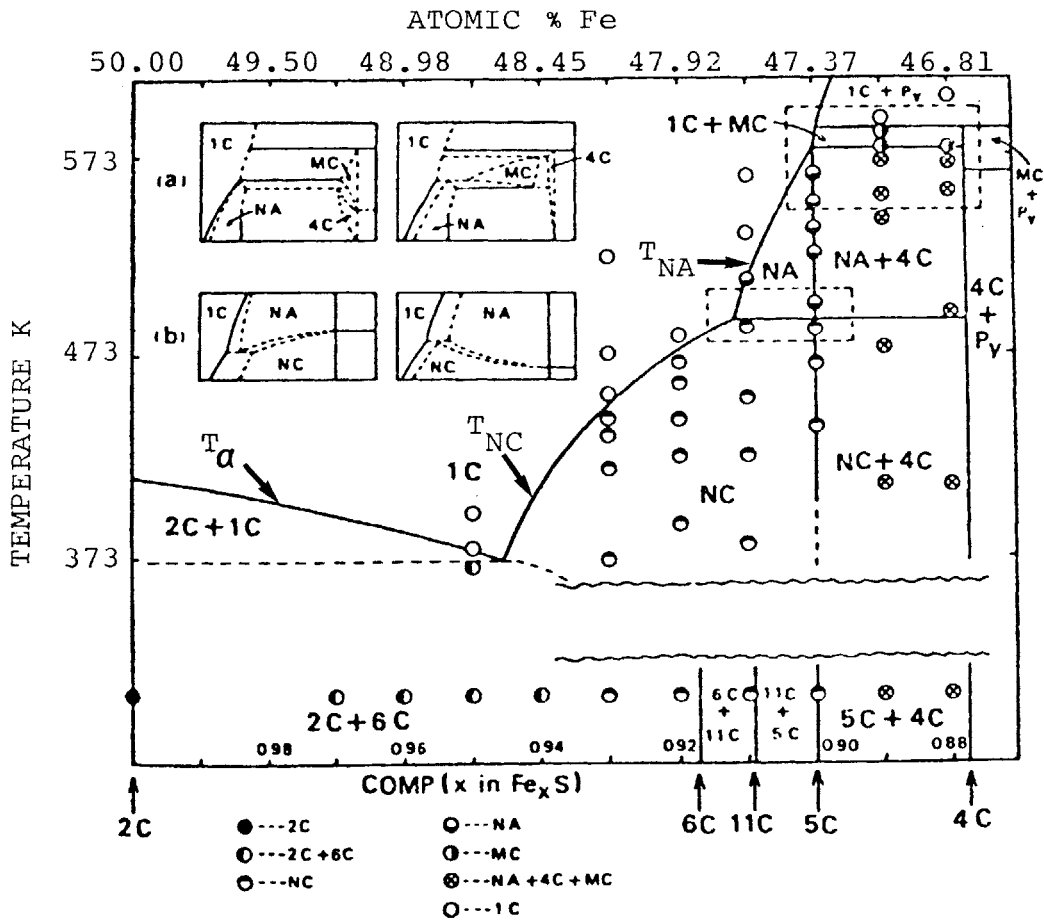
Figure 2.5. Phase diagram of the FeS-Fe$_7$S$_8$ system (after Nakazawa and Morimoto, 1971).
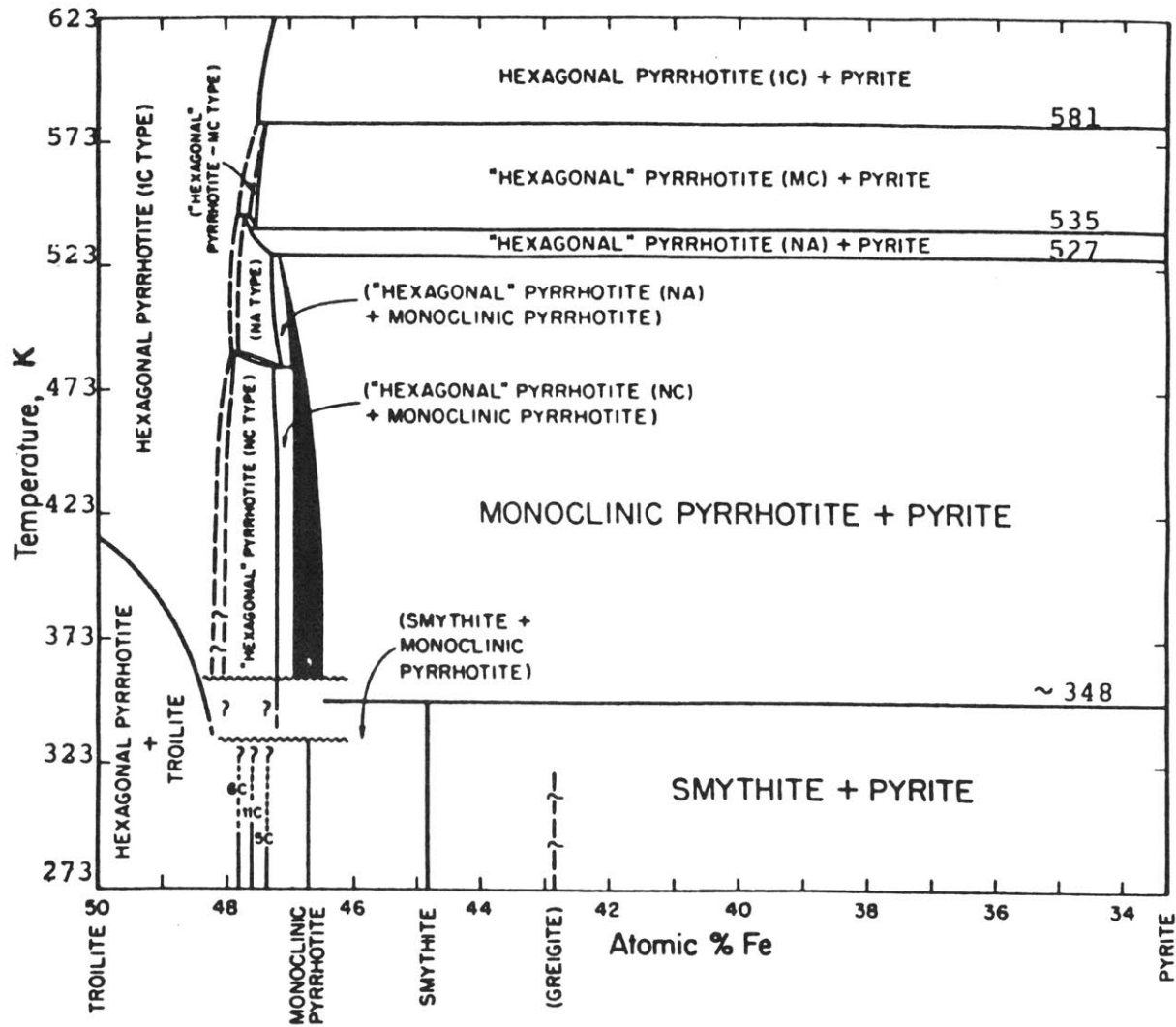
Figure 2.6. Phase diagram for the FeS-FeS$_2$ segment of the Fe-S system below 623 K (after Kissin and Scott, 1982).

44
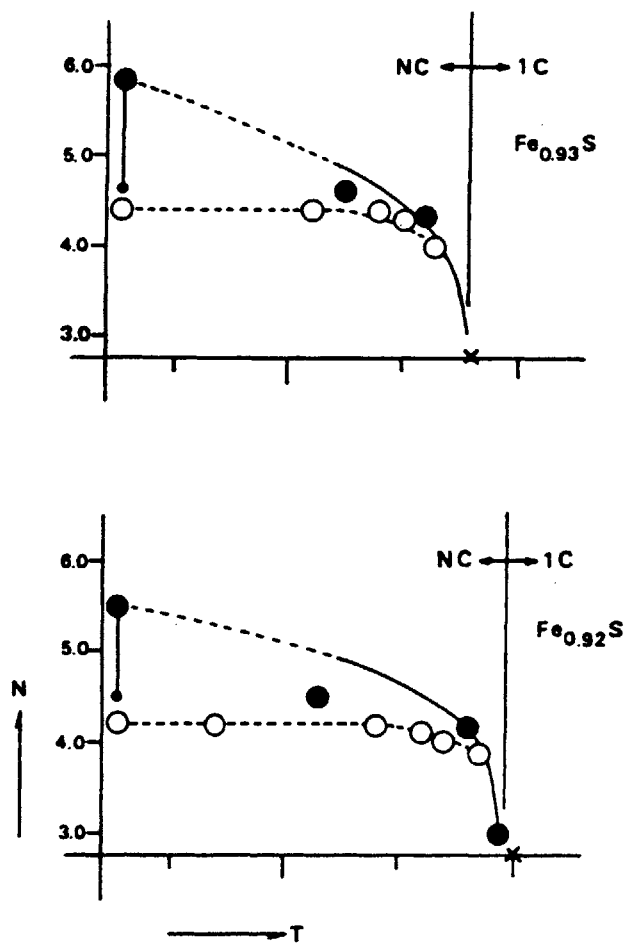
Figure 2.7. Changes of the N value by temperature for the crystals of fixed $Fe_{0.92}S$ and $Fe_{0.93}S$ compositions. The black and open circles represent the N-values obtained in heating and cooling experiments, respectively. The intensity maxima of the diffuse streaks observed at room temperature are shown by small black circles (after Nakazawa and Morimoto, 1970).
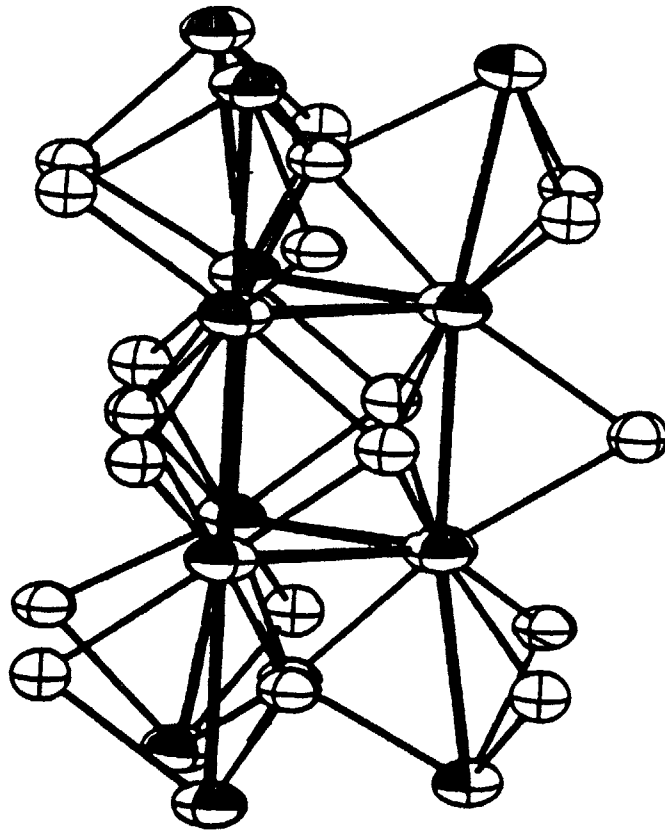
Figure 2.8. The troilite structure. The c axis of a NiAs-type unit cell points up and slightly rotated out of the plane of the drawing. The metal atoms have sectioned ellipsoids (after King and Prewitt, 1982).
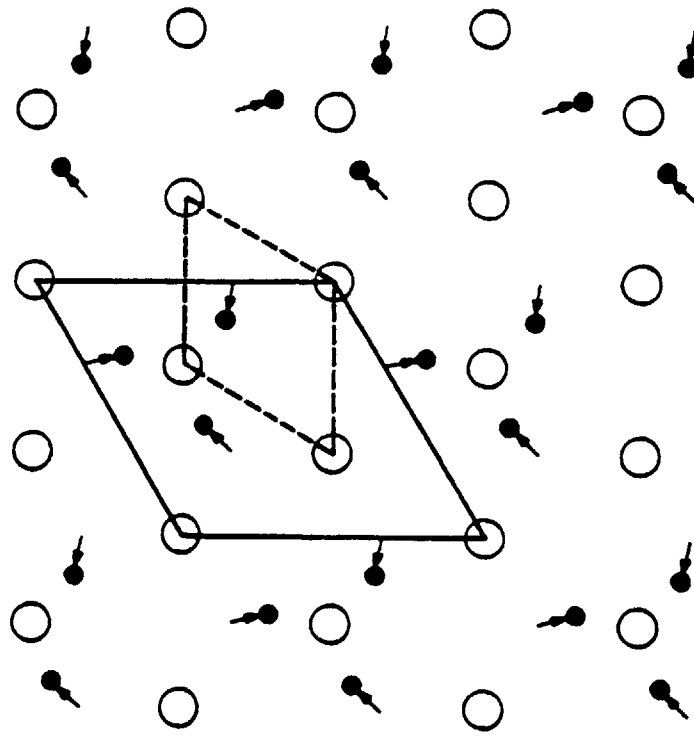
Figure 2.9. The metal atom displacements shown with exaggerated magnitudes in the troilite structure as viewed down $\underline{c}$ for an NiAs-type unit cell. The atom positions in an NiAs-type structure are indicated by the bases of the arrows (after King and Prewitt, 1982).
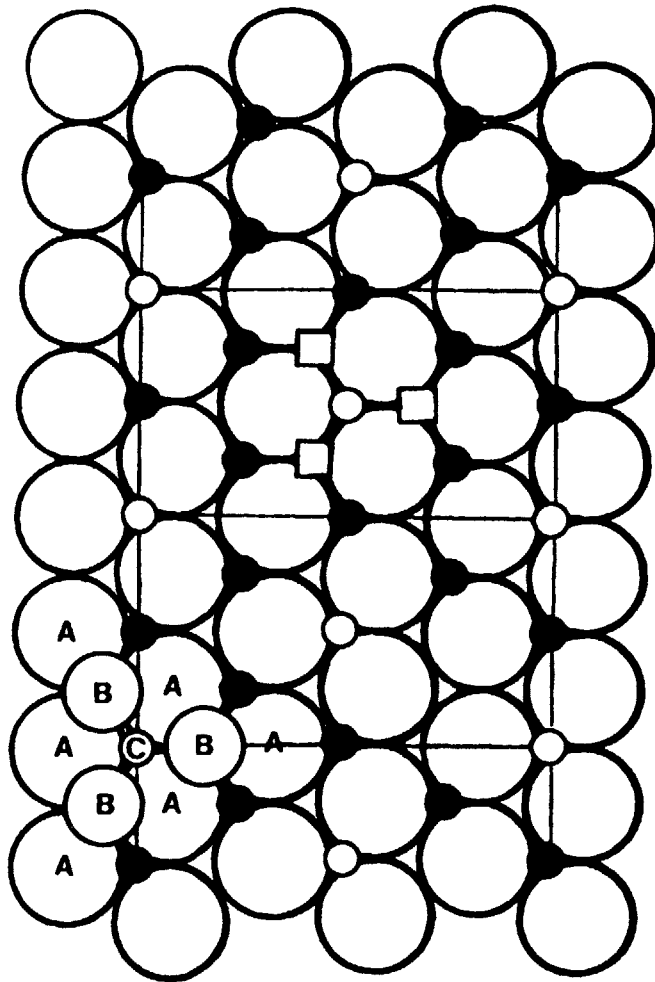
Figure 2.10. Iron vacancies order in layers normal to the c-axis. The vacancies stay in a configuration that maximizes their separations. Open circles are iron vacancies.
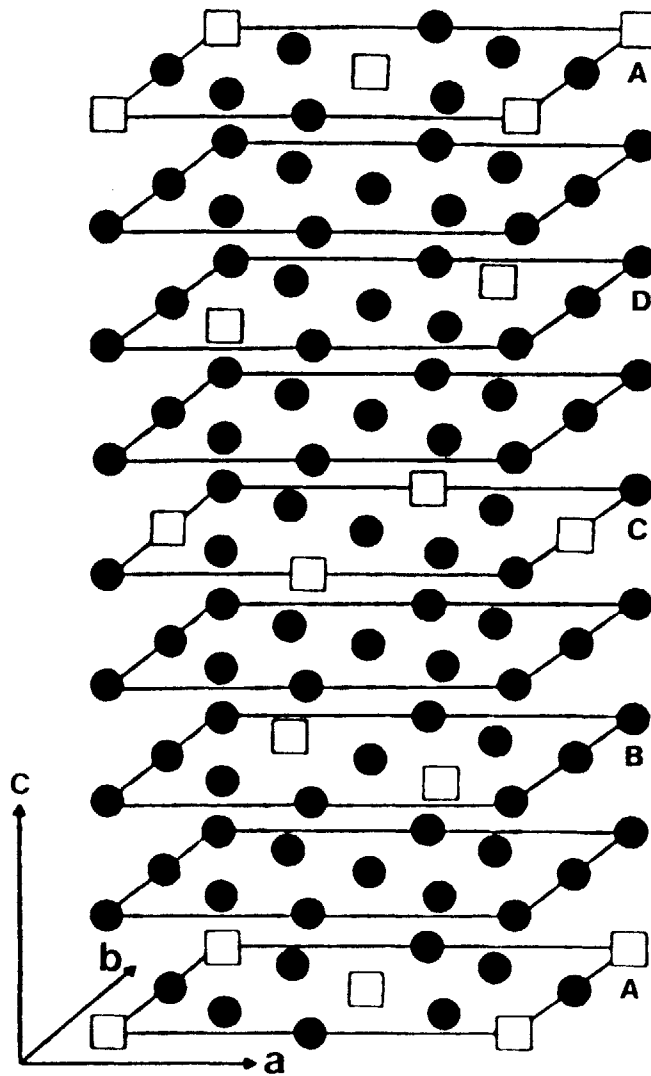
Figure 2.11. The iron vacancies in 4C-type superstructure. Only iron atoms are shown here. Squares are the vacant iron sites.
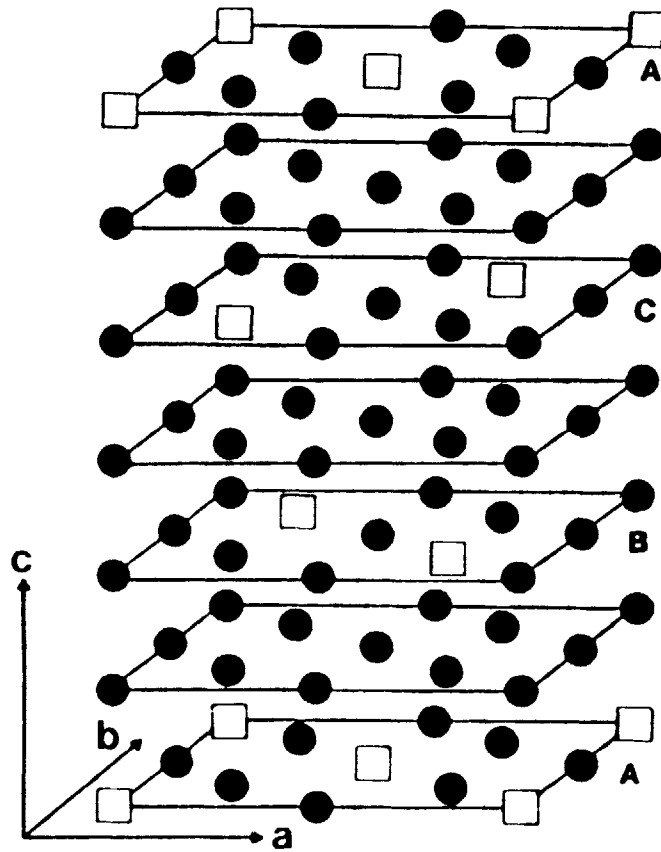
Figure 2.12. The iron vacancies in 3C-type superstructure. Only iron atoms are shown here. Squares are the vacant iron sites.
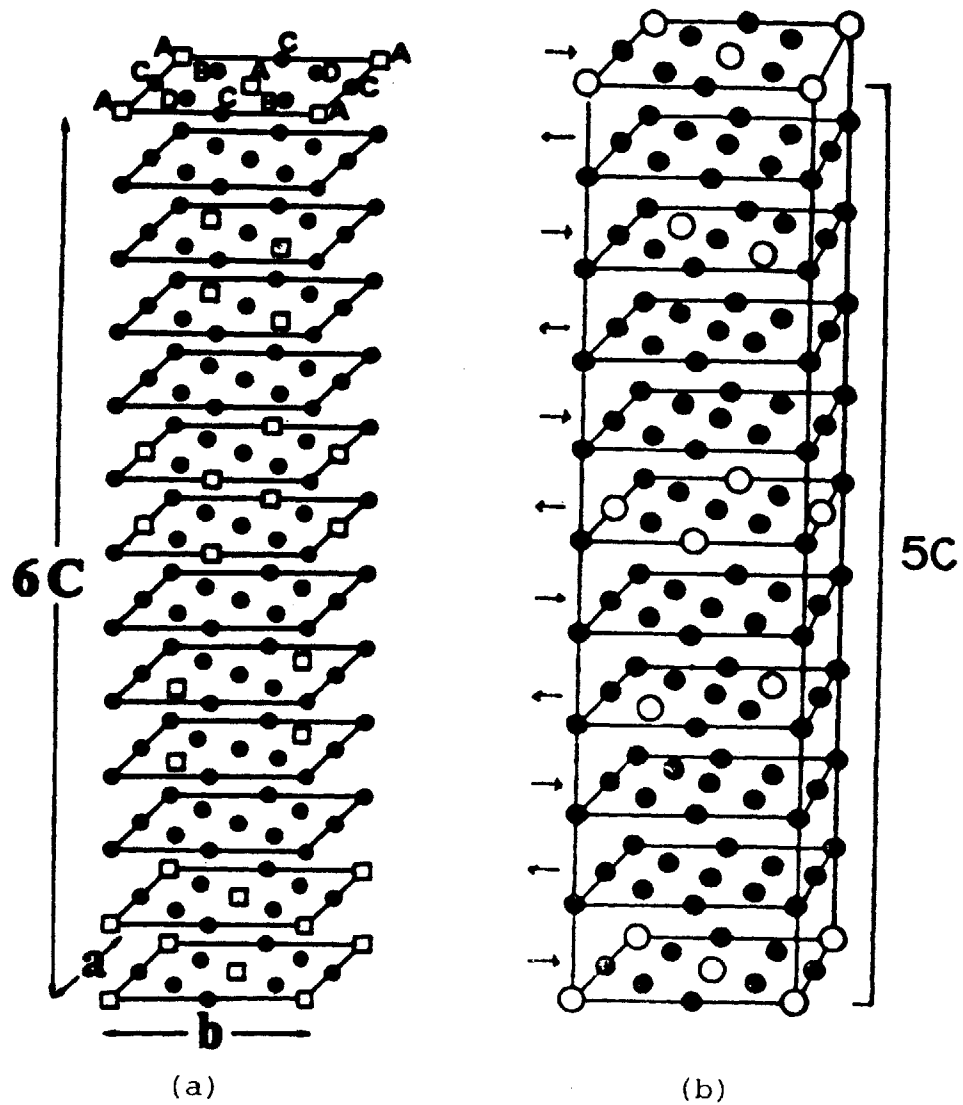
Figure 2.13. The iron vacancies in (a) 6C-type superstructure and (b) 5C-type superstructure. Only iron atoms are shown here. Squares in (a) and open circles in (b) are the vacant iron sites (after Koto et al., 1975).
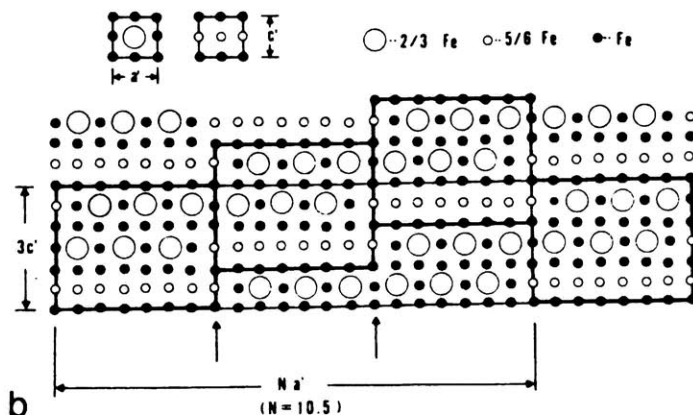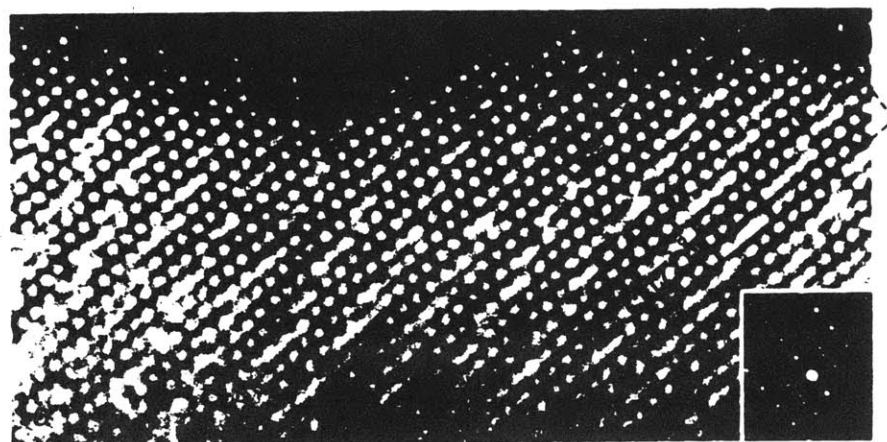
Fig. 4. (a) High magnification lattice image of the *NA* type. A unit with dimensions of a (82.6 Å) and c (17.1 Å) is indicated. An electron diffraction pattern is shown. (b) A structure model of the *NA* type. Filled circles indicate Fe sites that are completely filled. Large and small open circles are the Fe sites of 1/3 and 1/6 vacancies. respectively. Sulfur atoms are omitted for simplicity

Figure 2.14. (after Nakazawa and Morimoto, 1976).
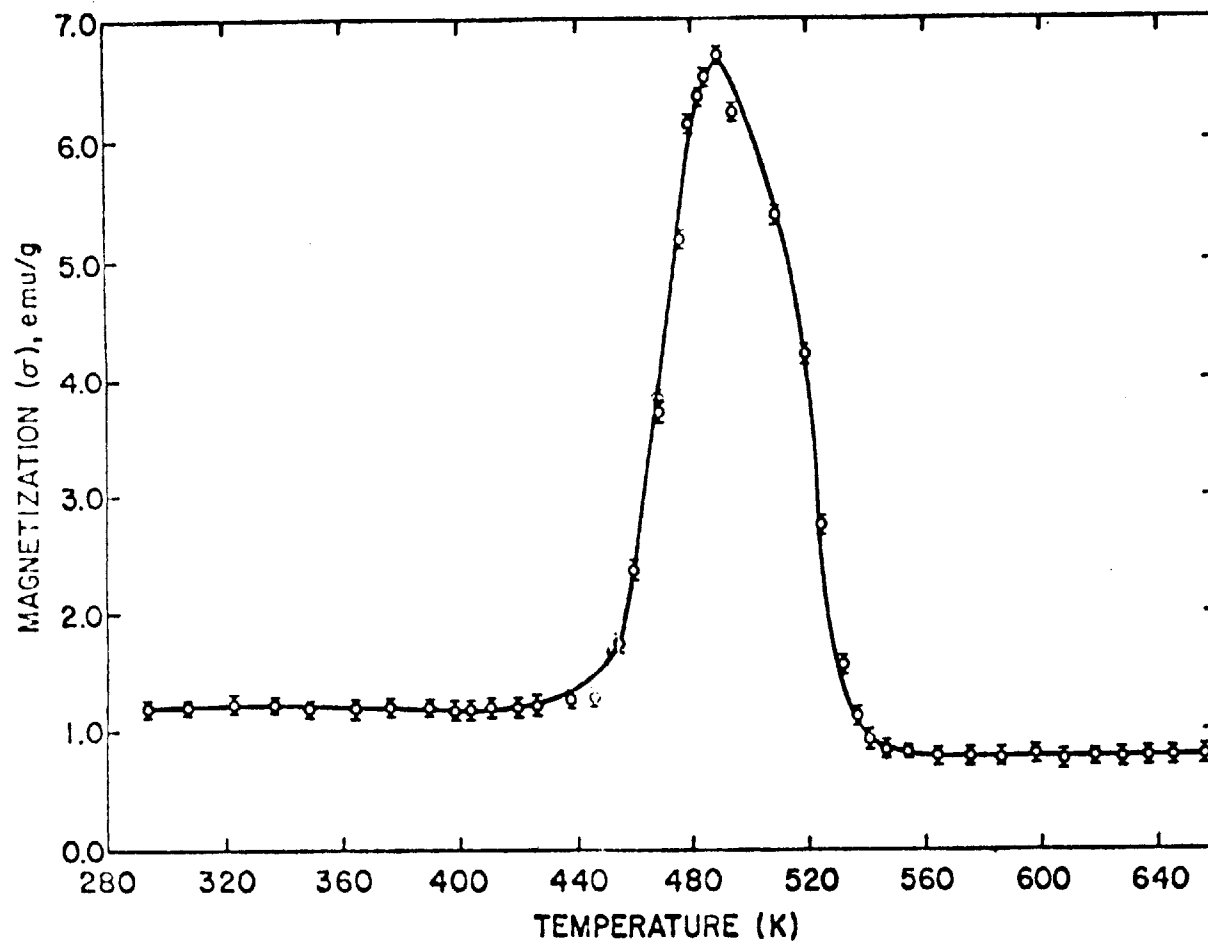
Figure 2.15. Magnetization per gram in units of emu/g in a field of 10,000Oe showing the λ transition for $Fe_{0.9}S$ (after Marusak, 1979).
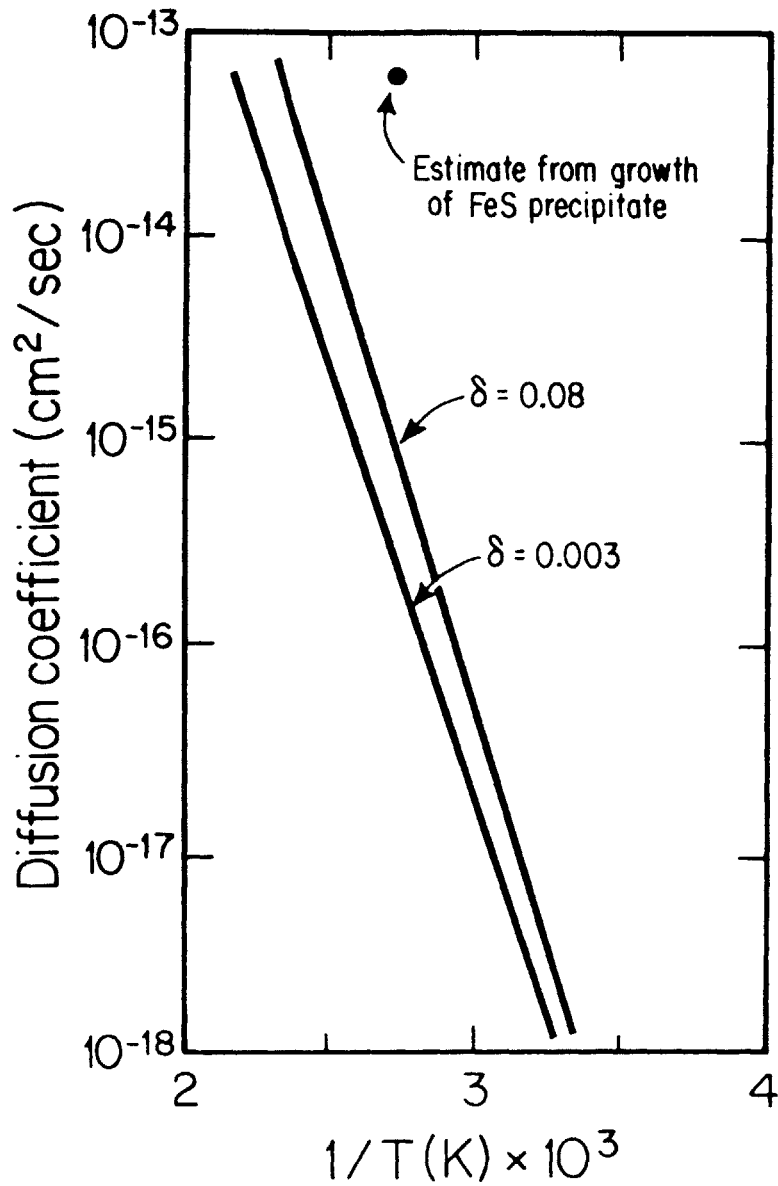
Figure 2.16. Iron self-diffusion in $Fe_{1-x}S$ extrapolated from the high temperature study of Condit et al. Black circle is a value of iron self-diffusion estimated from the study of growth of FeS precipitates (see Section 6.4).

References

* Troilite is named after Dominico Troili who described a meteorite that fell in Modelena, Italy in 1766.

Alsen, N., Geol. Fören. Stockh. Förh., 47, 19-22 (1925).

Bennett, C. E. G. and Graham, H., Amer. Miner. 66, 1254-1257 (1977).

Bertaut, E. F., Bull. Soc. Franc. Miner. Crist. 79, 276-292 (1956).

Bertaut, E. F., C. R. Acad. Sci., Paris, 234, 1245-1297 (1952).

Bertaut, E. F., Acta Cryst. 6, 557-561 (1953).

Buerger, M. J., Amer. Miner. 32, 411-414 (1947).

Carpenter, R. H. and Desborough, G. A., Amer. Mineral. 49, 1350-1365 (1964).

Condit, R. H. et al., Oxid. Met. 8, 409-455 (1974).

Corlett, M., Z. Krist. 126, 124-134 (1968).

Corlett, M., Ph.D. thesis, University of Chicago (1964).

Desborough, G. A. and Carpenter, R. H., Econ. Geol. 60, 1431-1450 (1965).

Engel, R., et al., Amer. Miner. 63, 1274-77 (1978).

Evans, H., Science 167, 621-623 (1970). 124-134 (1968).

Fleet, M. E., Can. Jour. Earth. Sciences 5, 1183-85 (1968).

Francis, C. and Craig, J., Amer. Miner. 61, 21-25 (1976).

Goodenough, J. B., Mat. Res. Bull. 13, 1305 (1978).

Hagg, G. and Sucksdorf, I., Z. Physik Chem. B22, 444 (1933).

Keller-Besrest, F. et al., Acta Cryst. B39, 296-303 (1983).

King, H. E. and Prewitt, C. T., Acta Cryst. 38, 1877-1887 (1982).

Kissin, S. A. and Scott, S. D., Econ. Geol. 77, 1739-1754 (1982).

Koto, K. et al., Acta Cryst. B31, 2759-2764 (1975).

Laves, F., Z. Kristallagr. 73, 275-325 (1930).

Liliental, Z. et al., in the 39 Annual EMSA Meeting (1981), pp. 60-61.

Lotgering, F. K., Philips Res. Reports 11, 190 (1956).

Marusak, L. A. and Mulay, L. N., J. Appl. Phys. 50(3), 1865-1867 (1979).

Marusak, L. A. and Mulay, L. N., Phys. Rev. B, 21, 238-244 (1980).

Marusak, L. A., Ph. D. Thesis, The Pennsylvania State University, University Park, Pennsylvania (1979).

Minagawa, T., Acta Cryst. A28, 308-318 (1972).

Morimoto, N. et al., Amer. Miner. 60, 240-248 (1975).

Morimoto, N. et al., Econ. Geol. 70, 824-833 (1975).

Morimoto, N. et al., Proc. Japan Acad. 50, 756-759 (1974).

Morimoto, N. et al., Science 168, 964-966 (1970).

Morimoto, N., Recent. Prog. Nat. Sci. Japan 3, 183-206 (1978).

Morimoto, N., Soc. Mining Geol. Japan Spec. Issue 2, 15-21 (1971).

Nakano, A. et al., Acta Cryst. B35, 722-724 (1979).

Nakazawa, H. and Morimoto, N., Mat. Res. Bull. 6, 345-358 (1971).

Nakazawa, H. and Morimoto, N., Proc. Japan Acad. 46, 678-683 (1970).

Nakazawa, H., and Morimoto, N., Mineral Soc. Japan Special Paper 1, 52-55 (1971).

Nakazawa, H. et al., in Electron Microscopy in Mineralogy. Edited by Wenk, H. R. et al. (Springer-Verlag) 1976.

Nakazawa, H. et al., in Eighth International Congress in Electron Microscopy, Canberra 1 (1974).

Ovanesyan, N. S. et al., Soviet Physics JETP 33, 1193-1197 (1971).

Pierce, L. and Buseck, P., Science 186, 1209-1217 (1974).

Pierce, L. and Buseck, P., in Electron Microscopy in Mineralogy (Springer-Verlag) 1976.

Putnis, A., Contrib. Mineral. Petrol. 52, 307-313 (1975).

Putnis, A., Phil. Mag. 31, 689-95 (1975).

Putnis, A., Science 186, 439-40 (1975).

Schwarz, E. J. and Vaughan D. J., J. Geomag. Geoelectr. 24, 441-458, (1972).

Spark, J. T. et al., J. Phys. Soc. Japan 17 (Suppl. 1), 249 (1962).

Sugaki, A. and Shima, H., Tokohu Univ. Sci. Rept., ser 3, 13, 147-163 (1977).

Sugaki, A. et al., Tokohu Univ. Sci. Rept., ser 3, 13, 165-182 (1977).

Thiel, R. C., Phys. Stat. Sol. 40, K17 (1970).

Thiel, R. C., and Van den Berg, C. B., Phys. Stat. Sol. 29, 837 (1968).

Tokonami, M. et al., Amer. Miner. 57, 1066-1080 (1972).

Van Landuyt, J. and Amelinckx, S., Mat. Res. Bull. 7, 71-80 (1972).

Wuensch, B. J., Miner. Soc. Am. Special Paper 1, 156-163 (1963).

Yamamoto, A. and Nakazawa, H., Acta Cryst. A38, 79-89 (1982).

Yund, K. A. and Hall, K. T., Mat. Res. Bull. 3, 779-784 (1968).

CHAPTER 3

PLAN OF RESEARCH

There are three major goals in this research: (1) resolve controversial and problematic aspects of the low temperature phase relations; (2) gain detailed information on the extent and mode of iron vacancy ordering and (3) gain information on the phase transformation mechanisms to better understand the thermodynamic and kinetic aspects in relation to the microstructures of the $Fe_{1-x}S$ crystals.

The phase relations and phase transformations of $Fe_{1-x}S$ were studied using various techniques of transmission electron microscopy and x-ray diffraction. *In situ* heating experiments were carried out in order to determine the phase relations and to study the phase transformations. Considerable efforts were devoted to the investigation of the phase transformations occuring in the composition range from FeS to $Fe_{0.92}S$. The extent and modes of vacancy ordering were investigated by high resolution transmission electron microscopy and diffraction techniques. The Arnold-Reichen-d_{102} method of compositional determination was used since no analytical methods satisfy the requirement of a 0.2 wt % composition resolution. Image simulations were used extensively to aid the image interpretation of the high resolution transmission electron micrographs.

Exceptionally high quality synthetic single $Fe_{1-x}S$ crystals (0<x<0.1) were used in this study. These crystals were obtained from Dr. R.A. McKee (grown by Dr. J.V. Cathcart) of the Oak Ridge National Laboratory. Throughout this investigation the thermal histories of samples studied were meticulously followed. The effects of sample preparation were carefully investigated to ensure that the TEM-transparent samples preserved the microstructures of the bulk materials.

Because of the potential structural damage and heating due to the high energy electron irradiation, all events occuring during a TEM session were scrupulously monitored to detect any deleterious effects.

CHAPTER 4

MATERIALS, PROCEDURES, DEFINITIONS AND NOTATION CONVENTION.

The following two chapters are devoted to the discussion of experimental techniques and interpretation of data acquired by this investigation. This chapter comprises four sections. The first presents the thermal and synthesis history of the iron sulfide compounds. The second section focusses on the methods used in the characterization of $Fe_{1-x}S$. This includes the Arnold-Reichen-d_{102} method of compositional determination. Detailed description of the TEM sample preparation and techniques will also be given in this section. The third section supplies important definitions and nomenclatures used in the following chapters. This chapter ends with a section on the notation convention employed in this thesis. Chapter 5 will concentrate on the interpretation of high resolution transmission electron micrographs.

4.1 THERMAL AND SYNTHESIS HISTORY OF $Fe_{1-x}S$.

Both synthetic and natural iron sulfide compounds were used in the investigation of the phase relations and defect structures of $Fe_{1-x}S$. Table 4.1 lists the history of the materials used in this investigation.

Synthetic "single" crystals were grown by Carthcart et al. (1982) using a modified Bridgeman technique. The starting materials are 99.9999% pure sulfur and "Marz" grade iron *. The crystals are grown in 100 mm long, 15 mm wide and 10 mm

deep boron nitride boats. After the freezing process, the $Fe_{1-x}S$ crystal is given a 48 hour homogenization anneal at 1198 K with p_{S2} being maintained at 10^2 Pa. The crystal's temperature is brought down to 898K by lowering the temperature of the furnaces in increments of 10-20K while simultaneously adjusting the sulfur partial pressure to maintain a desired fixed composition. The $Fe_{1-x}S$ crystal is annealed at 898K for five days and then lowered to room temperature by turning off the furnaces. The crystals are relatively free from defects. Only two dislocation loops were observed in more than 20 TEM samples. The composition of the crystal, however, is inhomogeneous due to the nature of the phase diagram (see Chapters 6 and 7). A very detailed description of the crystal growth technique of $Fe_{1-x}S$ can be found in the paper by Cathcart et al. (1982).

Synthetic polycrystalline $Fe_{1-x}S$ crystals were produced by sulfidizing to completion the "Marz" grade iron at 989K and with the sulfur partial pressure at 10 Pa. The composition of the materials produced by this method is $Fe_{0.9}S$.

Natural iron sulfide compounds were obtained from Santa Eulalia district in Chihuahua, Mexico and from Villa Rica, Brazil (American Museum of Natural History No. 1449). The natural iron sulfide compounds have an average composition of $Fe_{0.875}S$ (see Section 4.2.1). These compounds are also magnetic. Pyrite FeS_2 precipitates were observed in the Mexico pyrrhotite.

4.2   METHODS OF CHARACTERIZATION

4.2.1 THE ARNOLD-REICHEN METHOD OF COMPOSITIONAL DETERMINATION

The range of composition of iron sulfide compounds from FeS to Fe_7S_8 is very narrow. The difference in composition from troilite FeS (63.53 wt % Fe) to monoclinic pyrrhotite Fe_7S_8 (60.38 wt % Fe) is 3.15 wt % Fe. "Hexagonal" pyrrhotite

61

$Fe_{11}S_{12}$ (61.49 wt % Fe) and $Fe_{10}S_{11}$ (61.29 wt % Fe) differ by only 0.2 wt % Fe. The study of iron sulfide compounds in this composition range requires an ability to differentiate metal composition of 0.2 wt %. This requirement in compositional resolution, however, has not been achieved by modern analytical instruments (electron microprobe and scanning transmission electron microscope have compositional resolution of about 1 wt %).

An accepted technique for determining the composition of pyrrhotite has been described by Arnold and Reichen (1962) and subsequently "refined" by several other investigators (Yund and Hall 1969; Morimoto et al. 1975). This method established an empirical curve relating the $d_{10.2}$ spacing (henceforth d_{102}) to the metal content of pyrrhotite (Figure 4.1). Arnold and Reichen (1962) and Yund and Hall (1969) suggested that this method is accurate to 0.25 at % and 0.13 at % respectively.

A number of difficulties, however, are inherent in the measurement of d_{102} spacing. The d_{102} reflection is a single sharp peak only when it is immediately measured from pyrrhotite that is quenched from high temperature (above 623K). Without annealing at high temperature, the d_{102} peak often splits into several components for samples measured at temperature below 623 K. At temperature below T_α (see Figure 6.8 for definition of T_α), there are two "d_{102}" peaks in the composition range from FeS to $Fe_{0.92}S$. These peaks have been associated with the d_{102} reflections of the low temperature phases. In the composition range from $Fe_{0.92}S$ to $Fe_{0.9}S$, the d_{102} reflection remains a single sharp peak at all temperatures. The d_{102} reflection splits into several peaks (Figure 4.2) for samples of composition ranging from Fe_8S_9 to $Fe_{0.875}S$. The splittings are due to the low symmetry of the crystal and compositional inhomogeneity. A common procedure that is often used to obtain an average composition is annealing the sample above 650 K and measuring the d_{102} spacing of the quenched product (see Figure 4.2b). The annealing removes the splitting of the d_{102} reflection. Two other complications that often limit the

accuracy of the measument of the d_{102} spacing are the convolution of the $K_{\alpha 1}$ and $K_{\alpha 2}$ lines with the d_{102} reflection and the peak broadening due to mechnical damage incurred during the grinding. TEM studies of crushed iron sulfide have revealed extensive subgrain formation in an otherwise perfect single crystal (Figure 4.3).

In this investigation, the composition of iron sulfide compounds was also determined by the Arnold-Reichen empirical method. The powder x-ray d_{102} reflection was obtained using $CuK\alpha$ radiation. Powder silicon ($a_0 = 5.43088\overset{o}{A}$) was used as an internal standard. In the composition range from FeS to $Fe_{0.92}S$ and from $Fe_{0.9}S$ to $Fe_{0.875}S$, the average composition of $Fe_{1-x}S$ was determined from the d_{102} measurement of annealed sample. The sample was annealed at 698K for 15 minutes in a sealed ,evacuated Vicor tube.

4.2.2 TEM SAMPLE PREPARATION

Samples for TEM were prepared by the following methods:

1) $Fe_{1-x}S$ crystals are crushed using a mortar and pestle and dispersed in trichloroethane. The $Fe_{1-x}S$ powder is deposited onto 200 mesh Cu grid that is coated with a very thin layer of lacy carbon film by dripping the solution over the Cu grid. This sample preparation method is simple and fast. However, it has a number of drawbacks. The crushing causes mechanical damage. Extensive dislocation activitiy and subgrains are observed in an othewise perfect crystal. Poor contact between the crushed specimen and the carbon film can cause severe electron beam heating. The sample's temperature can increase up to 1488 K!.

63

2) $Fe_{1-x}S$ crystals are cut into 3mm disks, mechanically thinned, dimpled and ion thinned to electron transparancy. The $Fe_{1-x}S$ disk is usually dimpled to 50 µm thick. The ion thinning is carried out either at prebeam temperatures of 298 K or 123 K.

There is a large difference in microstructures of room temperature and 123K ion thinned $Fe_{1-x}S$ (0<x<0.08) samples (Figure 4.4). It can be shown using the results described in Chapter 6 that ion thinning at 298K raises the sample's temperature above the transformation temperature T_α. The microstructure shown in Figure 4.4a is generated by quenching the sample from temperature above T_α to room temperature. This quenching inevitably occurs immediately after the termination of ion thinning process. Ion thinning at 123 K minimizes the heating and preserves the original microstructure (Figure 4.4b).

4.2.3 ELECTRON MICROSCOPY

Electron microscopy was carried out using a Philips 300, two side-entry MIT JEOL JEM 200CX transmission electron microscopes at MIT, a top-entry JEOL JEM 200CX and a top-entry JEOL JEM 4000EX transmission electron microscopes at Arizona State University (ASU). Relevant microscopic parameters are listed in Table 4.2. Conventional transmission electron microscopy was performed using the standard 2-beam condition bright field and dark field technique (Hirsch et al. 1977). High resolution transmission electron microscopy was carried out in the axial illumination mode. The electron optical parameters listed in Table 4.2 were measured by an optical diffractometry technique (Krivanek, O.L. 1976; Spence, J.C.H. 1981). Considerable care was taken in the beam and crystal tilt alignment to avoid the undesirable effects which were thoroughly discussed by Smith et al. (1983).

The *in situ* heating experiments were carried out using a Gatan single tilt and a JEOL STH-10 double tilt heating stages. The hot stage thermocouple was calibrated at 530K and at room temperature. 530K is the melting temperature of tin. The error in temperature measurement at the sample is estimated to be within 10K.

Damage and local heating due to the high energy electron bombarment were major concerns in this investigation. No damage was observed below 200 kV. At 400 kV, the high energy electrons disorder the iron vacancies in about 10 minutes (beam current density is estimated to be about 1×10^4 A/m^2). The stoichiometric FeS, however, appeared to remain undamaged. The electron beam heating can be very severe. Local heating up to 600K was observed in crushed samples (see Chapter 7) during high resolution transmission electron microscopy. The extent of the electron beam heating depends on the contact between the crushed specimen and the carbon film. In disk sample that has good contact between sample and micoscope stage, the electron beam heating effect depends strongly on the thermal conductivity of the material studied. Iron sulfide compounds are either good semiconductors or poor electrical conducting metals, hence they are good thermal conductors. The elevation in specimen's temperature is therefore minimal (<10K). A thorough discussion of the beam heating effect can be found in a paper by Hobbs (1984).

4.2.4 MAGNETIC CHARACTERIZATION

The magnetism of pyrrhotite was determined using a permanent magnet and a DMS Model 880A vibrating sample magnetometer.

4.3 DEFINITIONS

Definitions of a number of terms used in this thesis have not been clearly defined in the literature. In order to avoid possible misunderstanding we define the following concepts:

A thermodynamic system is the portion of the universe selected for analysis.

A thermodynamic property is a measurable macroscopic quantity associated with the system .

A thermodynamic state is specified by a set of values of all the thermodynamic properties necessary for the description of the system.

Equilibrium - A system is in equilibrium state if a finite change in any property of the system cannot occur without the change of the corresponding magnitude in the surroundings.

A phase is a finite region in the thermodynamic system across which all of the properties are uniformly constant .

The equation of state is a functional relationship among the intensive thermodynamic properties of a system in equilibrium .

A thermodynamic transformation is a change of state that accompanied by a singularity in the behavior of the thermodynamic properties.

The composition-temperature diagram or "phase diagram" of a system is the projection of the surface of the equation of state onto the composition-temperature plane.

4.4 NOTATION CONVENTION

This study investigates a number of different structures. These structures possess different space group symmetries. The Miller index notation for lattice

66

directions and planes is based on the unit cell edge of a crystal structure. Consequently, these indices are different for different structures. For example, the unit cell edges for the 1C NiAs structure are parallel to the a_1, a_2 and c directions of the hexagonal lattice (Figure 4.5). However, the a_1' and a_2' edges of the 2C troilite unit cell make a 30° angle with the a_1 and a_2 directions of the hexagonal system. This means that when one says the [120] direction for the troilite structure one means the [100] direction in the NiAs system (see Figure 4.5). This can be very confusing when these two phases coexist. In order to avoid misunderstanding, the following convension is used.

(1)   The four index Miller-Bravais convention is always used to describe lattice directions. The reference unit cell used in this indexing scheme is the NiAs cell.

(2)   In cases where it is desirable to use the structure 's own indexing system, the Miller indices of that structure will be given first. Immediately following them, the Miller-Bravais indices prescribed by (1) will be given. These two indices are separated by a bar.

e.g. $[120]|[\bar{1}010]$

(3)   The superstructure reflections are always indexed by their own Miller indices.

Finally, a Kikuchi map for a close-packed hexagonal crystal extending over one standard triangle and important electron diffraction patterns of $Fe_{1-x}S$ crystal are shown in Figure 4.6.

SAMPLE	TYPE	DATE	COMMENTS
FeSMIT	Synthetic single crystal	5/15/80	Two phase mixture, FeS + Fe0.92S Also known as FeS116
MIT2	Synthetic	1982	Sulfidation of iron coupon to completion Sulfur partial pressure 10Pa at 700 K $Fe_{0.9}S$
FeS110	Synthetic single crystal	1/5/82	$Fe_{0.9}S$
FeSMex	Natural	unknown	Fe_7S_8 from Santa Eulalia district in Chihuahua, Mexico
FeSBra	Natural	unknown	Fe_7S_8 from Villa Rica, Brazil Amer. Mus. Nat. Hist. No 1149

Table 4.1. History of materials used in this investigation.

	JEM 200CX (MIT)	JEM 200CX(ASU)	JEM 4000EX(ASU)
Accel. Voltage	200kV	200kV	400kV
Resolution (WPO)	3.1A	2.5A	1.7A
Spherical Aberration C_s	2.9mm	1.2mm	1 mm
Focal Spread Half Width (from Image Simulation)	100A	100A	100A
Divergence Half Angle θ	0.5 mrad	0.5 mrad	0.8 mrad
Aperture Radius	0.4 A^{-1}	0.5 A^{-1}	0.7 A^{-1}

Table 4.2. Electron optical parameters of microscopes used in this investigation.
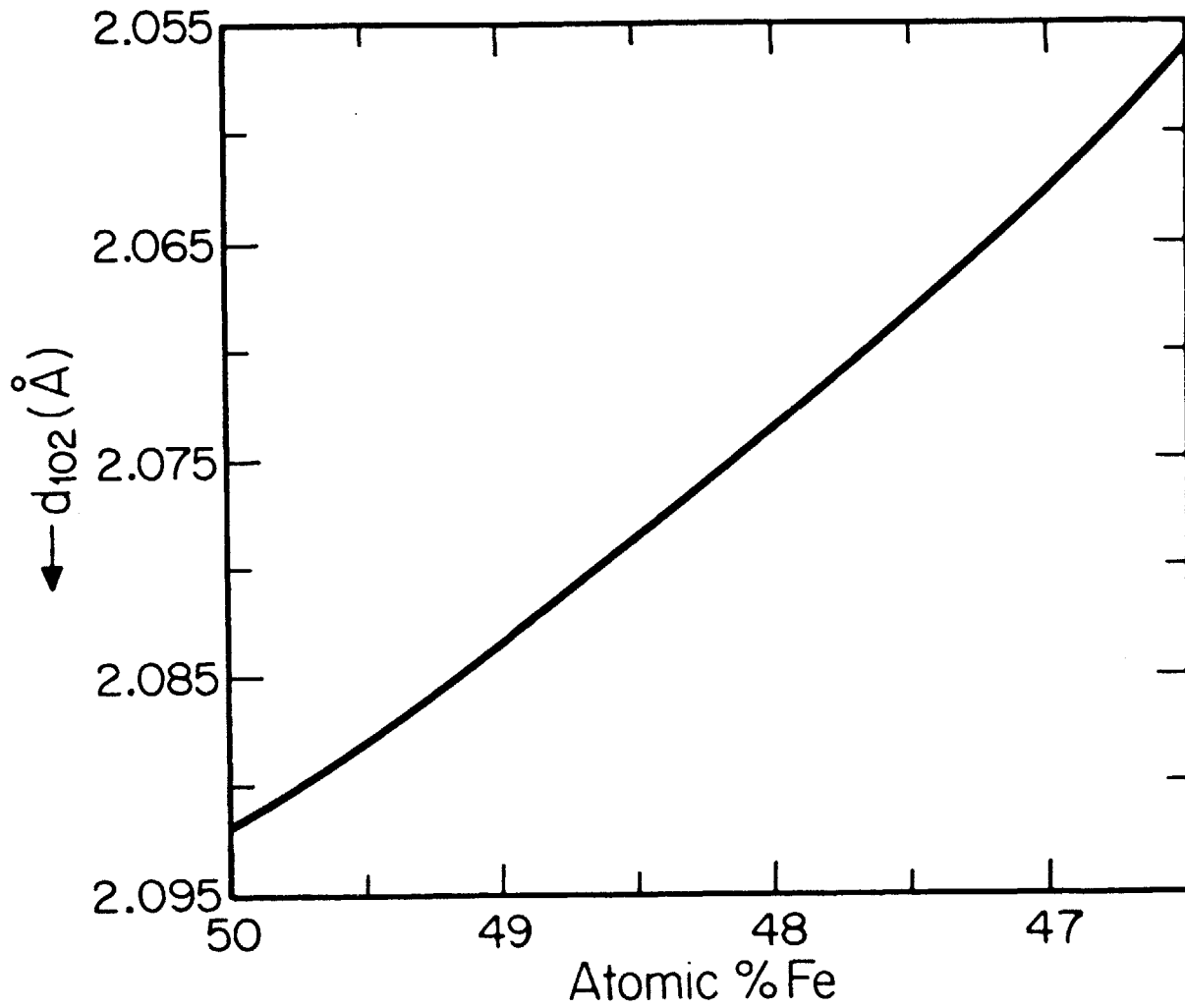
Figure 4.1. The Arnold-Reichen metal composition versus d_{102} curve.
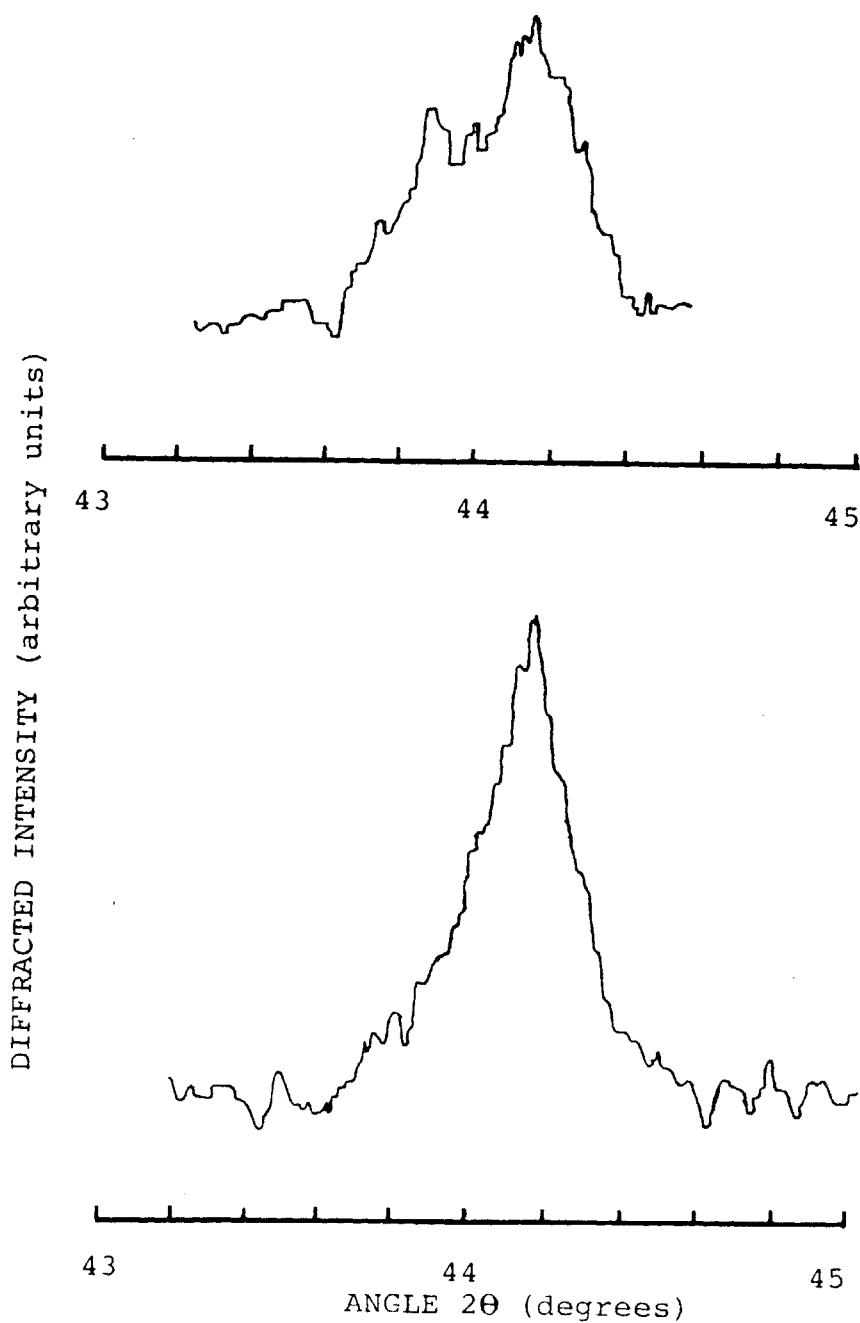
Figure 4.2. The powder x-ray diffraction patterns of d_{102} reflection. (a) d_{102} reflection before annealing. (b) d_{102} reflection after annealing at 650 K for 15 minutes in vacuum.
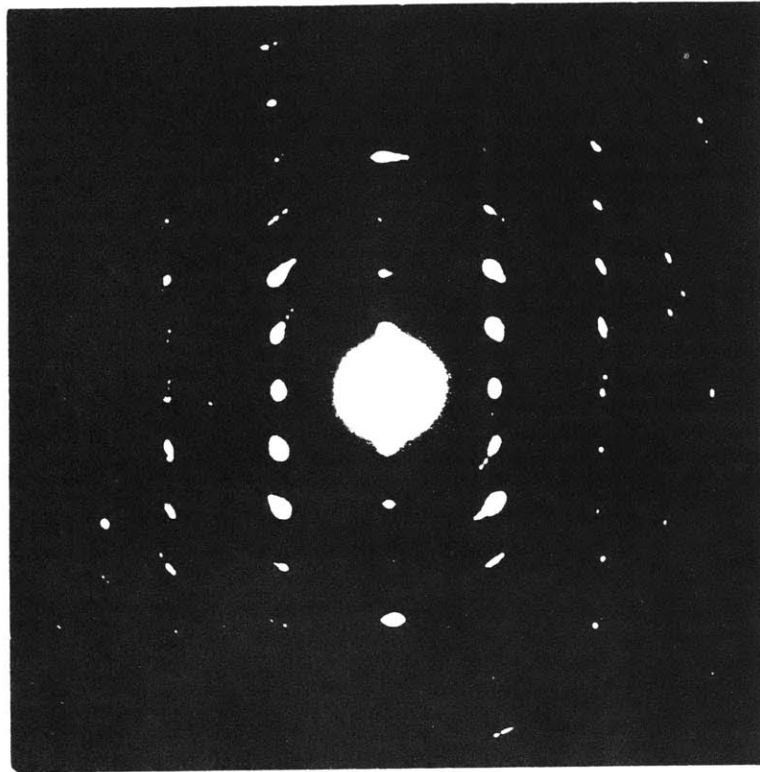
Figure 4.3. Arc reflections indicate the presence of low angle grain boundaries.
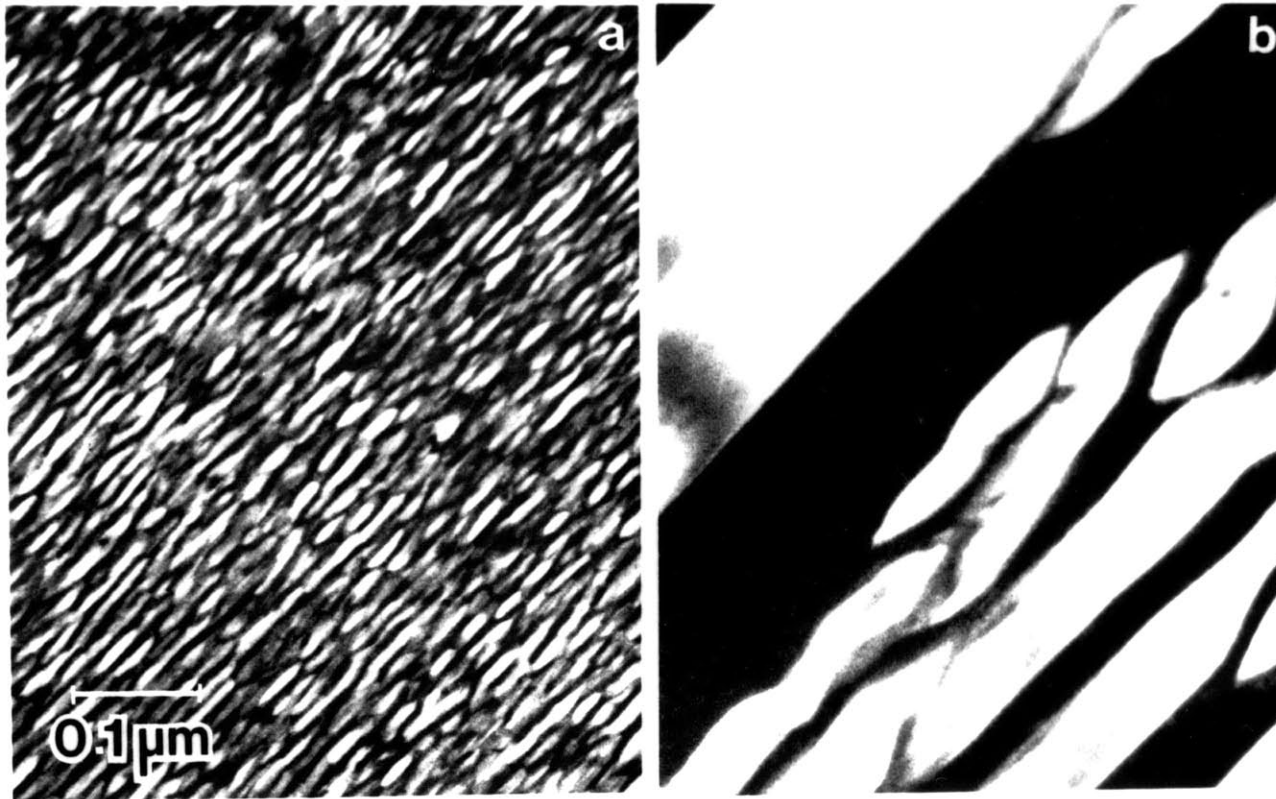
Figure 4.4. Microstructure of a mixture of FeS and $Fe_{0.92}S$ ion thinned (a) at room temperature (b) at 123 K.

NiAs [100]
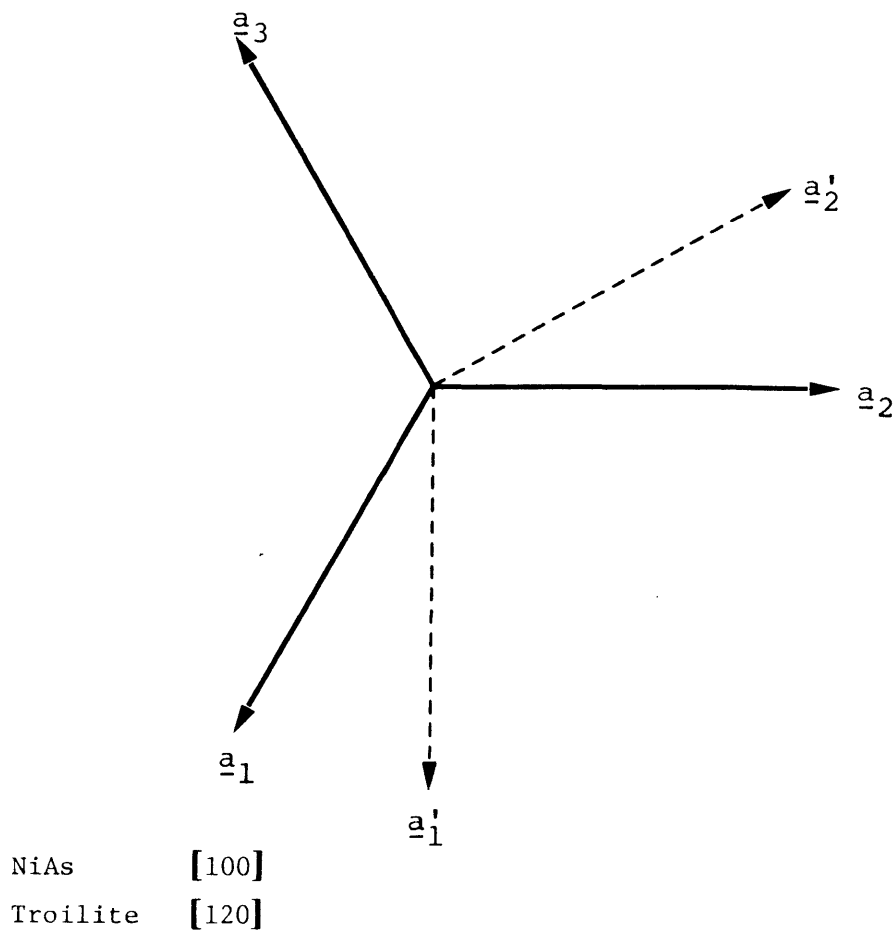
Troilite [120]

Figure 4.5. NiAs crystal axes a_1, a_2, a_3 and troilite crystal axes a_1', a_2'.

Figure 4.6. Schematic skecth of a Kikuchi map for a close-packed hexagonal crystal extending over one standard triangle. The electron diffraction patterns are those of $Fe_{1-x}S$ crystal.

References

Arnold, G. R. and Reichen, L. E., Amer. Mineral. 49, 1350-1365 (1964).

Cathcart, J. V. et al., J. Crystal Growth 62, 299-308 (1982).

Hobbs, L. W., in Quantitative Electron Microscopy, (Chapman, J. N. and Craven,A. J.,

eds.), The Scottish Universities Summer School in Physics, 399-445 (1983).

Krivanek, O. L., Optik 45, 97 (1976).

Morimoto et al., Amer. Miner. 60, 240-248 (1975).

Smith, D. J., Ultramicroscopy 11, 263-282 (1983).

Spence, J. C. H., Experimental High-Resolution Electron Microscopy, Oxford University

Press, Oxford (1980).

Yund, K. A. and Hall, K. T., Mat. Res. Bull. 3, 779-784 (1968).

CHAPTER 5

IMAGE INTERPRETATION IN HIGH RESOLUTION TRANSMISSION ELECTRON MICROSCOPY

High resolution transmission electron microscopy is an important investigative tool used in this study of the defect structures of iron sulfide compounds. Accurate interpretation of high resolution electron micrographs is therefore crucial to the effort of deducing these defect structures. In this chapter, we will examine important aspects of image interpretation in high resolution transmission electron microscopy. A general procedure for image interpretation and critical discussion of image contrast reversal and Fourier image phenomena will be given.

5.1 INTRODUCTION

A simplistic approach to the image interpretation of high resolution electron micrographs assumes that the interaction between the electron wave and the material is kinematical (i.e. weak phase object approximation) so that the square of the object transmission function or of the electron wave at the exit face of a TEM specimen can be related directly to the projected electrostatic potential of the material studied (Spence 1981; Cowley 1979). The electron microscope, under this assumption, functions only as a magnification device. In its optimal operating condition, the electron microscope faithfully magnifies the electron wave signal to a level at which features separated by distance greater than the "point" resolution of the microscope can be resolved. The high resolution electron micrograph is simply the convolution of the transmission function and a gaussian shaped impulse response

function.   Models of structures can be accepted or rejected by direct comparison with the experimental images.   The above experimental conditions, unfortunately, cannot be achieved.   The incident electron wave interacts strongly with the object potential, and the kinematical approximation is invalid for most materials with thickness greater than 10Å.   Inelastic and multiple scattering phenomena are more often the dominant processes.   A direct relationship between the square of the transmission function and the projected potential of a structure therefore occurs only in very special (and fortuitous) circumstances.   Neither is the electron microscope a perfect magnification device.   Imperfections, such as spherical aberration, defocus, lack of spatial and temporal coherence, alter the amplitude and phase of the electron wave. The modification of the wave function can be so severe that features separated by distance greater than the "point" resolution of an electron microscope can no longer be reliably interpreted without the aid of reference image calculations.

In this chapter we seek to establish a rigorous physical basis for interpreting high-resolution transmission electron microscopic images. The approach involves acquiring a detailed understanding of interactions between (Figure 5. 1)

1) incident electron wave and the material studied ;

2) the propagation of the transmitted wave in free space and the   imperfections of a high resolution transmission electron microscope.

These different aspects of image formation and interpretation are organized into four sections.   The first section comprises a detailed derivation of the electron wave function as it propagates through and interacts with the material studied.   A computational procedure used in obtaining the transmission function will be described in detail.   The second section consists of a delineation of the imperfections of a high resolution transmission electron microscope and their influences on the transmission function. A precise definition of the "point" resolution

of an electron microscope will be given. The third section discusses the computational procedure used in the simulation of high resolution lattice images; these programs (SHRLI programs) calculate the transmission functions and images. The last sections of this chapter describes the image interpretation employed in the analysis of our experimental results.

5.2   PHYSICS OF IMAGE FORMATION

5.2.1   LITERATURE REVIEW

The problem of electron scattering in a crystal and the solution for the scattering electron wave function have been investigated by various theoretical methods during the past sixty years. In 1928, Bethe developed the dynamical theory of electron diffraction using the quantum mechanical Schrodinger equation. Since then, alternative theoretical approaches have also been developed to investigate the dynamical scattering of electrons. These have included the scattering-matrix method (Sturkey 1962) and the wave optical method which is similar to the X-ray diffraction theory of Darwin (Howie and Whelan 1961). The methods of Bethe, Sturkey, Howie and Whelan, however, give electron wave functions that are highly complicated and computationally impractical in cases where many diffracted beams are required (Humphreys 1979, Self et al. 1983). An alternative approach to the dynamical scattering problem has been proposed by Cowley and Moodie (Cowley and Moodie, 1957-1959). Their solution, often known as the multislice approximation, is based on the "physical-optics" arguments and is computionally tractable when many diffracted beams are considered. The physical optics approach, however, lacks the physical rigor of a first principle quantum-mechanical approach. Efforts to justify the multislice approximation rigorously have been made recently using the Green's

function method (Ishizuka and Uyeda 1977), semi-classical method (Berry 1971), time-like perturbation method (Gratias and Portier 1983), and Feynman path integral method (Van Dyck 1975, Jap and Glaeser 1979). The Feynman path-integral method is a quantum-mechanical and physically intuitive approach. The papers by Van Dyck, Jap and Glaeser, however, have serious deficiencies in their derivations of the Cowley-Moodie equations. In the next sub-section, we rederive the Cowley-Moodie equation and the multislice calculation using the path-integral formalism. The path-integral can be shown to be equivalent to the Schödinger formalism (Shankar 1980).

5.2.2 DYNAMICAL SCATTERING OF HIGH ENERGY ELECTRONS IN A MATERIAL

Incident high-energy electrons interact with a material through various mechanisms such as electrostatic, exchange and spin-spin interactions. The magnitude of the electrostatic interaction is much larger then all other interactions when the incident electron energy is greater than 50 keV (Rez 1978, Whelan 1962). This means that in the case of high energy electrons, the only interaction term needed in the Lagrangian is the Coulombic potential. The high energy of the incident electron also implies that relativistic effects are important. Fujiwara (1962) and Whelan (1962) have shown that the relativistic effects are adequately taken into account if the appropriate relativistic corrections to the electron mass and wavelength are made.

An electron wave propagating through a material can be described by a space integral of the product of the initial wave function and a propagator (Feynman and Hibbs 1965, Sakurai 1985)

$$\psi(\underline{r},\ t\ ;\ \underline{r}_0,\ t_0) = \int d\underline{r}_0\ \psi(\underline{r}_0\ ,\ t_0)\ K(\underline{r},\ t;\ \underline{r}_0,\ t_0) \qquad (5.1)$$

where $\psi(r_0, t_0)$ is the initial wave function at position r_0 and time t_0, and $K(r, t; r_0, t_0)$, often known as the kernel or propagator, is the transition amplitude from location r_0 and time t_0 to location r and time t. The kernel has the form

$$K(r, t ; r_0, t_0) = \int_{r_0}^{r} \exp\left(\frac{i}{\hbar} S(r, r_0)\right) \mathcal{D}[r(t)],$$ (5.2)

where $\int_{r_0}^{r} \mathcal{D}[r(t)]$ is a symbolic way of saying "integrate over all paths connecting r_0 and r in the interval t_0 to t, and $S(r, r_0)$ is the classical action given by

$$S(r, r_0) = \int_{t_0}^{t} L(r, \dot{r}, t') dt',$$ (5.3)

where $L(r, \dot{r}, t)$ is the Lagrangian. In our case, $L(r, \dot{r}, t)$ has the form

$$L(r, \dot{r}, t) = 1/2\, m\, \dot{r}^2 - eV(r),$$ (5.4)

where $eV(r)$ is the electron potential energy.

We assume that the incident electron wave is a unit amplitude plane wave i.e. $\psi(r_0, t_0) = \exp(i2\pi k_0 \cdot r_0)$ and the coordinate system is chosen so that the origin coincides with the top surface of the material studied. This means that

$$\psi(r, z=0, t) = 1.$$

The solution of the electron wave function is known if we know the kernel

$$K(r, t; r_0, t) = \int_{r_0}^{r} \exp\left\{ \frac{i}{\hbar} \int_{t_0}^{t} \left(\frac{1}{2} m\dot{r}^2 - eV(r) \right) dt' \right\} \mathcal{D}[r(t)].$$ (5.5)

In general, the integral (5.5), integrated over all possible paths, can be evaluated analytically for only a few special potentials such as constant or parabolic potentials. Nevertheless, we can evaluate (5.5) for any well-defined potentials by partitioning the spatial change of the true potential into a series of constant potentials. That is, we partition the crystal into parallelopiped cells (Figure 5.2) such that the potential change within the cell is small and therefore can be approximated by a constant potential. For a constant potential, the kernel can be shown to have the form (Feynman and Hibbs 1965, Shankar 1980)

$$K(\underline{r}, t; \underline{r}_0, t_0) = \exp\left[-\frac{i}{\hbar}\int_{t_0}^{t}\frac{1}{2}m\dot{\underline{r}}^2 dt' - \frac{i}{\hbar}\int_{t_0}^{t}eV(r)dt'\right]_{\text{classical path}} ; \qquad (5.6)$$

using the fact that the potential is constant with a cell

$$dt' = -\frac{1}{v}dr' \qquad (5.7)$$

where v is the electron velocity. The kernel becomes

$$K(\underline{r}, t; \underline{r}_0, t_0) = \exp\left[-\frac{i}{\hbar}\int_{t_0}^{t}\frac{1}{2}m\dot{\underline{r}}^2 dt'\right]\exp\left[-\frac{i}{\hbar v}\int_{r_0}^{r}eV(\underline{r}')dr'\right]. \qquad (5.8)$$

The first exponential on the right hand side of (5.8) is the propagator of a free electron. It can be shown to be equal to (Feynman and Hibbs 1965)

$$\exp\left[-\frac{i}{\hbar}\int_{t_0}^{t}\frac{1}{2}m\dot{\underline{r}}^2 dt'\right] = \frac{m}{2\pi\hbar i(t-t_0)}\exp\left[\frac{im(r-r_0)^2}{2\hbar(t-t_0)}\right]. \qquad (5.9)$$

Using the fact that $\dfrac{r-r_0}{t-t_0} = v$ and substituting (5.9) into (5.8), we get

$$K(\underline{r}, t; \underline{r}_0, t_0) = \text{constant} \exp\left[\frac{imv(r-r_0)}{2\hbar}\right]\exp\left[-\frac{i}{\hbar v}\int_{r_0}^{r}eV(\underline{r}')dr'\right]. \qquad (5.10)$$

83

Using relation $mv = \dfrac{h}{\lambda} = hk$ and dropping the constant, (5.10) becomes

$$K(\underline{r}, t; \underline{r}_0, t_0) = \exp\left[\, i\pi k(r-r_0)\,\right] \exp\left[\frac{i}{\hbar v}\int_{r_0}^{r} eV(\underline{r}')dr'\right]. \qquad (5.11)$$

The scattering angle for high energy electrons is typically less than $2°$ and therefore to a good approximation $r - r_0 = H$, where H is the thickness of the crystal. Define a projected potential $V_p = \int_0^H V\, dz$ and the shorthand notations

$$\sigma = -\frac{1}{\hbar v}$$

$$A = \exp\left[\, -i\pi kH\,\right],$$

the kernel has the form

$$K(\underline{r}, t; \underline{r}_0, t_0) \equiv \psi(\underline{r}) = A e^{i\sigma V_p}. \qquad (5.12)$$

This is the well known phase object approximation.

Thus far, we have found the kernel or wave function for a high-energy electron wave propagating through a constant potential. We next approximate the true potential of a material by a series of constant potential steps. This approximation can be implemented by dividing the crystal into n-slices of thickness ΔZ (see Figure 5.2). Each slice is further subdivided into parallelepiped cells whose dimensions are small enough so that the potential within a cell can be approximated by a constant. The electron wave function propagating through the material can be found by successively calculating the electron wave at the exit face of each slice using (5.1).

The electron wave at the exit face of the $(n+1)$th slice is

$$\psi_{n+1}(x_{n+1}, y_{n+1}) = \int \psi_n(x_n, y_n) \, K(r_{n+1}, r_n) \, dx_n dy_n \tag{5.13}$$

where ψ_{n+1} and ψ_n are respectively the transmitted wave functions emerging from the exit face of the $(n+1)$th and nth slices. The kernel has the usual form

$$K(r_{n+1}, t_{n+1}; r_n, t_n) = \exp\left[-i\pi k(r_{n+1} - r_n) \right] \exp\left[-i\sigma \int_{r_n}^{r_{n+1}} V(r)dr \right]. \tag{5.14}$$

When the electron wave impinges on a new slice of material, the wave can either be transmitted or scattered (see Figure 5.3). The path length difference between the transmitted and diffracted beams is

$$\Delta_{n+1} = \left[R_{n+1}^2 (\rho_{n+1}, \rho_n') + (\Delta Z_{n+1})^2 \right]^{\frac{1}{2}} - \Delta Z_{n+1} \tag{5.15}$$

where $R_{n+1}(\rho_{n+1}, \rho_n) = \left[(x_{n+1} - x_n')^2 + (y_{n+1} - y_n')^2 \right]^{\frac{1}{2}}$

$$\rho = (x, y)$$

ΔZ_{n+1} = thickness of $(n+1)$th slice.

Since the scattering angle is small and the slice is thin we can expand the square root in (5.15)

$$\Delta_{n+1} \approx \Delta Z_{n+1} \left[1 + \left(\frac{R_{n+1}}{\Delta Z_{n+1}} \right)^2 \right]^{\frac{1}{2}} - \Delta Z_{n+1}$$

$$\approx \Delta Z_{n+1} + \frac{1}{2} \frac{R_{n+1}^2 (\rho_{n+1}, \rho_n)}{\Delta Z_{n+1}} - \Delta Z_{n+1}$$

$$\Delta_{n+1} = \frac{R_{n+1}^2(\rho_{n+1},\rho_n)}{2\Delta Z_{n+1}}.$$

(5.16)

Since $R_{n+1}(\rho_{n+1}, \rho_n') = \Delta Z_{n+1} \tan \theta_{n+1}$

$$\approx \Delta Z_{n+1} \, \theta_{n+1}$$

$$\Delta_{n+1} = \frac{\Delta Z_{n+1} \theta_{n+1}^2}{2}.$$

From Figure 5.3 we can see that the kernel of a path starting at r_n' and ending at r_{n+1} is

$$K(r_{n+1}, t; r_n', t') = \exp\left[-i\pi k(\Delta Z_{n+1} + \Delta_{n+1})\right] \exp\left[i\sigma\int_{Z_n}^{Z_{n+1}} eV(\rho_n', z')dz'\right], \quad (5.17)$$

where $\rho_n' = (x_n', y_n')$.

In (5.17), we have made the approximation that the integral of the potential along any non-parallel path is equal to that of a straight line path parallel to the beam direction. Substituting (5.16), (5.17) into (5.13) we have

$$\psi_{n+1}(\rho_{n+1}) = \int_{Z_n}^{Z_{n+1}} \psi_n(\rho_n') \exp\left[i\sigma\int eV(\rho_n, z')dz'\right] \exp\left[-i\pi k(\Delta Z_{n+1} + \frac{R_{n+1}^2(\rho_{n+1},\rho_n)}{2\Delta Z_{n+1}})\right]d\rho_n'.$$

(5.18)

The integral (5.18) should be limited to values which are associated with small angle path deviation in order to be consistent with our previous assumption. That is, the scattering angle is small. It turns out that for large angles, the path difference will be large and the phase change due to the difference in path length will oscillate rapidly. This means that the contribution to the integral from large angles will be insignificant. Therefore, the integral (5.18) can be performed over all possible

values without making any significant error in the transmitted wave function. Equation (5.18) can be rewritten in convolution form

$$\psi_{n+1}(\rho_{n+1}) = \exp(-i\pi k \Delta z) \left\{ \psi_n(\rho_n) * \exp\left(\frac{i\pi K(X^2+Y^2)}{2\Delta Z}\right) \right\} \exp(i\sigma) \int_{Z_n}^{Z_{n+1}} eV(\rho_{n+1}, z')dz'$$

(5,19)

where * represents a convolution.

Equation (5.19) is the recursive relation for the transmitted wave in the well-known multislice approximation. This equation tells us that the wave function ψ_{n+1} at the exit face of the (n+1)th slice is the convolution of the incident wave ψ_n and two phase shifts. The first phase shift comes from the potential and the second phase shift comes from the propagation through free space (i.e. Fresnel propagator).

Let $q_n = \exp(i\sigma V_\rho)$

$$p_n = \exp\left(\frac{i\pi K(X^2+Y^2)}{2\Delta Z}\right).$$

Neglecting the constant phase factor, (5.19) becomes

$$\psi_{n+1}(\rho_{n+1}) = (q_n^* \psi_n) p_n.$$

(5.20)

Therefore $\psi_1(\rho_1) = (q_0 * 1)p_0 = q_0 * p_0$ and the electron wave function at the exit face of a studied material can be obtained by iterating (5.20). It has the form (assume n-slices),

$$\psi(x,y) = q_n [...q_2 [q_1 [q_0 * p_0] * p_1] * p_2] * ...] p_n.$$

(5.21)

The above equation is the basis for the multislice dynamical calculation. For a crystal, the iteration in (5.21) is actually best performed in reciprocal space where the amplitude of the wave function is nonzero only at the discrete points of reciprocal lattice. Furthermore, the Fourier components of the wave function fall off with increasing order. This means that accurate calculation can be achieved by using only a finite number of Fourier coefficients (Goodman and Moodie 1974). The recursive relation (5.20) can be Fourier transformed to

$$\psi_{n+1}(\underline{U}) = \psi_n(\underline{U})\,\underline{P}_n(\underline{U}) * Q_n(\underline{U}). \qquad (5.22)$$

where $\underline{U} = \underline{j}u + \underline{j}v$

$$Q_n(\underline{U}) = F.T.[\,q(\rho)\,]$$

$$\underline{P}_n(\underline{U}) = F.T.[\,p_n(\rho)\,] = \exp[\,-i\lambda\pi\Delta z\,(u^2 + v^2)\,].$$

Here we assume that the reciprocal vectors a^* and b^* are orthogonal. The term $S_g = -\frac{\lambda}{2}(u^2 + v^2)$ is the excitation error for reflection (h, k). The Fourier transform of equation (5.21) is

$$\psi(U) = [\,Q(\underline{U}) * \cdots [\,Q_2 * [\,Q_1 * Q_0\,P_0\,]\,P_1\,]\,P_2 \cdots]\,P_n(\underline{U})\,]. \qquad (5.23)$$

The calculation procedure used to obtain the electron wave function is summarized in Figure 5.9.

88

5.3 MODIFICATION OF ELECTRON WAVE FROM IMPERFECTIONS IN A HIGH RESOLUTION TRANSMISSION ELECTRON MICROSCOPE

The electron wave formed at the exit face of a TEM specimen, or the transmission function, is magnified by propagating through a set of magnetic lenses. This wave signal is not only magnified but also modified by various imperfections in the magnetic lens and electron source. The alteration of the amplitude and phase of the electron wave can be so extensive that the electron wave signal at the imaging planes may be completely different from the transmission function. In order to obtain meaningful information from high resolution electron micrographs, it is absolutely essential to understand the image formation mechanism in an electron microscope. The mathematical description of the propagation of the transmission function and the modification of this wave function due to the imperfections of an electron microscope has been developed using Fourier optics (Born and Wolf 1985, Goodman 1968; Misell 1973, Frank 1973, Wade and Frank 1977, Wade 1978, Hanszen 1971, Hawkes 1978, Lenz 1971, Hawkes 1980, Ishizuka 1982). This derivation, however, is very lengthy and will not be reproduced here. We will only state important results obtained from the Fourier optics calculation and use them to describe significant aspects of the interpretation of high resolution transmission electron micrographs.

5.3.1 IMPORTANT FOURIER OPTICS THEOREMS

Theorem 1 : The wave signal formed at the back focal plane of a lens is the product of the Fourier transform (F.T.) of the wave signal at the object plane and a quadratic phase factor.

Theorem 2 : The signal formed at the imaging plane of a lens is the Fourier transform of the signal at the back focal plane. Theorems 1 and 2 imply that the signal at the imaging plane is an inverted and magnified version of the signal at the object plane.

Theorem 3 : The modification of the transmission function due to the electron optical imperfections is taken into account by multiplying the wave function at the back focal plane with a lens transfer function.

5.3.2 THE LENS TRANSFER FUNCTION

According to theorem 3 above, the alteration of the transmission function is known if we know the lens transfer function. The lens transfer function is a mathematical description of the modification of the electron wave due to the spherical aberration and defocus of the objective lens, the fluctuation of magnetic lens current and accelerating potential, and the energy distribution and finite size of the electron source. The lens transfer function is given by

$$T(\underline{k}) = E(\underline{k}) \exp \left[i\chi(\underline{k}) \right] \tag{5.24}$$

and has two components, the envelope function $E\ (\underline{k})$ and a term involving phase shift $\chi\ (\underline{k})$. $\underline{k}$ is a vector in reciprocal space. The envelope function has the form

$$E\ (\underline{k}) = P(\underline{k})\ \exp \left[-\pi^2\lambda^2\Delta^2 k^2/2 \right] \exp \left[-\pi^2 u_0 q \right], \tag{5.25}$$

where $P(\underline{k})$ is the aperture function, equal to unity inside the objective lens aperture and zero outside.

90

The expression $\exp[-\pi^2\lambda^2\Delta^2\kappa^2/2]$ describes the temporal coherency of the microscope. The focal or gaussian spread half width Δ is give by

$$\Delta = C_C \left[\left(\frac{\Delta V_a}{V_a}\right)^2 + 4\left(\frac{\Delta I}{I}\right)^2 + \left(\frac{\Delta E}{E}\right)^2 \right]^{1/2},$$

where C_C is the chromatic aberration of the microscope

$\frac{\Delta V_a}{V_a}$ is the high tension instability

$\frac{\Delta I}{I}$ is the lens current fluctuation and

$\frac{\Delta E}{E}$ is the fluctuation in electron energy due to the thermal energy distribution and electron-electron repulsive interaction (Boersch 1954, Zimmerman 1970).

The spatial coherency of the electron source is given by expression $\exp[-\pi^2 u_0^2 q]$ where

$$q = (C_s\lambda^3\kappa^3 + \delta f\lambda\kappa)^2$$

C_s is the spherical aberration constant

δf is the defocus of the objective lens

$$u_0 = \frac{\theta_c(\ln 2)^{\frac{1}{2}}}{\lambda}$$

and θ_c is the divergence half angle. The spatial coherency term arises because the incident electron wave is not a perfect plane wave.

The envelope function is a damping function. It attenuates the high spatial frequency components of the transmission function. Small features in an image are lost due to this term. The envelope function therefore determines the information limit of an electron microscope. The envelope functions of the MIT JEOL JEM 200CX and ASU JEOL JEM 4000EX are shown in Figure 5.4. We note that in deriving the envelope function, the transmission function was assumed to be a weakly scattering object (Hawkes 1980, Frank 1973). However, Tanaka and Jouffrey (1984) have demonstrated that this envelope function works satisfactorily for a strongly scattering object as well.

The phase shift term of the lens transfer function arises from the spherical aberration and defocus of the objective lens. The phase χ ($\underline{\kappa}$) in equation (5.24) is given by

$$\chi (\underline{\kappa}) = \pi \delta f \lambda \kappa^2 + 1/2 \, \pi C_s \lambda^3 \kappa^4.$$

This phase is added to the transmission function continuously in reciprocal space. The main effect of the phase shift term of the lens transfer function is to alter the contrast of an image. This contrast modification is very complex and highly sensitive to change in focus. Figures 5.5 and 5.6 show the behavior of the phase shift term as a function of reciprocal distance and focusing. The variation of image contrast due to change in focusing is illustrated in a through-thickness calculation of the NiAs (1C) structure with incident electron wave vector parallel to the [$1\bar{2}10$] direction (see Figure 5.7).

92

5.3.3 POINT RESOLUTION OF AN ELECTRON MICROSCOPE

We have shown in Section 5.2.2 that for a very thin crystal the wave function can be written as

$$\psi\ (\ \underline{r}\ ) = \exp\left[\ -i\sigma V_p\ \right].$$ (5.26)

If $\sigma V_p < 0.1$ we can expand the wave function and keep only terms of order σ. This is known as the weak phase object approximation.

$$\psi\ (\ \underline{r}\ ) = 1 - i\sigma V_p + O\ (\ \sigma^2\ ).$$ (5.27)

At the back focal plane of a lens

$$\psi\ (\ \underline{k}\ ) = \delta\ (\ \underline{k}\ ) + i\sigma\ F.T.\ (\ V_p\ ).$$ (5.28)

Note that this is the kinematical approximation !

We introduce the imperfections of the electron optics by multiplying the electron wave $\widehat{\psi}\ (\ \underline{k}\ )$ with the lens transfer function $T\ (\ \underline{k}\ )$

$$\psi\ (\ \underline{k}\ ) = (\ \delta\ (\ \underline{k}\ ) + i\sigma F.T.\ (\ V_p\ )\ )\ E\ (\ \underline{k}\ )\ \exp\ (\ i\chi\ (\ \underline{k}\ )\ )$$

$$= \delta\ (\ \underline{k}\ )\ E\ (\ \underline{k}\ )\ \exp\ (\ i\chi\ ) + i\sigma F.T.\ (\ V_p\ )\ E\ (\ \underline{k}\ )\ \cos\chi + \sigma F.T.\ (\ V_p\ )\cdot$$
$$E\ (\ \underline{k}\ )\ \sin\chi.$$

At the gaussian image plane

$$\psi \, (\, -r \,) = 1 + i\sigma V_p \, * \, F.T. \, (\, E \, (\, \underline{k} \,) \cos\chi \,) + \sigma V_p \, * \, F.T. \, (\, E \, (\, \underline{k} \,) \sin\chi \,).$$

If the potential is centrosymmetric i.e. $V_p = V_p^*$, their Fourier transforms are real, and since $\sin\chi$ and $\cos\chi$ are even, the intensity is

$$I = | \, \psi \, (\, -r \,) \, |^2 = 1 + 2\sigma V_p \, * \, F.T. \, (\, E \, (\, \underline{k} \,) \sin\chi \,) + O \, (\, \sigma^2 \,).$$

Neglecting terms of order higher than σ

$$I = 1 + 2\sigma V_p^* \, F.T. \, [\, E \, (\, \underline{k} \,) \sin\chi \,] \tag{5.29}$$

$E \, (\, \underline{k} \,) \sin\chi$ is known as the contrast transfer function. Equation (5.29) describes the intensity at the imaging plane for a weak phase object as the convolution of the projected potential and the Fourier transform of the contrast transfer function. The reciprocal of the first zero crossing of the contrast transfer function where the phase changes sign defines the "point" resolution of a microscope. It is approximately equal to $0.6 \, C_s^{1/4} \, \lambda^{3/4}$. We emphasize that the point resolution of a microscope is defined only for a weak phase object. This definition may not be applicable to a strongly scattering object. The contrast transfer functions for the MIT JEOL JEM 200CX and ASU JEOL JEM 4000EX are shown in Figure 5.8.

94

5.4 IMAGE CALCULATION METHODS

Calculations of high resolution lattice images and diffracted electron amplitudes were performed on Digital Microvax and PDP 11/750 computers using the SHRLI suite of programs (courtesy of Dr. M. A. O'Keefe) and the Arizona State University multislice programs. These programs are based on the Cowley-Moodie multislice formulation discussed in Sections 5.2 and 5.3. An outline of the SHRLI 80 suite of programs and the image program flow-chart are shown in Figures 5.9 and 5.10. Instrumental parameters used in these programs are experimentally measured values for the appropriate instrument. Further details for the SHRLI 80 and SHRLI 81E suites of programs are available in the program manual or directly from Dr. M. A. O'Keefe.

5.5 IMAGE INTERPRETATION IN HIGH-RESOLUTION TRANSMISSION ELECTRON MICROSCOPY

5.5.1 PROCEDURE FOR IMAGE ANALYSIS

The discussion in Sections 5.2 and 5.3 clearly shows that the structural information cannot be obtained reliably from a single high-resolution transmission electron micrograph. Much more stringent requirements must be met before structural information can be inferred from high resolution electron micrographs. In this study, micrographs are said to be intepretable and/or model defect structures deemed to be acceptable if

• there is general agreement between a series of through-focus or through-thickness series of experimental and calculated images and

• this comparison is carried out for at least two different orientations.

The second requirement serves as an independent verification of the structural models.

Usually, the contrast of a high-resolution electron micrograph changes continuously due to change in specimen thickness and/or focussing condition (e.g. if the specimen is not perpendicular to the incident electron wave). Image analysis is performed by carrying out a comparison between the experimental images and a matrix of through-thickness series of calculated images. An example of the comparison between experimental and calculated images is illustrated in Figure 5.11.

5.5.2 IMAGE CONTRAST REVERSAL PHENOMENON

The image interpretation of high-resolution electron micrographs can be complicated considerably due to the image contrast reversal phenomenon. With this phenomenon, high-resolution electron microscope images appearing in thin regions recur in thicker regions with the image contrast reversed. Figure 5.7 shows reversed contrast images occuring at crystal thicknesses of 3.4 Å and 75 Å for optimum (Scherzer) focus setting. This contrast reversal can be explained by investigating the behavior of the amplitudes and phases of the diffracted waves. Figure 5.12 shows the diffracted intensities along the [100] | [$1\bar{2}10$] pole that interfere and form the images shown in Figure 5.7. Figures 5.13 and 5.14 show the variation of amplitudes and phases of important diffracted beams as a function of crystal thickness. As the thickness increases, the amplitude of the diffracted waves rises and the phase difference between the transmitted and diffracted beams increases rather quickly. At 3.4 Å thickness, the phase difference between the transmitted and diffracted beams is roughly $\pi/2$. However, at 75 Å thickness the phase differences between the transmitted beam and the (012) and (011) beams, two of the three most intense beams, increases to π or to the vicinity of π; the phase difference with

(013), the other most intense beam, decreases to near zero. This change in phase difference, from π/2 to π, shifts the intensity distribution formed by the interference between the transmitted and diffracted beams by one quarter of a wavelength. This displacement of interfering amplitudes gives rise to the image contrast reversal phenomenon. We note that this contrast reversal effect can only be observed if the additional phase shifts due to the lens transfer function are the same for all important reflections. In the case of Figure 5.7, this constant phase shift condition can be achieved when the focus setting is at optimal condition.

5.5.3 Fourier Images

Another complication that often arises in the interpretation of high resolution electron microscopic images is the recurrence with focus of similar images or Fourier images. This phenomenon can be understood by the following observation.

The phase shift due to spherical aberration and defocus is given by

$$\chi \ (\kappa, \delta f \ ) = \pi \lambda \delta f \kappa^2 + 1/2 \pi C_s \lambda^3 \kappa^4$$

The phase shift at position g in reciprocal space is

$$\chi \ (g, \delta f \ ) = \pi \lambda \delta f g^2 + 1/2 \pi C_s \lambda^3 g^4$$

If $\delta f' = \delta f + \dfrac{2b_m^2}{\lambda}$,

where m is an integer and b is a lattice constant, and g is a reciprocal lattice point, such that

$$g^2 = \frac{h^2+k^2+l^2}{b^2} \qquad \text{for a cubic crystal,}$$

then

$$\chi\ (\ g,\ \delta f'\ ) = \pi\lambda\delta fg^2 + 2\pi\ (\ h^2 + k^2 + l^2\ )m + 1/2\pi C_s\lambda^3g^4$$

and since h, k, l and m are integers

$$\exp[\ i\chi\ (g,\ \delta f)\ ] = \exp[\ i\chi\ (g,\ \delta f')\ ]$$

This means that if a lattice image is formed by interfering electron waves with spatial frequency of $\frac{n}{b}$ where n is an integer, then identical lattice images of perfect crystals can be observed at focus settings differing by $m\frac{2b^2}{\lambda}$. Fourier images of cubic materials in a high symmetry orientation are commonly observed. A detailed discussion of the Fourier images of silicon lattice image can be found in Spence, O'Keefe and Kolar (1977).

For noncubic materials, Fourier images also occur. However, the image interpretation is complex. The complication arises from the fact that the phase shift χ is not the same for the important reflections. For example, in the NiAs case along the [100] | [1$\overline{2}$10] (Figure 5.12), table 5.1 lists the phase shift of four reflections at three different focus settings. The phase shift of the (010) reflection is the same for focus settings -496Å and -1526Å but different by 90° for the -766Å under-focus. The phase shifts of other reflections are all different. This means that unequal displacement of intensity will occur at different focus settings. Figure 5.15 show the calculated images of the FeS 1C structure along the [100] | [1$\overline{2}$10] direction for focus settings -496Å, -776Å and -1526Å. These images are essentially identical, however; their relative positions are not the same. The

98

intensity distribution of the image at -776Å defocus is shifted by one quarter of a wavelength along the short cell edge. The sulfur atom at -1526Å defocus is in the wrong position!. This example demonstrates that the simplistic interpretation often practiced in the literature is very likely to be incorrect for most cases.

5.5.4 Precautions in the Image Interpretation

In the discussion of image formation, we have implicitly assumed that the electrons are scattered elastically. This assumption is not valid in the thicker crystal region. Typically, inelastic and multiple scattering processes become significant when the crystal thickness is greater than 100A for materials composed of elements with atomic number less than 50. The inelastic scattering affects the image by smearing out fine features. The effect of multiple scattering is to increase the amplitude of the diffracted waves. This increased in amplitude enhances the mutual interference between diffracted beams resulting in additional fine features in an electron micrograph. The matching between experimental and calculated images becomes very complicated and often unreliable since the existing image simulation programs do not take into account the inelastic scattering process. The calculated images, thererefore, tend to have very fine features that are not observed experimentally.

The interpretation of high resolution transmission electron microscopic images also becomes complicated by the lack of precise alignment of the incident beam and the crystal projection axis with the optic axis of the objective lens. Smith et al. (1983, 1985) have shown that even slight beam tilt can have marked effect on the images of crystalline materials, causing considerable spurious detail, incorrect lattice periodicities for thicker crystals and loss of expected projection symmetry of the structure.

Finally, the contamination and/or amorphous layers formed on top and bottom of a TEM sample also cause loss and/or modification of fine details in a high resolution transmission electron micrograph. This problem can be severe in thin areas. This problem, however, can be minimized during the sample preparation process.

$$\chi = \pi\lambda\delta fk^2 + \pi/2Cs\lambda^3k^4$$

DEFOCUS (Å)

d (Å)	reflection	-496Å	-776Å	-1526Å
3.4	010	-63.59	30.66	-63.58
3.8	011	-52.46	65.50	37.37
4.8	012	-60.96	52.84	-63.30
6.11	013	34.75	90.00	-47.99

PHASE SHIFT (in degree)

TABLE 5.1. The phase shifts of the (010), (011), (012) and (013) reflections as a function of focussing.

incident wave ψ_o

↓ ↓ ↓

specimen

transmission - - - - - - - - - - - - - - - - - -
function ψ_t

lens

$\psi = \psi_t \cdot T(k)$ - - - - - - - - - - - - - back focal plane

$\psi(x/m, y/m)$ - - - - - - - - - - imaging plane
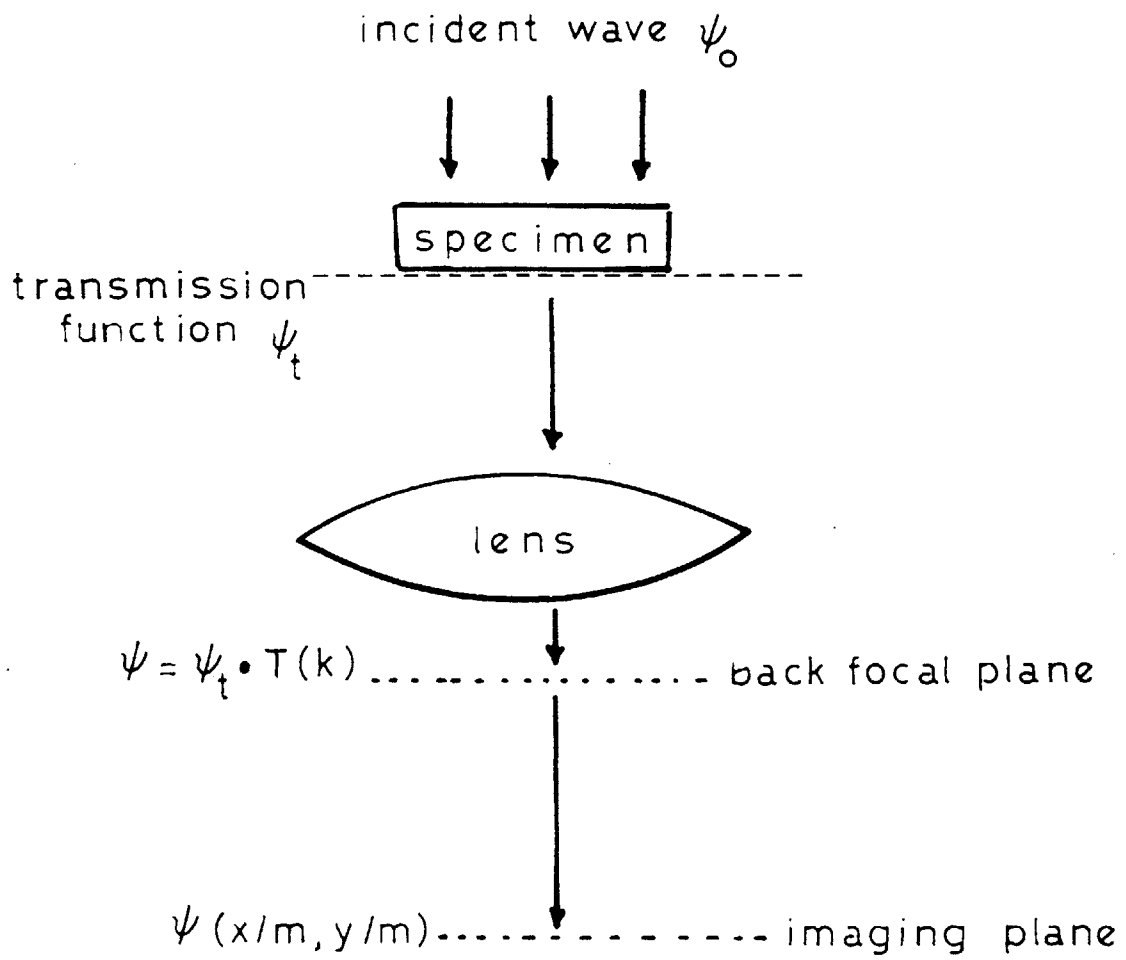
Figure 5.1. The interaction of the electron wave with the specimen and the magnetic lens of an electron microscope.
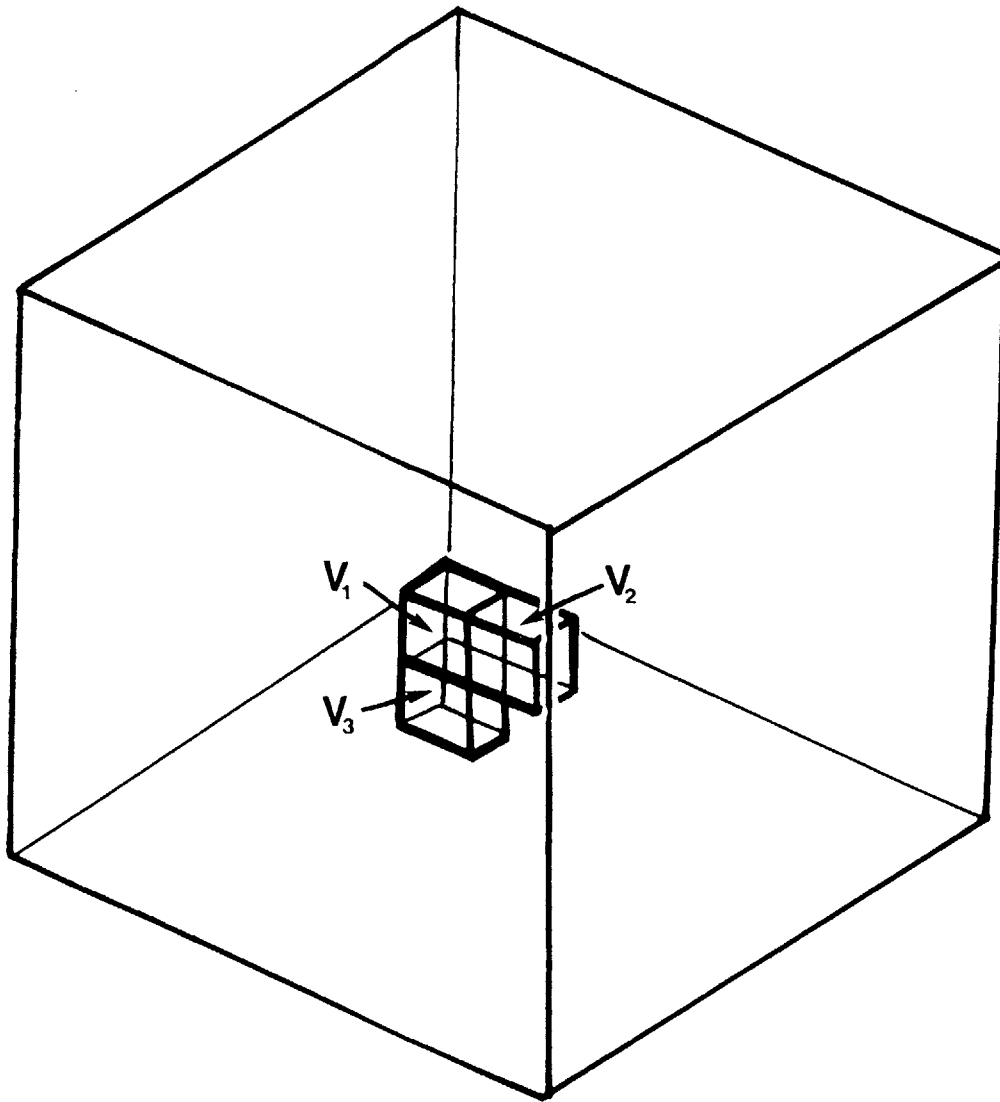
Figure 5.2. The crystal is partitioned into parallelopiped cells. The dimensions of the cell are chosen so that the potential change within the cell is small and therefore can be approximated by a constant potential.

incident
wave

Δz_i

(x_n, y_n, z_n)

R_{n+1}

(x_n', y_n', z_n')

Δz_n

θ_n

Δn

$(x_{n+1}, y_{n+1}, z_{n+1})$

$(x_{n+1}', y_{n+1}', z_{n+1}')$

Δz_{n+1} transmitted
wave
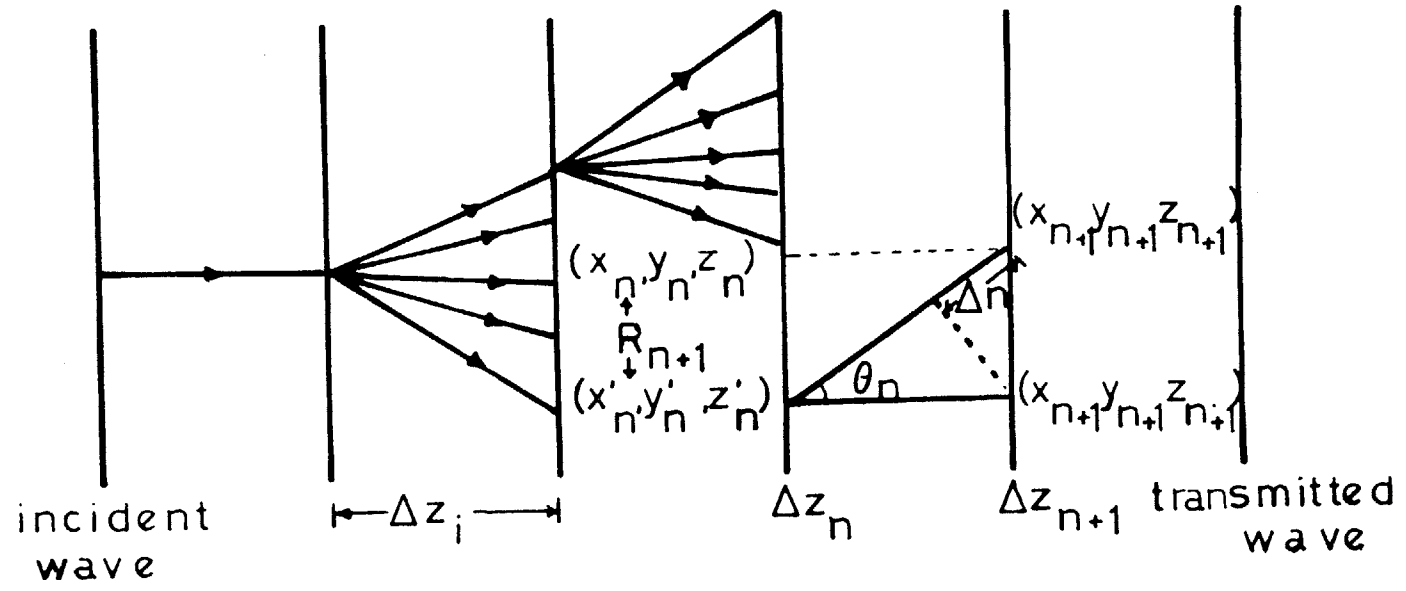
Figure 5.3. The scattering of the electron wave upon entering a new slice of material.
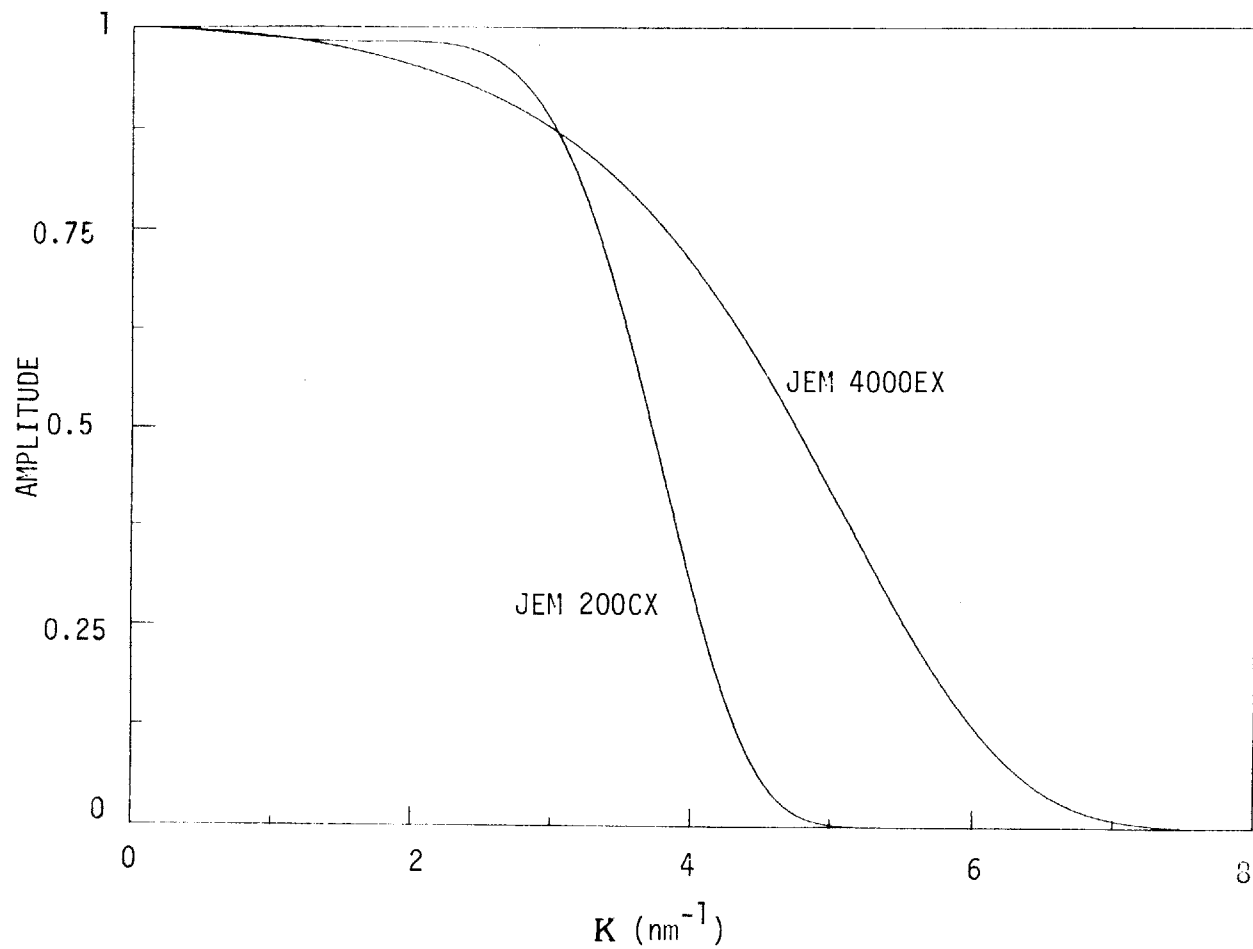
Figure 5.4. The envelope functions of the MIT JEOL JEM 200CX and ASU JEOL
JEM 4000EX.
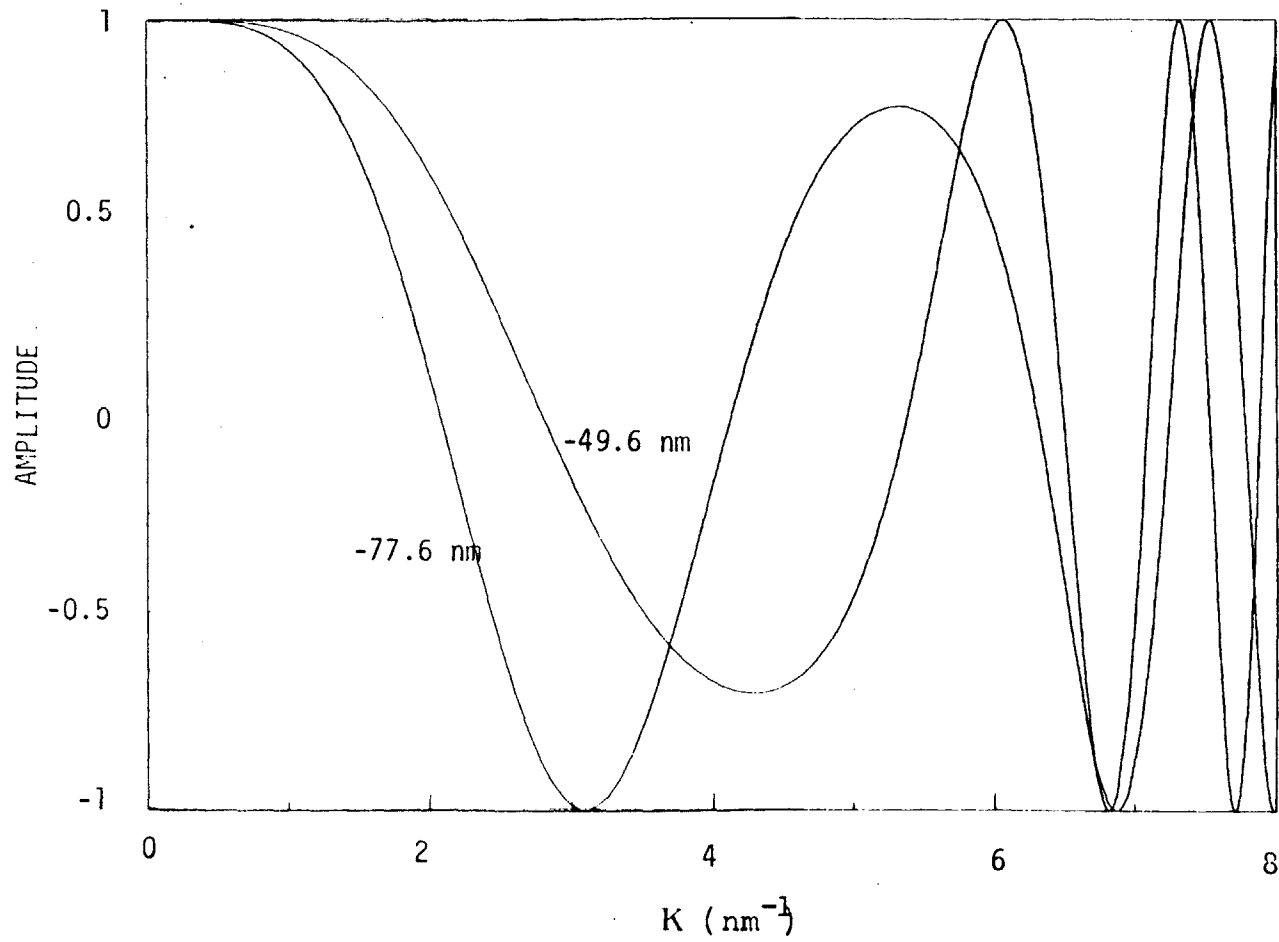
Figure 5.5. Cosχ(κ). The focus settings are -49.6 nm and -77.6 nm. The
electron optical parameters are those of the JEM 4000EX.
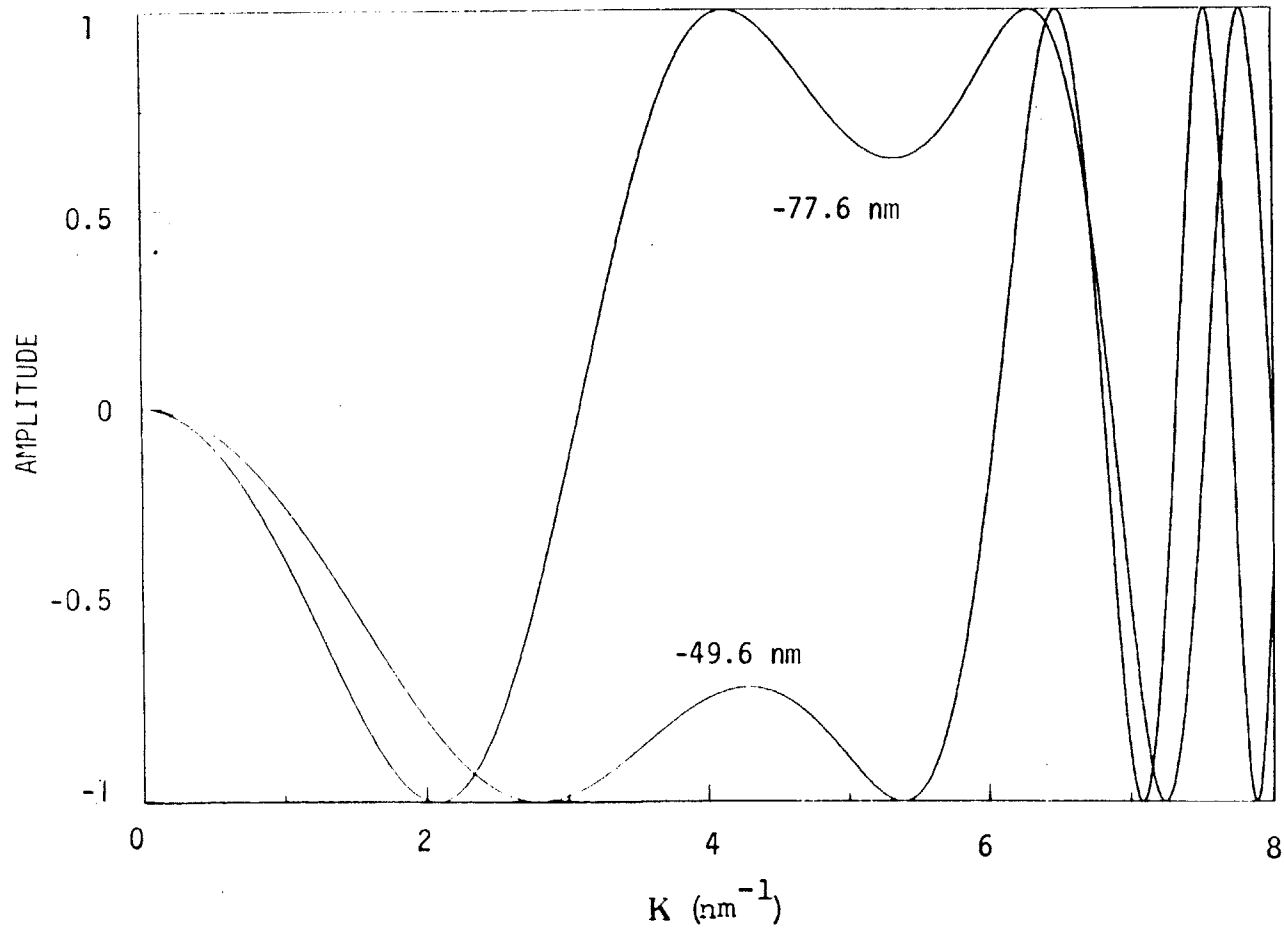
Figure 5.6. Sinχ(x). The focus settings are -49.6 nm and -77.6 nm. The electron optical parameters are those of the JEM 4000EX.

Figure 5.7. A through-focus and through-thickness image simulation of the NiAs (1C) structure with the incident wave vector parallel to the [1210] direction. The microscope parameters are those of the ASU JEM 4000EX.
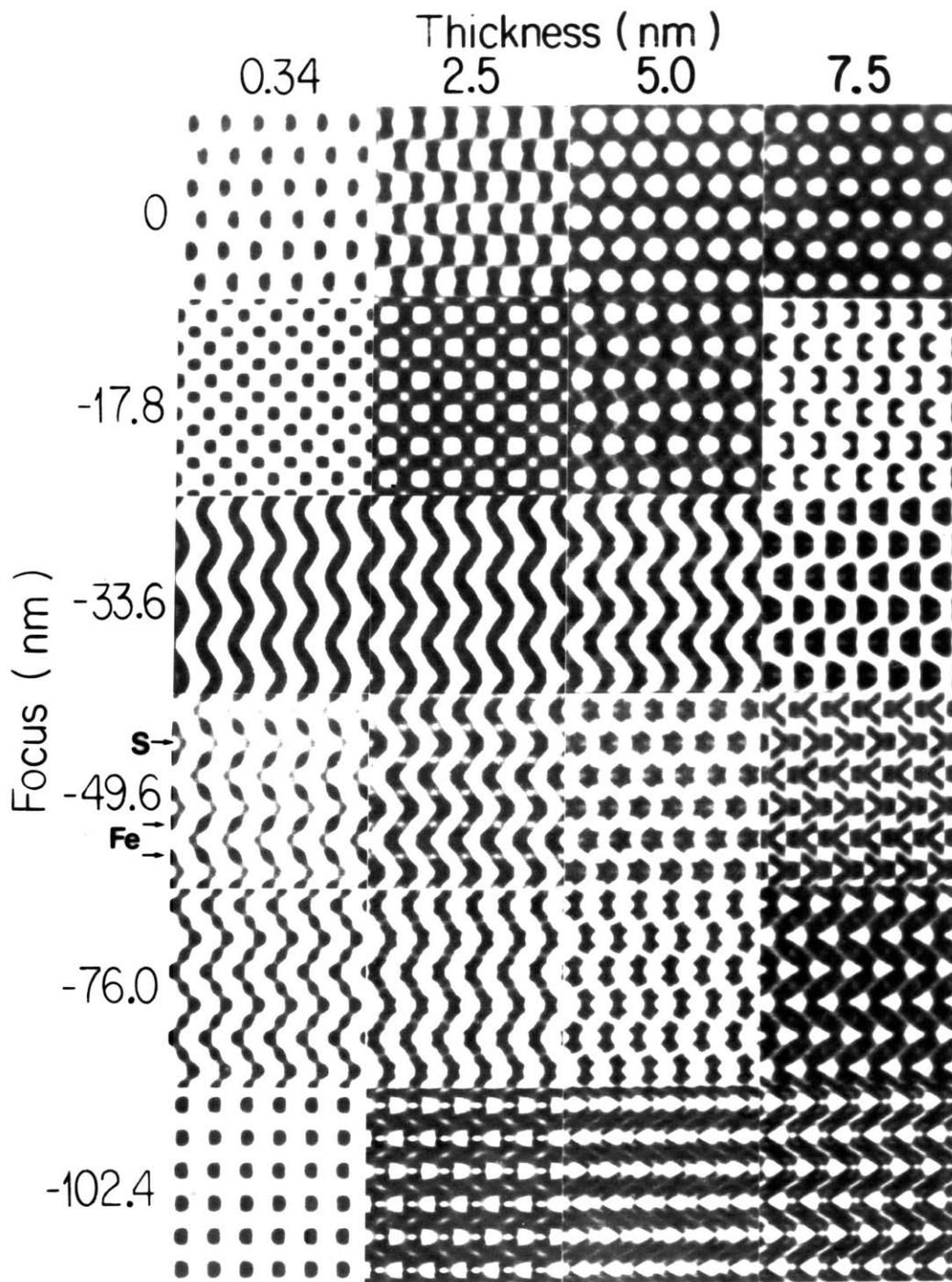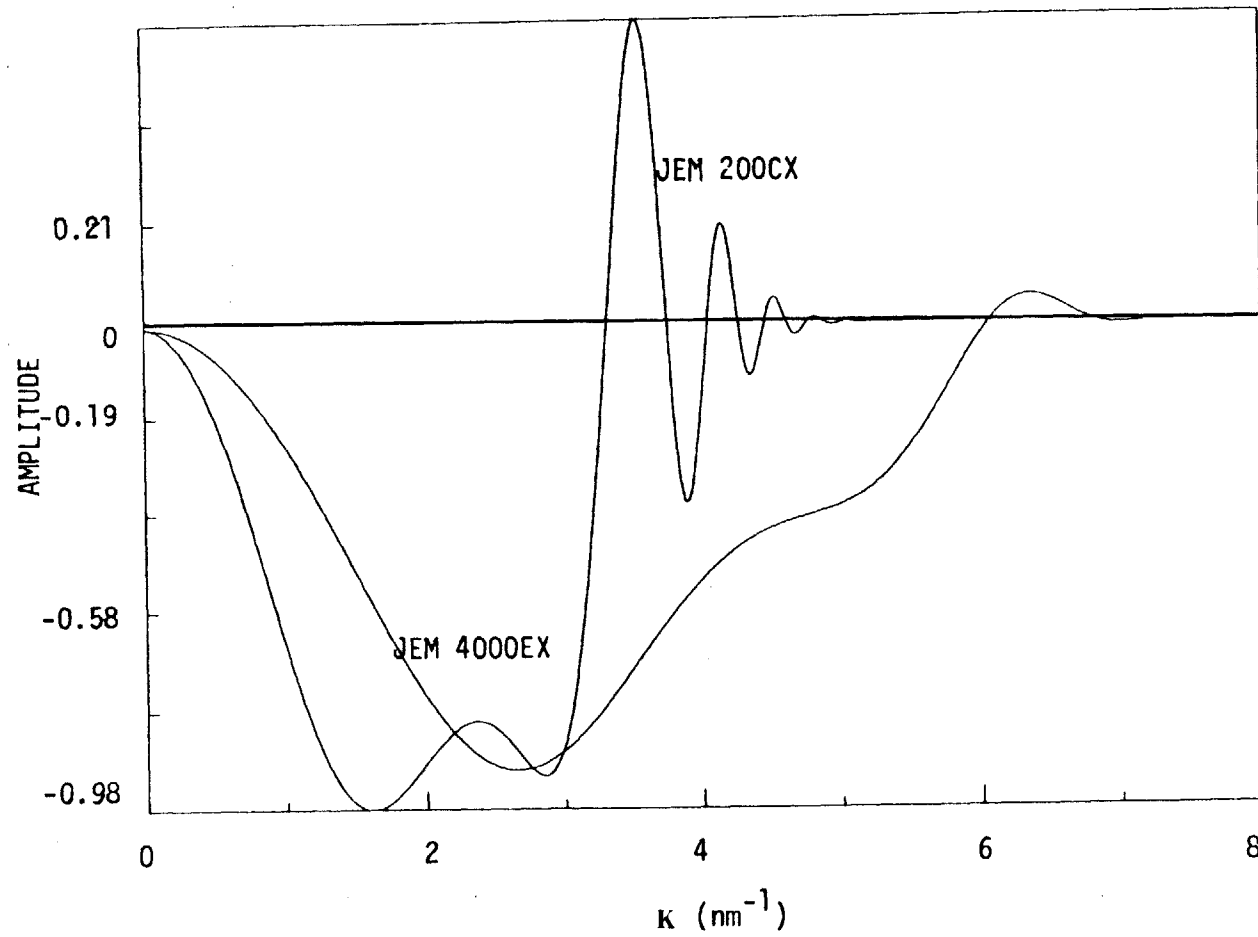
Figure 5.8. The contrast transfer functions of the MIT JEOL JEM 200CX and ASU JEOL JEM 4000EX.

STRUCTURE FACTORS

INPUT

UNIT CELL PARAMETERS $a, b, c, \alpha, \beta, \gamma$
ATOMIC POSITIONS x_t, y_t
ELECTRON SCATTERING FACTOR   Tables for All Atom Species

CALCULATE

SCALED STRUCTURE FACTORS, $V(h,k)$, OUT TO 2Å^{-1} IN THE REQUIRED ZONE

$$V(h,k) = \frac{1}{V_c} \sum_t f_t^B(s) \cdot \exp\{2\pi i(hx_t/a + ky_t/b)\}$$

WHERE: V_c = unit cell volume
f_t^B = electron scattering factor for the tth atom
$s = \sin\theta/\lambda$

SINGLE SLICE

INPUT

STRUCTURE FACTORS $V(h,k)$
MICROSCOPE ACCELERATING VOLTAGE W
SLICE THICKNESS Δz

CALCULATE

1. PROJECTED POTENTIAL TO ½ Å RESOLUTION $\phi(x,y) = \mathcal{F}\{V(h,k)\}\Delta z$
2. PHASE GRATING TO ½ Å RESOLUTION $q_1(x,y) = \exp\{i\sigma\phi(x,y)\}$
3. SINGLE SLICE EXIT WAVE AMPLITUDE $Q_1(h,k) = \mathcal{F}^{-1}\{q_1(x,y)\}$

WHERE: $\mathcal{F}$ = Fourier transform
σ = interaction parameter

$$\frac{2\pi}{\lambda W} \frac{1}{1 + \sqrt{1 - \beta^2}}$$

λ = electron wavelength
β = v/c
c = velocity of light

MULTISLICE

INPUT

SINGLE SLICE WAVE AMPLITUDE $Q_1(h,k)$
SLICE THICKNESS Δz
ELECTRON WAVELENGTH λ

CALCULATE

1. IN-CRYSTAL PROPAGATOR $P(h,k) = \exp\{i\pi\lambda\Delta z u^2\}$
2. TWO-SLICE EXIT AMPLITUDE $Q_2(h,k) = \{Q_1(h,k) \cdot P(h,k)\} * Q_1(h,k)$
3. THREE-SLICE EXIT AMPLITUDE $Q_3(h,k) = \{Q_2(h,k) \cdot P(h,k)\} * Q_1(h,k)$

⋮

n. n-SLICE EXIT AMPLITUDE $Q_n(h,k) = \{Q_{n-1}(h,k) \cdot P(h,k)\} * Q_1(h,k)$

WHERE: * represents the convolution operation
$u = 2\sin\theta/\lambda$

THE IMAGE

INPUT

ELECTRON WAVE AMPLITUDE AT CRYSTAL EXIT SURFACE $Q_n(h,k)$
OBJECTIVE APERTURE RADIUS (Å^{-1}) R
OBJECTIVE LENS SPHERICAL ABERRATION COEFFICIENT (mm) C_s
OBJECTIVE LENS DEFOCUS (Å) ϵ

CALCULATE

1. LENS TRANSFER FUNCTION FOR BEAMS WITH $u \leq R$ $\chi = \pi i\lambda\epsilon u^2 + \frac{1}{2}\pi i\lambda^3 C_s u^4$
2. PROPAGATE WAVE AMPLITUDE FROM EXIT SURFACE $\psi(h,k) = Q_n(h,k) \cdot \exp\{i\chi\}$
3. IMAGE AMPLITUDE $\psi(x,y) = \mathcal{F}\{\psi(h,k)\}$
4. IMAGE INTENSITY $I(x,y) = \psi^*(x,y) \cdot \psi(x,y)$

Figure 5.9. An outline of the computational procedure used in the SHKLI 80 suite of image simulation programs. (Courtesy of Dr. M.A. O'Keefe).

111
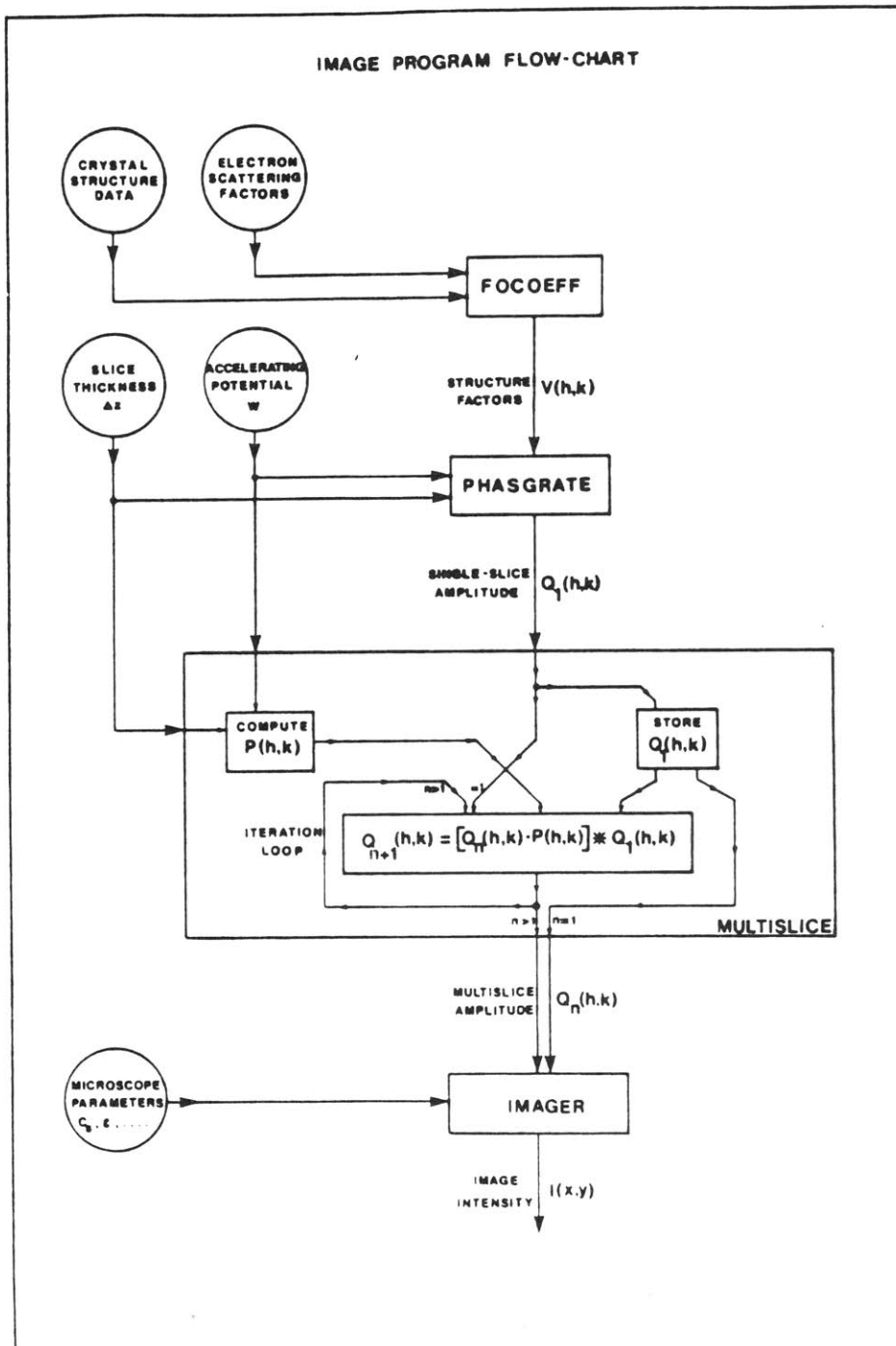
Figure 5.10. Image program flow chart for the SHRLI 80 suite of programs. (Courtesy of Dr. M.A. O'Keefe).

Figure 5.11. Computed (right) and experimental (left) lattice images of troilite matched for various focus settings. The computed images are based on the structure reported by King and Prewitt (1982). The focus values for the experimental and theoretical images in nm are (a) -49.6, (b) -62.0, (c) -76.0.
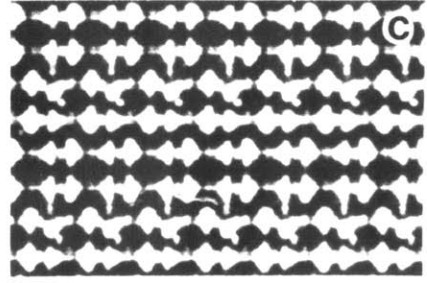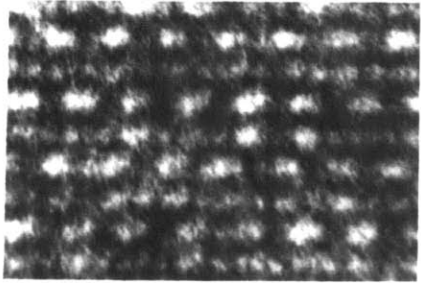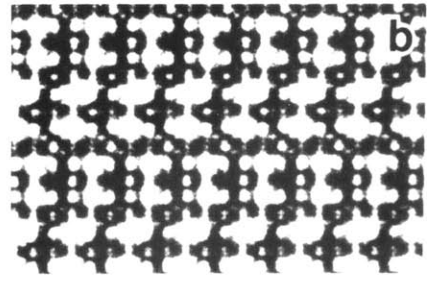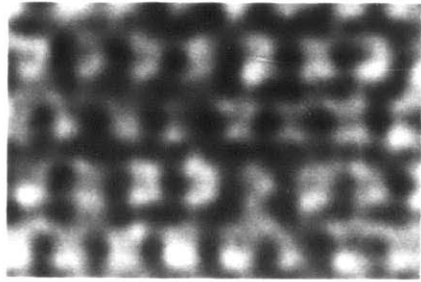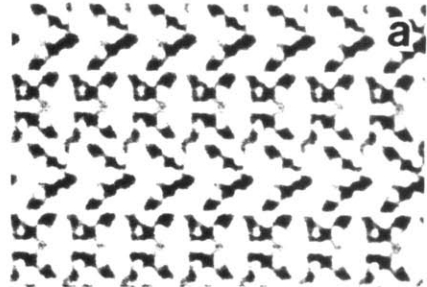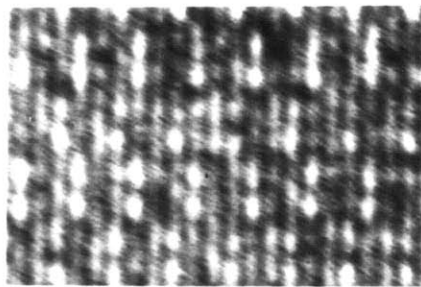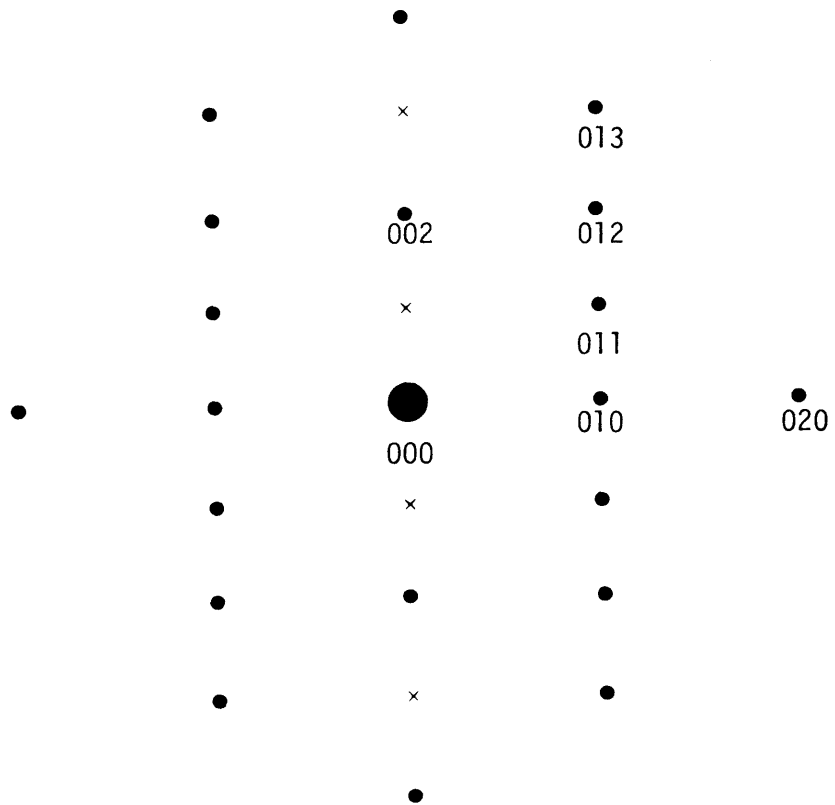
Figure 5.12. The diffraction pattern of the NiAs (1C) structure along the [100]|[1210] direction.
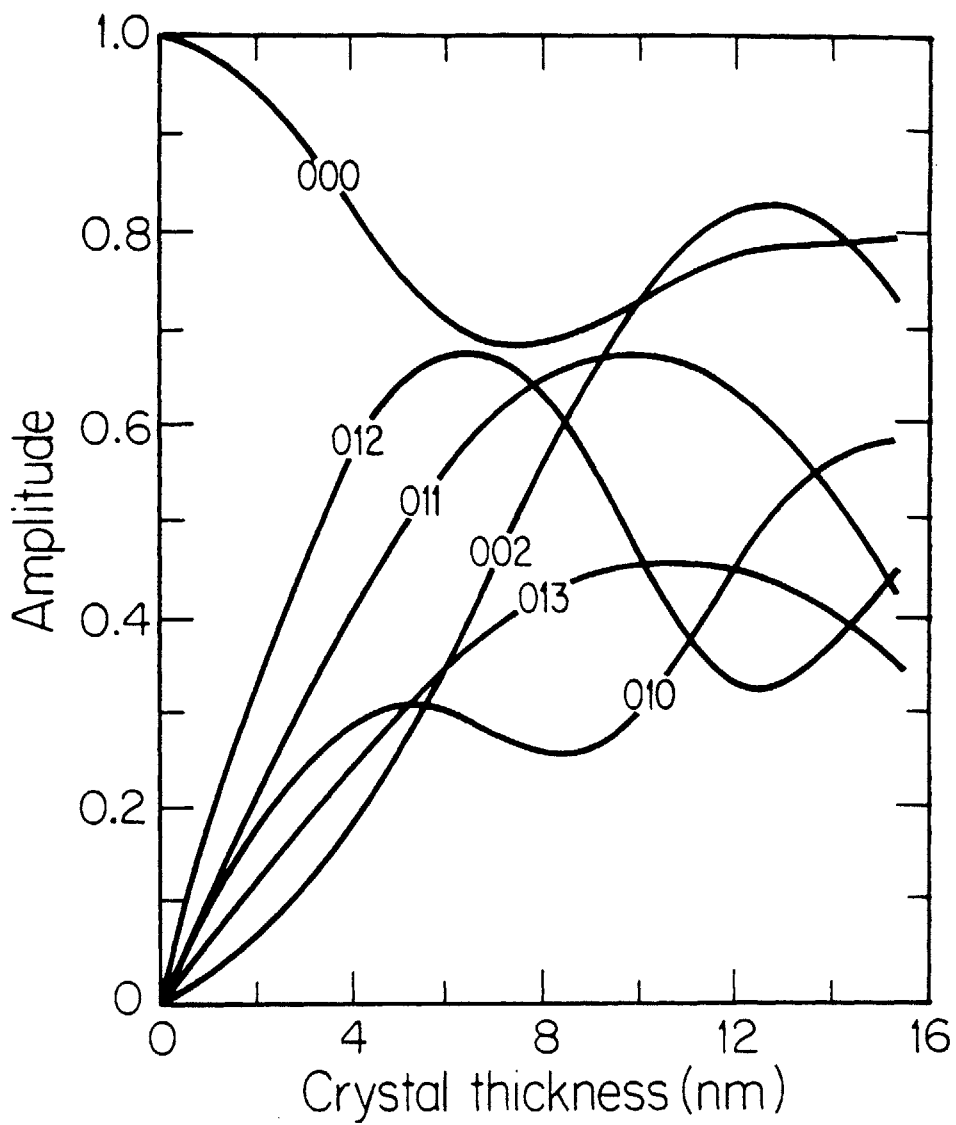
Figure 5.13. The variation of amplitudes of important diffracted beams as a function of crystal thickness. The diffracted beams intensities are plotted with an amplification factor of 4 to bring out the variation in intensity.
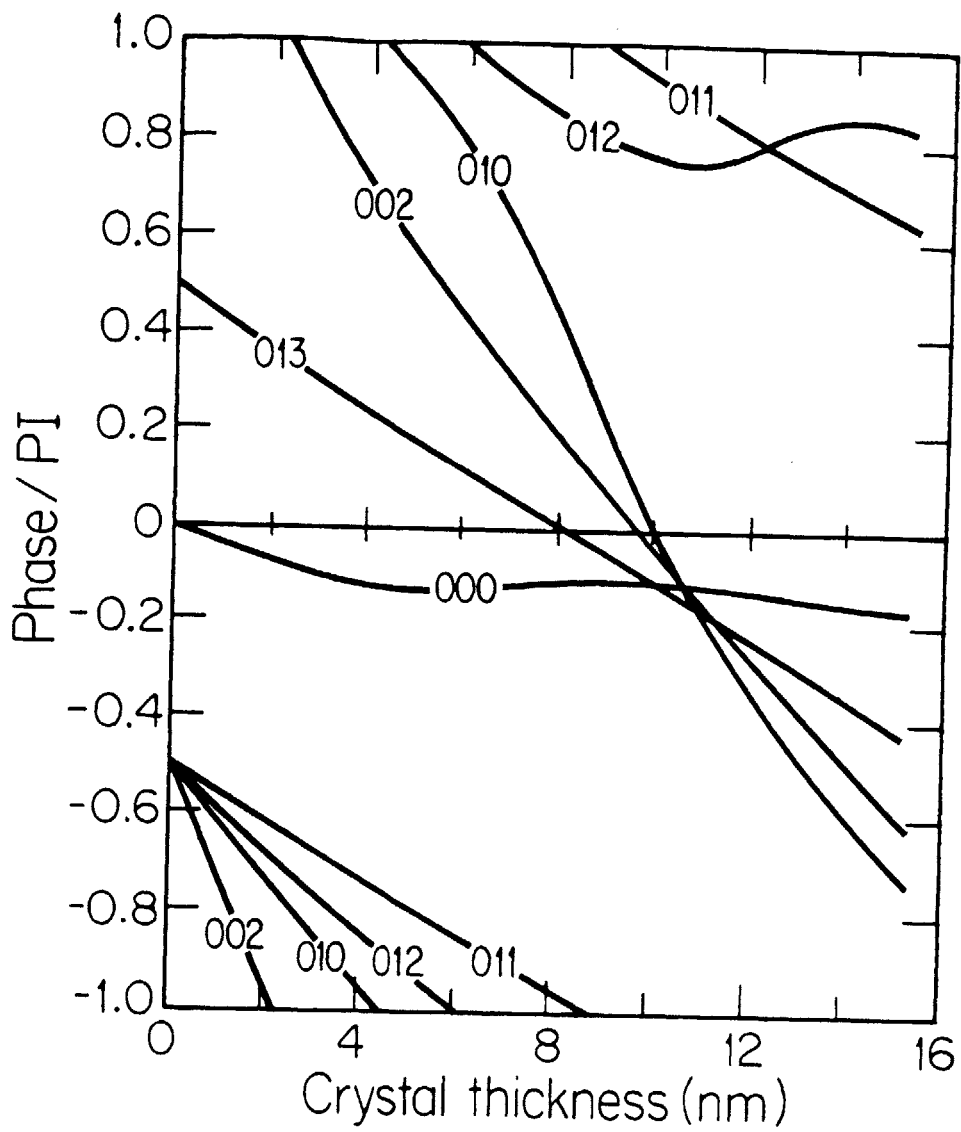
Figure 5.14. The variation of phases of important diffracted beams as a function of crystal thickness.

Figure 5.15. Image simulation of the FeS 1C structure along the [100]|[1210] direction for focus setting -496A , -776A   and -1526A.
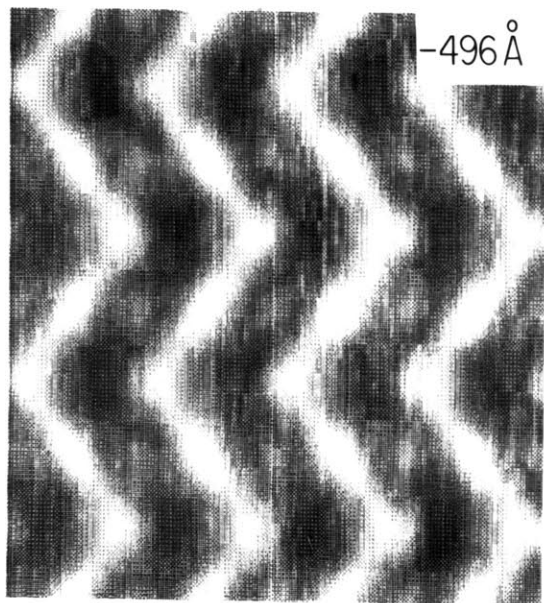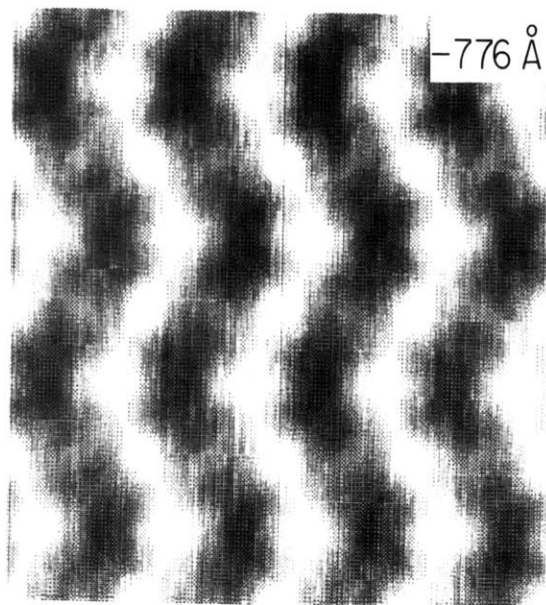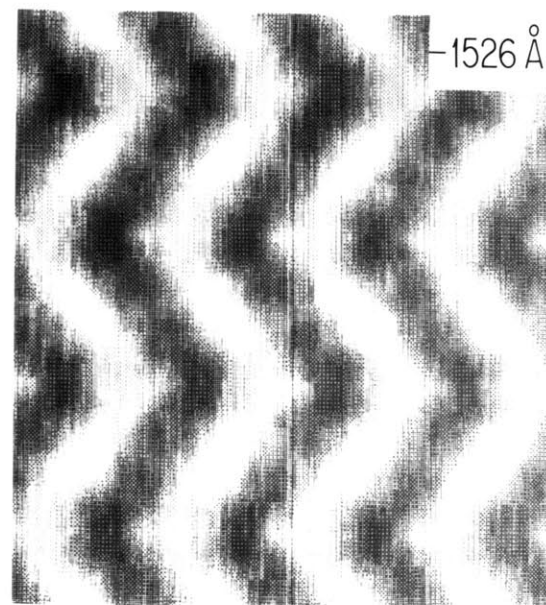
(a) (b) (c)

References

Boersch, H.. Z. Physik 139, 115 (1954).

Berry, M. V.. J. Phys. C. 4, 697-722 (1971).

Bethe, H. A.. Ann. Phys. 87, 55-129 (1928).

Born, M. and Wolf, E.. Principle of Optics, 5th edn. Pergamon, New York (1975).

Cowley, J. M.. Diffraction Physics, Elsevier Science Publishers, Netherlands (1979).

Cowley, J. M. and Moodie, A. F.. Acta Cryst. 10, 609-619 (1957).

Cowley, J. M. and Moodie, A. F.. Acta Cryst. 12, 353-359 (1959).

Cowley, J. M. and Moodie, A. F.. Acta Cryst. 12, 360-367 (1959).

Feynman, R. P. and Hibbs, A. R.. Quantum Mechanics and Path Integrals, McGraw-Hill Book Co. NY (1965).

Frank, J.. Optik 38, 519-536 (1973).

Fujiwara, K.. J. Phys. Soc. Japan 16, 2226-22238 (1961).

Goodman, J. W.. Introduction to Fourier Optics, McGraw-Hill, New York (1968).

Goodman, P. and Moodie, A. F., Acta Cryst. A30, 280-289 (1974).

Gratias, D. and Portier, R.. Acta Cryst. A39, 576-584 (1983).

Hanszen, K. J.. Adv. Opt. Electron Microsc. 4, 1-82 (1971).

Howie, A. and Whelan, M. J.. Proc. Roy. Soc. A263, 217-237 (1961).

Hawkes, P. W.. Adv. Opt. Electron Microsc. 7, 101-173 (1978).

Hawkes, P. W.. In Imaging Processes and Coherence in Physics (M. Schlenker et al. eds.) pp 415-422. Springer-Verlag, New York (1980).

Humphreys, C. J.. Rept. Progr. Phys. 42, 1825-1887 (1979).

Ishizuka, K. and Uyeda, N.. Acta Cryst. A33, 740-749 (1977).

Ishizuka, K.. Ultramicroscopy 5, 55-65 (1980).

Jap, B. K. and Glaeser, R. M., Acta Cryst. A34, 94-102 (1978).

Lenz, F. A.. In Electron Microscopy in Materials Science (U. Valdre, ed.) pp. 540-569. Acudemic Pcess. New York and London (1971).

Misell, D. L.. Adv. Electron. Electron Phys. 32, 63-191 (1973).

O'Keefe, M. A., Simulated High Resolution Lattice Image (unpublished program) .

Rez, P.. Acta Cryst. A34, 48 (1978).

Sakurai, J. J.. Modern Quantum Mechanics, Benjamin/Cummings Publishing Company Inc., Menlo Park, California (1985).

Self, P. G. et al.. Ultramicroscopy 11, 35-52 (1983).

Shankar, R.. Principle of Quantum Mechanics, Plenum Press, New York (1980).

Smith, D.J. et al., Ultramicroscopy 11 263-282 (1983).

Smith, D.J., Bursill, L.A., Wood, G.J. . Ultramicroscopy 16, 19-32 (1985).

Spence, J. C. H., O'Keefe, M. A. and Kolar, H.. Optik 49, 307-323 (1977).

Spence, J. C. H.. Experimental High Resolution Electron Microscopy, Clarendon Press, Oxford (1981).

Sturkey, L.. Proc. Phys. Soc. 80, 321-354 (1962).

Tanaka, M. and Jouffrey, B.. Acta Cryst. A40, 143-151 (1984).

Van Dyck, D.. Phys. Stat. Sol. (b) 72, 321-336 (1975).

Wade, R. H. and Frank, J.. Optik 49, 81-92 (1977).

Wade, R. H.. Ultramicroscopy 3, 329-334 (1978).

Whelan, M. J.. J. Phys. Soc. Japan 17, Suppl, B II , 122- (1962).

Zimmerman, B.. Adv. Electron. Electron Phys. 29, 257-311 (1970).

CHAPTER 6

PHASE RELATIONS, PHASE TRANSFORMATION AND STRUCTURES OF $Fe_{1-x}S$, $0 < x < 0.08$

The following two chapters are devoted to the presentation and discussion of results of this investigation. This chapter presents the experimental results of the investigation of the phase relations, phase separation mechanism and the structures of $Fe_{1-x}S$ compounds with composition ranging from FeS to $Fe_{0.92}S$ ($Fe_{1-x}S$, $0 < x < 0.08$). The phase relation, structures and defect structures of $Fe_{1-x}S$ in the composition range from $Fe_{0.92}S$ to $Fe_{0.875}S$ or Fe_7S_8 ($Fe_{1-x}S$, $0.08 < x < 0.125$) will be reported in the next chapter.

6.1 INTRODUCTION

The phase relations, phase transformation mechanisms and structures of $Fe_{1-x}S$ in the composition range from FeS to $Fe_{0.92}S$ are the major focus of this chapter. The phase relations and microstructures of the "as grown" synthetic pyrrhotite in this composition range will be addressed in the following two sections. A temperature versus composition phase diagram is constructed from results of the room temperature and *in situ* heating studies and from the powder and precession x-ray diffraction data. Because the equilibrium phase diagram of $Fe_{1-x}S$ ($0 < x < 0.08$) is determined mainly from the *in situ* heating experiments, the task of ensuring the system has achieved thermal equilibrium is critically important. The time scale required for a system to reach equilibrium can be determined if the kinetics and the phase transformation mechanism are known. Section 6.4 will be devoted exclusively to the presentation and discussion of the phase transformation

122

that occurs in this system. From these transformation studies, an iron diffusion coefficient at 366 K was obtained. The structural investigation of troilite FeS and $Fe_{0.92}S$ at room temperature by high resolution transmission electron microscopy is reported in Section 6.5. This chapter ends with a summary of important results and a discussion of results reported in the literature.

6.2 COEXISTENCE OF TROILITE FeS AND $Fe_{0.92}S$ AT ROOM TEMPERATURE

In this section, we present experimental evidence showing that compositions $Fe_{1-x}S$ compounds ($0 < x < 0.08$) are unstable at room temperature. They decompose into two compounds, FeS and $Fe_{0.92}S$. The stoichiometric FeS compound is identified as troilite. It is embedded in the $Fe_{0.92}S$ matrix in a rodlike structure.

6.2.1 EXPERIMENTAL DETAILS

Specimens used for electron microscopy studies were prepared from the "as grown" synthetic $Fe_{1-x}S$ ($0 < x < 0.08$) crystals. The orientations of the TEM samples were chosen in such a way that either the $<1\bar{2}10>$ and $<0\bar{1}10>$ zone axes or the $<0001>$, $<0\bar{1}12>$ and $<1\bar{2}13>$ zone axes can be accessed by the JEM 200CX STH10 double tilting holder. All TEM specimens were ion thinned to electron transparency with the specimen holder cooled to 123 K.

In order to obtain accurate lattice parameters, a precession x-ray diffraction study was carried out on one sample (FeS MIT*1). This sample came from a thin area of the extensively studied FeSMIT*1 TEM specimen . The composition of the this sample was assumed to be the same as that of the $Fe_{1-x}S$ powder obtained from the same slab that was used to prepare the FeSMIT*1 specimen. The

composition of the $Fe_{1-x}S$ powder was determined using the Arnold-Reichen-d_{102} technique.

6.2.2 RESULTS

Experimental evidence showing that $Fe_{1-x}S$ ($0 < x < 0.08$) decomposes to two compounds, FeS and $Fe_{0.92}S$, comes from x-ray diffraction and electron microscope studies. Figure 6.1, is a powder x-ray diffraction pattern of $Fe_{1-x}S$ showing two distinct peaks at $2\theta_B= 43.2 \pm 0.1^0$ and $2\theta_B= 43.7 \pm 0.1^0$. These peaks correspond to lattice spacings of 2.093 ± 0.004 Å and 2.072 ± 0.004 Å respectively. They are the d_{102} reflections of iron sulfide compounds of composition FeS (50 $\pm$ 0.25 at % Fe) and $Fe_{0.92}S$ (47.85 $\pm$ 0.25 at % Fe), according to the Arnold-Reichen d_{102}-versus-composition curve.

Electron and precession x-ray diffraction patterns of the [0001], [1$\bar{2}$10] and [0$\bar{1}$10] poles (Figures 6.2 and 6.3) also indicate the presence of two different phases. A slight difference in lattice parameters can clearly be observed from the high order reflections along the $\underline{c}^*$-axis (see horizontal arrows in Figures 6.2 b,c and 6.3 b,c). The locations and spacings of the superstructures, labelled by the Miller indices in Figures 6.2 and 6.3, are identical to those of the stoichiometric troilite FeS "2C" structure. Note that except for the kinematically forbidden but dynamically allowed reflections (i.e. 0$\bar{2}$2 reflection in Figure 6.3c) the precession x-ray and the electron diffraction patterns are identical. The lattice parameters (a=b= 5.975(5)Å c= 11.78(2)Å) measured from the precession x-ray diffraction method are in good agreement with those reported from the single crystal study of troilite (King and Prewitt 1982; Evans 1970). The stoichiometric FeS is therefore troilite and has a 2C structure. The structure and stability of $Fe_{0.92}S$ will be explored fully in Sections 6.3 and 6.5.

The coexistence of troilite and $Fe_{0.92}S$ can also be observed directly by transmission electron microscopy. Figures 6.4a,b are dark field images formed by the superstructure reflections of troilite phase. Figure 6.4a shows a composite microstructure of two compounds, troilite FeS and $Fe_{0.92}S$. They coexist in a lamellar type morphology. The long edge of the troilite phase is normal to the [0001] direction and parallel to the $[1\bar{2}10]$ direction. The superstructure dark field image shown in Figure 6.4b also shows a lamellar structure. The long edge of the troilite phase is parallel to the $[1\bar{2}10]$ direction and perpendicular to the $[\bar{1}010]$ direction. Since the orientations of the microstructures shown in Figures 6.4a.b are orthogonal to each other, the existence of the lamellar morphology in both Figures 6.4a,b implies that the troilite phase is embedded in the $Fe_{0.92}S$ matrix with a rodlike structure. The nature and origin of this rod like morphology are reported in Section 6.4.

6.3 PHASE RELATIONS IN $Fe_{1-x}S$. $0 < x < 0.08$

The phase relations of $Fe_{1-x}S$ crystals with compositions ranging from FeS to $Fe_{0.92}S$ have been investigated by a series of *in situ* heating experiments. The experimental results obtained from these experiments demonstrate unambiguously that the previous "generally accepted" phase diagram is incorrect. A new temperature versus composition phase diagram has been constructed from results of this and previous sections.

6.3.1 EXPERIMENTAL DETAILS

In situ heating experiments were carried out using a JEOL JEM EM-SHTH double tilt heating holder and a Gatan single tilt heating holder. The TEM samples used in

these experiments are those showing the composite rodlike microstructure of FeS and $Fe_{0.92}S$. The average composition at any region can be deduced from the volume ratio of the two compounds. Experimentally, one can find areas where there is no overlap between the FeS and $Fe_{0.92}S$ regions through the thickness of a TEM sample. This is possible because the TEM sample thickness near the edge of a perforation is thinner than an FeS rod (the thickness of the areas studied varies from about 100 Å to 600 Å). The volume ratio is then equal to the area ratio which can be measured by an image analyzer . We note that the accuracy of area ratio measurement is limited by the validity of the assumptions that FeS rods have square cross-section and that there is no overlap between the FeS and $Fe_{1-x}S$ compounds along the thickness of the TEM sample. These assumptions are met experimentally in the beginning of the heating experiment. They become less valid when the temperature approaches the transformation temperature T_α since overlapping between the FeS and $Fe_{1-x}S$ phases inevitably occurs as the FeS rods continue to shrink. The measurement error of the area ratio, nevertheless, is very small because the TEM sample thickness is much smaller than the lateral dimensions of the measured area. The uncertainty in the area ratio measurement is also insignificant compared to the uncertainties in temperature and composition.

A great deal of effort has been made to ensure that the experimental system reaches thermal equilibrium. When the sample is raised to a new temperature, the diffraction pattern and the image of the sample are recorded only after the temperature has been held fixed for a predetermined time interval calculated from the kinetic data. The diffusion length $x = \sqrt{Dt}$ in this time span is always greater than half of the separation distance between the FeS rods. Discussion of the iron diffusion kinetics is given in Sections 2.9 and 6.4.4.3. In the heating experiments that were carried out to determine the solvus between $Fe_{1-x}S$ and a mixture of FeS and $Fe_{1-x}S$ phases, one other verification for thermal equilibrium has also been used.

126

The area ratio is monitored periodically during the annealing. The system is assumed to be equilibrium if the area ratio reaches a steady state value.

6.3.2 RESULTS

Figure 6.5 shows the evolution of the composite structure of FeS and $Fe_{1-x}S$ as a function of temperature. These images are formed using the troilite superstructure reflections. At room temperature, the composition of the iron poor $Fe_{1-x}S$ is $Fe_{0.92}S$ (47.85 at % Fe). The average composition of the two compounds is $Fe_{0.97}S$ (49.14 at % Fe). As the temperature increases, the area fraction of the troilite phase (Figures 6.5 a-e) decreases continuously. The troilite phase disappears at 390 K. Correspondingly, the area fraction of the iron-poor $Fe_{1-x}S$ continues to increase as the temperature rises. The composition of the iron poor $Fe_{1-x}S$ increases from $Fe_{0.92}S$ (47.85 at % Fe) at 298 K to $Fe_{0.97}S$ (49.14 at % Fe) at 390 K.

The results shown in Figure 6.5 established a solvus separating $Fe_{1-x}S$ (0 < x < 0.08) into a two-phase mixture of troilite FeS and an iron-deficient $Fe_{1-x}S$ composition. The position of this solvus has been determined from the area ratios of FeS and $Fe_{1-x}S$ (hence the weight fractions of FeS and $Fe_{1-x}S$) and the application of the lever rule

$$C_{FeS} f_{FeS} + C_{Fe_{1-x}S} f_{Fe_{1-x}S} = C_i$$

where C_i is the initial average composition and f_{FeS} and $f_{Fe_{1-x}S}$ are the weight fractions of FeS and $Fe_{1-x}S$ respectively. The phase diagram in Figure 6.6 shows this solvus tracing from FeS at 433 K to $Fe_{0.92}S$ at 298 K. Data and results used in the construction of this solvus are listed in Table 6.1. The thermal histories of these data are also delineated in this table. We note that the temperature obtained

by extrapolation of the solvus to the composition FeS (50 at % Fe) agrees with that reported by Sugaki and Shima (1977). The temperature at any composition along this solvus is called T_α.

The structural transformation between FeS and $Fe_{1-x}S$ has also been studied by *in situ* heating electron diffraction. Figure 6.7 shows the selected area electron diffraction patterns of $Fe_{1-x}S$ or a mixture of $Fe_{1-x}S$ and FeS at seven different temperatures. The incident electron beam is parallel to the [$0\bar{1}10$] direction. These diffraction patterns are formed from the same area shown in Figure 6.5. Figures 6.7 a,b,c,d are the diffraction patterns of areas shown in Figures 6.5 a,b,c,d, respectively. In these diffraction patterns, the superstructure reflections of troilite FeS and $Fe_{1-x}S$ are marked by arrows and labelled 2C and 1C respectively.

The superstructure reflections of the troilite FeS (2C) phase, as expected, cease to exist at temperatures above 390 K (Figure 6.7d). The superstructure reflections of the $Fe_{1-x}S$ phase, however, continue to exist above 390 K (Figure 6.7d). They do not completely transform to the NiAs (1C) structure until the temperature reaches 483 K (Figure 6.7e). The fact that the superstructure reflections of the $Fe_{1-x}S$ phase persist up to 483 K implies that the structure of $Fe_{1-x}S$ in the temperature range of 298 K to 483 K is not the NiAs structure. This result contradicts that reported by Morimoto and Nakazawa (1978) and Sugaki and Shima (1977) (see figure 2.5). Figure 6.8 shows the diffraction patterns of the two-phase mixture of FeS and $Fe_{1-x}S$ or single phase $Fe_{1-x}S$. The average composition of the area that scattered the electron wave is $Fe_{0.98}S$. The incident electron beam is parallel to the [$1\bar{2}10$] direction. In this orientation, there are no troilite superstructure reflections. The superstructure reflections of the $Fe_{1-x}S$ phase are marked by the arrows. Again, the superstructure reflections of $Fe_{1-x}S$ persist up to 473 K. Notice that the slight difference in lattice parameters between FeS and

$Fe_{1-x}S$ (marked by horizontal arrows in Figure 6.8a) at low temperature disappears at temperatures above the solvus line (Figures 6.8a,c).

The positions of the superstructure reflections of the $Fe_{1-x}S$ phase change as a function of composition and temperature. At temperature below the solvus, the c dimension of the superstructure increases from 4.91C at 298 K ($Fe_{0.92}S$) to 5.45C at 390 K ($Fe_{0.98}S$) (Figures 6.8a,b). At temperatures above the solvus and at composition $Fe_{0.98}S$ (49.4 at % Fe), the c dimension of the superstructure of $Fe_{1-x}S$ decreases from 5.45C at 390 K to 4.10C at 458 K. Henceforth, the $Fe_{1-x}S$ phase(s) with the incommensurate superstructure reflections along the c* direction is (are) called the IC phase(s). IC is the acronym for Incommensuration along the C-axis. Here, the precise application of our definition of a phase leads to the conclusion that there are a very large number of IC phases in the phase field demarcated by the two solvuses (see Figure 6.6). We, however, shall not pursue this issue further.

When $Fe_{0.97}S$ is heated above 460 K, the superstructure reflection intensity decreases steadily and disappears at 483 K (see Figure 6.7e and 6.8d for composition $Fe_{0.98}S$). The IC phase completely transforms to the 1C phase at 483 K. Upon cooling, the IC superstructure reflections reappear at 418 K (Figure 6.8C). The facts that the superstructure reflection intensity decreases steadily as the temperature approaches 483 K and that there is a temperature hysterisis upon cooling suggest that the transformation between IC and 1C is first order.

In this section, we have presented experimental evidence indicating the existence of two solvus lines in the composition range of FeS and $Fe_{0.92}S$. The first solvus separates the $Fe_{1-x}S$ (IC) phase and a two-phase mixture of FeS (2C) and $Fe_{1-x}S$ (IC). The second solvus demarcates the IC and 1C phases.

129

6.4   PHASE TRANFORMATION IN $Fe_{1-x}S$ (0< x < 0.08)

This section reports our study of the mechanism of transformation of $Fe_{1-x}S$ (1C) phase to a mixture of FeS (2C) and iron poor $Fe_{1-x}S$ (1C) phases. This study was carried out in order to:

1)   resolve the controversy over the mechanism of phase separation (spinodal decomposition or nucleation and growth).

2)   explain the different microstructures of the two phase mixture, FeS (2C) and $Fe_{1-x}S$ (1C) (see Figures 4.4 and 6.4).

3)   obtain a diffusion coefficient of iron in $Fe_{1-x}S$ at 366 K.

4)   explain the nature and origin of the "intermediate" low temperature iron sulfide compounds.

6.4.1 EXPERIMENTAL DETAILS

The phase separation from $Fe_{1-x}S$ to FeS and $Fe_{1-x}S$ was investigated by a series of *in situ* cooling experiments. Some of these experiments comprise the cooling cycles of the *in situ* heating experiments described in Section 6.3. In all cooling experiments, the TEM sample was held at a temperature above T_α first in order to generate an initial single phase material; then, the temperature was reduced quickly to a lower temperature or to room temperature.

The phase transformation has been found to be impeded by the incident high energy electron bombardment. The nucleation of the troilite phase will not occur if the sample is viewed continuously. The high energy electrons, however, do not appear to interfere with the growth of the FeS precipitate significantly. Consequently, considerable effort has been devoted to minimize the electron exposure in the area studied. In all experiments, the process of phase separation is

disturbed by the electron beam only for a very short time during photography. The exposure time is always less than 4 seconds and the beam current is about 10-100 nA. The total exposure time in experiments that were carried out to study the growth velocity and iron diffusion coefficient was always less than 5% of the entire experiment duration.

6.4.2 PRELIMINARY OBSERVATION OF THE PHASE TRANSFORMATION

Figures 6.5 e,f,g,h show the evolution of the phase separation from $Fe_{1-x}S$ to FeS and iron-poor $Fe_{1-x}S$. At 390 K, the composition of the area shown in Figure 6.5e is $Fe_{0.97}S$ (49.14 at % Fe). The sample's temperature was reduced from 390 K to room temperature (298 K) in ten minutes. The sample was exposed to the electron beam during the cooling period. This prevents the occurrence of the phase transformation. At 298 K, the undercooling (T_α-T) was 92 K. The troilite FeS phase heterogeneously nucleates along the edge of the sample first (Figure 6.5f). Figure 6.5g shows a higher density of FeS precipitates one hour later. The higher concentration of FeS precipitates in the thicker region suggests that homogeneous nucleation is the dominant mechanism. The FeS precipitates are rod-like with sharp needle-like ends. Their long axes are always parallel to the $[1\bar{2}10]$ direction. Their length varies from 5nm to 30nm. The growth mechanism that gives rise to the rod-like shape will be discussed later. After 7 hours at room temperature, the population of the troilite FeS precipitates is very dense (Figure 6.5h). The microstructure of the two-phase mixture of FeS and $Fe_{1-x}S$ in Figure 6.5h is identical to that of Figure 4.4a and of Putnis (1975).

The phase separation mechanism is clearly that of a precipitation reaction. At first, the troilite FeS phase heterogeneously nucleates at the limited number of sites along the edge of the sample. The troilite phase also homogeneously nucleated

in the thicker region but with a slower and steadier rate. This phase continues to nucleate and grow until it covers the entire sample.

A different microstructure that resembles those shown in Figures 6.4a and 6.5a can also be formed by applying a different degree of undercooling. Figure 6.9 is a sequence of images showing the evolution of this phase separation process. In this experiment, the temperature was reduced from 390 K to 363 K. The sample was held at this temperature for about 10 minutes and then cooled to room temperature. At 363 K, the undercooling T_α-T is 27 K. The troilite FeS heterogeneously nucleates and grows along the edge of the sample. The super-critical nuclei grow very quickly (Figure 6.9a). The heterogeneously nucleated FeS elongates and develops a lenticular shape. This microstructure is similar to those in Figures 6.4a and 6.5a. Figure 6.9b shows the microstructure of the same region after seven hours at room temperature. The previously nucleated lenticular FeS precipitates are surrounded by a mixture of very small FeS rods and the $Fe_{1-x}S$ (1C) phase. The microstructure of this two-phase mixture surrounding the lenticular FeS precipitates is identical to that in Figure 6.5h. The lenticular-shape FeS precipitates are separated from the FeS and $Fe_{1-x}S$ mixture by a region of pure $Fe_{1-x}S$ (dark contrast region). This $Fe_{1-x}S$ region tapers off and eventually disappears at the tip of the large FeS needle.

The lenticular troilite is also observed in the thicker region away from the sample's edge (Figure 6.10) but the density of these large lenticular FeS precipitates is much lower than that at the edge of the sample. $Fe_{1-x}S$ is the only phase present if the region between two lenticular FeS precipitates is narrow.

The growth rate of the precipitates is highly anisotropic. They grow faster along the [1$\bar{2}$10] direction than the [0001] direction. Figure 6.11 is a plot of the square of the maximum width of the precipitate versus its length. Data used in this plot are from precipitates shown in Figure 6.10 and from precipitates in areas adjacent to Figure 6.10. The straight line behavior of Figure 6.11 suggests:

1.   diffusion-controlled parabolic growth rate for the side walls of the precipitate.

2.   interfacial reaction-controlled linear growth rate for the tip of the precipitate.

In the next two sub-sections we will present and discuss evidence supporting the above propositions.   We will also show that the occurrence of two microstructures, the large lenticular FeS precipitates which are surrounded by $Fe_{1-x}S$, and the mixture of small FeS rods and $Fe_{1-x}S$, can be attributed to the conditions of nucleation and growth. The microstructure of the former is favored when the heterogeneous nucleation sites are limited and the homogeneous nucleation rate is small relative to the growth rate. A large nucleation rate and a small growth rate favor the microstructure of the latter.

Before discussing the experimental results on nucleation and growth of FeS precipitates, we shall review several nucleation and growth models in the next   sub-section.   These are very well known models in the literature.   They are approximations to the real processes that occur during phase transformation. The nucleation model is highly idealized and can only be used to describe the nucleation of FeS qualitatively. However, the diffusion controlled growth model can be used to derive quantitative information since many of its assumptions can be met experimentally.   Results derived from this model will be used to estimate the diffusion coefficient of iron in $Fe_{1-x}S$.

6.4.3 THEORIES OF NUCLEATION AND GROWTH

In this section, we summarize important aspects of the classical theories of nucleation and growth. Extensive discussion of these theories can be found in books by Christian (1975) and Porter and Easterling (1981).

a)   Simple Nucleation Model

Assume that in the homogeneous nucleation process the nucleus is spherical with a radius of curvature r. The activation energy barrier is given by

$$\Delta G_c = (16\pi\gamma^3)/(3\Delta G_v^2) \qquad (6.1)$$

where

γ is the interfacial free energy

ΔG_v is the chemical driving force

In writing (6.1) we neglect the misfit strain energy since the difference in lattice parameters between FeS and $Fe_{1-x}S$ in relevant directions is extremely small (see Section 6.5, Figure 6.23).

The chemical driving force is assumed (for the sake of discussion) to be a linear function of undercooling

$$\Delta G_v = f\Delta T \qquad (6.2)$$

where

ΔT is the undercooling $(T_\alpha - T)$

f is the proportionality factor. f is a function of composition and temperature.

The activation energy barrier for homogeneous nucleation becomes

$$\Delta G_c = (16\pi\gamma^3)/(3f^2\Delta T^2) \tag{6.3}$$

In the heterogeneous nucleation processes we assume that the activation energy barrier is different from that for homogeneous nucleation by only a shape factor.

$$\Delta G^*_{Het} / \Delta G^*_{Hom} = S$$

The rate of nucleation is given by

$$I = [(kT)/h) \exp(-\Delta_a g^t/kT)][\mathcal{N} \exp(-\Delta G_c/kT)] \tag{6.4}$$

where

kT/h = "attempt" frequency

$\Delta_a g^t$ = activation energy for diffusion

$\mathcal{N}$ = number of possible nucleation site per unit volume.

The first term in square brackets on the right hand side of (6.4) is the rate each nucleus can be made supercritical. The second term in the square bracket is the concentration of critical-size nuclei.

The rate given by (6.4) is valid for both homogeneous and heterogeneous nucleation provided that the appropriate concentrations of nucleation sites and activation energy barriers are used. Figure 6.12 is a schematic sketch of the rate of nucleation as a function of undercooling. Note that at undercoolings smaller than the critical undercooling, the nucleation rate I is extremely small due to a very small

135

chemical driving force. At very high undercoolings, I is also negligible because the diffusion rate is too low. A maximum nucleation rate is obtained at intermediate undercoolings.

b)   Continuous Growth Model

Assume that the migration of an $\alpha|\beta$ interface is limited by the net rate at which atoms jump across the interface. The individual atomic processes involved in the phase transformation are treated as simply activated processes. An activation energy barrier must be overcome when atoms move from one phase to the other (see Figure 6.13). The rate of transfer of atoms from α to β is given by

$$\text{rate} = v_{\alpha\beta} \exp(-\Delta_a g^*/kT)$$

where $v_{\alpha\beta}$ is the attempt jump frequency from α to β.
The rate of transfer of atoms from β to α is given by

$$\text{rate} = v_{\beta\alpha} \exp(-\Delta_a g^*/kT) \exp(-\Delta g^{\alpha\beta}/kT)$$

where

$v_{\beta\alpha}$ is the attempt jump frequency from β to α

$\Delta g^{\alpha\beta}$ is the driving force for phase change

For simplicity, assume that the frequency factors are identical

$$v_{\alpha\beta} = v_{\beta\alpha} = v_0$$

136

The net rate of reaction is

$$\text{net rate} = \upsilon_0 \exp(-\Delta_a g^*/kT)\,(1-\exp(-\Delta g^{\alpha\beta}/kT)) \tag{6.5}$$

For a small $\Delta g^{\alpha\beta}/kT$, the second exponential in the above equation can be approximated by

$$\exp(-\Delta g^{\alpha\beta}/kT) = 1-(\Delta g^{\alpha\beta}/kT) $$

Therefore the interface migrates with velocity

$$v = \delta_B\, \upsilon_0 \exp(-\Delta_a g^*/kT)\,(\Delta g^{\alpha\beta}/kT) \tag{6.6}$$

where δ_B is the interface width.

Substituting (6.2) into (6.6), the velocity becomes

$$v = \delta_B \upsilon_0 \exp(-\Delta_a g^*/kT)\,(f\Delta T/kT) \tag{6.7}$$

Equation (6.7) is independent of time. The continuous growth model predicts a linear growth law.

The velocity is not only a function of undercooling but also depends on the thermal activated rate of transfer of atoms from α to β. Figure 6.14 illustrates the dependence of the growth rate on undercooling. At small undercoolings, the growth rate is small due to low chemical driving force. The growth rate is also small at large undercoolings due to a very small $\exp(-\Delta_a g^*/kT)$ exponential term. The growth rate is a maximum at intermediate undercooling.

c)   <u>Simple Diffusion-Controlled Growth Model</u>

Consider an one-dimensional growth model of a slab of solute-rich precipitate. Assume that the growth rate is limited by the transport of solute β to the interface and local equilibrium is achieved at the interface. Figure 6.15 shows the concentration profile across the precipitate. Since the concentration of solute in the precipitate (C_β moles of β) is higher than the bulk (C_0 moles of β) solute depletion zone adjacent to the precipitate is formed in the matrix (Figure 6.15b).

Assume that in a time increment dt, a unit area of interface advances a distance dx. This means that $(C_\beta - C_e)dx$ moles of β must be supplied by diffusion through the α phase (C_e is the concentration of solute in the matrix adjacent to the precipitate). This amount of β is equal to the flux of β through a unit area in time dt. Therefore

$$(C_\beta - C_e)dx = D(dC/dx)dt$$

where D is the interdiffusion coefficient.
The growth velocity is

$$v = dx/dt = (D/(C_\beta - C_e))(dC/dx)$$

As the precipitate grows, the solute β is depleted from an ever increasing volume of the α matrix. The concentration gradient dC/dx continuously decreases with time. If the concentration profile is approximated by that shown in Figure 6.15c, conservation of solute requires the two shaded areas in Figure 6.15c to be equal

$$(C_\beta - C_0)x = 0.5L\Delta C$$

138

where

$$\Delta C = C_0 - C_e$$

x is the thickness of the precipitate

Then dC/dx is equal to $\Delta C/L$

The growth rate becomes

$$v = dx/dt = D(\Delta C)^2/ (2(C_\beta - C_e)(C_\beta - C_0)x) \qquad (6.8)$$

Integration of (6.8) gives

$$x^2 = D(\Delta C)^2 K(t - t_0) - x_0^2 \qquad (6.9)$$

where

$$K = [(C_\beta - C_e)(C_\beta - C_0)]^{-1}$$

t_0 is the transient time before the growth rate becomes parabolic

x_0 is the precipitate's width before the growth rate becomes parabolic

Equation (6.9) indicates that the rate of thickening of the precipitates obeys a parabolic growth law. Note that Equations (6.8) and (6.9) are not valid when the diffusion fields of separate precipitates begin to overlap. The growth rate will decelerate more rapidly and stop when the matrix concentration is C_e everywhere.

6.4.4 RESULTS

The next three sub-sections will concentrate on the presentation and discussion of results of the investigation of the growth rates, growth mechanisms and diffraction studies of the $Fe_{1-x}S \longrightarrow FeS + Fe_{1-x'}S$ ($x < x'$) phase transformation.

139

A discussion of the relationship between the microstructure of the mixture of FeS and $Fe_{1-x}S$ and undercooling will be given in Section 6.4.4.4.

6.4.4.1 NUCLEATION RATE OF FeS

At this time we have not acquired enough data to generate a statistically sound plot of nucleation rate versus undercooling. Nevertheless, the nucleation rates shown in Figure 6.16 indicate a clear trend of the dependence of the nucleation rate on undercooling. The nucleation rates are small at both low and high undercoolings. The maximum nucleation rate is at some intermediate undercooling. This trend agrees with that discussed in Section 6.4.3 (see Figure 6.12). It is significant to note that nucleation will not occur unless the undercooling is greater than 22 K.

6.4.4.2. GROWTH RATES OF FeS PRECIPITATES

Figure 6.17 shows the evolution of a single precipitate as a function of time. The sample was cooled rapidly from 580 K to 366 K (about 2 minutes) and then it was held at this temperature for the duration of the experiment. The area of interest has an average composition of 49.14 at % Fe and the undercooling temperature is 24 K. The precipitate shown in Figure 6.17a was found about four minutes after the sample has reached 366 K. The length of the precipitate is plotted as a function of time in Figure 6.18. The growth of the length of the precipitate obeys a linear rate law (the linear correlation coefficient is 0.99996). The line intercepts the time-axis at (x-254 seconds). This value is in good agreement with the duration in which the sample is held at 366 K before the precipitate was found.

140

Six other cooling experiments have also been carried out to investigate the effect of undercooling on the growth rate. Figure 6.19 shows the data obtained from these experiments. In order to be plotted with the same origin, the x-time-intercept interval is added to each time datum. Note that when the undercooling is large (i.e. 25 to 35 K), the nucleation rate becomes very high (see Figure 6.16). The number of growth data is limited because the precipitates start to interfere with each other in a rather short time (about 10 minutes at $\Delta T = 35$ K). In these cases, the growth rate is determined by averaging the growth rate of several particles. Despite the small number of data points, the variation of these individual rates is always less than 6% (the linear correlation coefficient is always better than 0.995 for all sets of growth data and the variation in the growth rate between several precipitates at a particular temperature can be attributed entirely to the measurement errors). The growth rates shown in Figure 6.19 are also linear with time at all undercoolings. Figures 6.20 shows the dependency of the growth rate on undercooling. At small undercoolings, the growth rate is small but increases with increasing undercooling. The growth rate reaches a maximum at 361K and eventually decreases as the undercooling continues to increase.

The variation of the growth rate as a function of undercooling agrees qualitatively with that predicted by the continuous growth model (see Section 6.4.3). The quantitative fitting of the growth data to Equation 6.5 is, however, less successful. Complications arises because the chemical driving force is not only a function of temperature but also composition. The concentration of iron in the iron poor phase in the precipitation reaction $Fe_{1-x}S \longrightarrow FeS + Fe_{1-x'}S$ ($x < x'$) decreases as the undercooling increases (see phase diagram, Figure 6.6). The chemical driving force is therefore a complicated function of both composition and temperature. The activation energy $\Delta_a g^*$ also appears to be a function of composition. Since the

compositional dependency on the chemical driving force is not known, the quantification of growth data in terms of Equation 6.5 will not be carried out.

The growth of the side wall of the FeS precipitates has also been studied. Figure 6.21 is a plot of the square of the maximum width of a precipitate versus time. Data in this figure were obtained from the precipitate shown in Figure 6.17. The variation of the square of the width of a precipitate as a function of time can also be obtained by measuring the precipitate's width and the distance from the tip of the precipitate to the location where the width was measured. Because the length of the FeS precipitate grows linearly with time and the growth rate can be measured accurately, the time can be obtained from the tip to the point where the width is measured. Width squared versus time data obtained from this method are plotted in Figure 6.22. These data come from measurements of the precipitate shown in Figure 6.17g.

Figures 6.21 and 6.22 show that the growth rate of the side wall of the precipitate is linear in the first 100 seconds. The growth rate then decreases gradually and eventually becomes parabolic after about 1000 seconds. The change in the growth rate suggests the possibility of a change in the growth mechanism from interfacial reaction-controlled growth to diffusion-controlled growth. Evidence of a diffusion field will be discussed later.

The growth of the side wall of FeS precipitates at higher undercoolings was also investigated. The precipitate's width data were obtained from the same six cooling experiments that were used in the study of the growth rate of the precipitate length. Because the nucleation rate is high (see Figure 6.16) and the maximun experimental duration is always less than 1000 seconds, the growth rate never becomes parabolic. The diffusion fields of separate precipitates begin to overlap well before the growth mechanism changes from mixed-controlled growth to

142

diffusion-controlled growth. Plots of the square of the width of the precipitate versus time are very similar to Figure 6.22 and therefore will not be given here.

Several factors appear to influence the growth rate of the side wall during the transition from linear to parabolic growth rate. Besides the mixed-control mechanism, the diffusion field may also influence the growth rate. During this transition period, the width of the precipitate is smaller than the thickness of the sample. The diffusion field is therefore anisotropic and three dimensional. Discussion of growth rate in this type of diffusion field is beyond the scope of this thesis and therefore will not be given here.

A chemical diffusion coefficient of iron in $Fe_{1-x}S$ at 366 K can be estimated from the growth data in Figure 6.21 and Equation 6.8. Knowing that C_β = 50 at % Fe, C_0 = 49.14 at % Fe and C_e =48.62 at % Fe (according to the phase diagram, Figure 6.6), the calculated diffusion coefficient is D_c = 6.1 × 10^{-18} m^2/sec. This diffusion coefficient is roughly 75 time larger than the extrapolated value obtained from the high temperature radiotracer study of Condit et al. (1974) (see Figure 2.16). Note that the assumption of a planar interface made in the diffusion-controlled growth model is nearly satisfied at the maximum width of the precipitate (Figures 6.16e,f,g,h).

So far we have shown that the growth rate of the FeS precipitate is highly anisotropic. The growth rate is linear at the tip, but it changes from linear to parabolic at the side wall. At this point we give further evidence suggesting that the growth rate at the tip of the FeS precipitate is controlled by the interfacial reaction and that the growth rate of the side wall of the precipitate is eventually controlled by the diffusion field.

There are two important factors suggesting an interfacial reaction growth mechanism for the tip of the precipitate. They are:

(1)   faster iron diffusion coefficient along the c-direction (D_c/D_a = 1.76).

143

(2)   the tip of the precipitate is almost atomically sharp (Figure 6.23) (it also

        means that the interfacial free energy is very small) .

(1) and (2) prevent the establishment of a diffusion field in front of the precipitate. The tip extends into the $Fe_{1-x}S$ matrix by incorporating iron atoms from the adjacent matrix. The iron vacancies rejected by the precipitate diffuse out on either side of the precipitate. These vacancies eventually set up an iron concentration gradient normal to the precipitate's length. Since the tip grows into the matrix, its growth velocity is limited by the interfacial reaction that incorporates $Fe_{1-x}S$ from the adjacent matrix to the FeS precipitate.

Evidence of a diffusion field adjacent to the side wall can be deduced from Figure 6.10. Recall from the simple diffusion-controlled growth model that there is a solute depletion zone surrounding the precipitate.   Also recall that the microstructural features shown in Figure 6.10 were generated by first reducing the temperature from 390 K to 353 K. The sample was held at this temperature for about 10 minutes and then cooled to room temperature. The large lenticular shape FeS precipitates were formed at 353 K and the small mixture of FeS and iron poor $Fe_{1-x}S$ was formed at room temperature. Surrounding the large FeS precipitate is a region of pure $Fe_{1-x}S$ (dark contrast region). This region is believed to be the iron depletion zone. In this region the iron concentration was lower than that of the matrix (see Figure 6.15b) and hence the thermodynamic driving force was lower than that of the matix when the sample was cooled at room temperature. It appears the driving force was sufficiently low so that the nucleation of FeS precipitates did not occur .

144

6.4.4.3 NATURE AND ORIGIN OF THE INTERMEDIATE
IRON SULFIDE COMPOUNDS

Diffraction studies of the $Fe_{1-x}S \longrightarrow FeS + Fe_{1-x'}S$ ($x < x'$) phase transformation have also been carried out during the *in situ* cooling experiments. These studies revealed the nature and origin of the "intermediate" or "hexagonal" low temperature iron sulfide compounds. Figures 6.7f,g,h,i,j and 6.8e,f,g,h are sequences of diffraction patterns taken prior to and during the phase transformation. Figures 6.7 h,i,j are patterns diffracted from areas in Figures 6.5 f,g,h respectively. Recall that the average iron composition of the areas shown in Figure 6.5 is 49.14 at % Fe and the incident electron beam is parallel to the $[0\overline{1}10]$ direction. The average iron composition of the selected areas that form the diffraction patterns of Figure 6.8 is 49.5 at % Fe. The incident beam is parallel to the $[1\overline{2}10]$ direction.

Figure 6.7f was taken at 368 K. The undercooling is 22 K and just above the critical temperature for nucleation. In the figure, considerable diffuse scattering was observed indicating atomic relaxation and/or local ordering. The superstructure reflections of the 1C phase are also highly diffuse.

The diffraction pattern shown in Figure 6.7g was taken right after the sample reached 353 K and just before the beginning of the nucleation of FeS precipitates. This diffraction pattern differs significantly from that of Figure 6.7f. The diffuse scattering disappeared. The 1C superstructure reflections are distinct. These reflections are different from those of Figures 6.7a,b,c,d. A group of three satelite reflections was observed rather than the group of two reflections seen in Figure 6.7a (see horizontal arrow in Figure 6.5g). At 298 K, the 2C superstructure reflections of the troilite phase reappeared (Figure 6.7h). The 1C superstructure reflections are similar to those in Figure 6.7g. At 298 K and one hour later (Figure 6.7i), the 1C superstructure reflections changed from a group of three satelite reflections to a

group of two reflections. They are similar to Figures 6.7 a,b,c,d. No further change was observed at later time (Figure 6.7j). Apparently the gradient in iron concentration which inevitably occurs during the phase transformation modifies the superstructure reflections of the ⚊C phase drastically.

The diffraction patterns shown in Figures 6.8e,f,g,h display similar behavior to that of Figures 6.7f,g,h,i,j. In Figures 6.8f and 6.8g, the superstructure reflections of the ⚊C phase are different from those of Figures 6.8a,b,c,h. More significantly, these superstructure reflections are identical to those of the 5C superstructure and very similar to the superstructure reflections of the 11C "intermediate" low temperature iron sulfide compound! (see Figures 2.3 and 2.4). The "superstructure" reflections are also incommensurate with the main reflections. The "superstructure" dimension varies from 5.07C at 418 K to 6.16C at 298 K (Figures 6.8e-h). Finally, note that the diffraction patterns of Figures 6.8a and 6.8h are identical.

The major finding of this sub-section is that the diffraction patterns of the phase transforming $Fe_{1-x}S$ system are similar or identical to the diffraction patterns of the intermediate low temperature pyrrhotite.

6.4.4.4 MICROSTRUCTURE OF FeS AND $Fe_{1-x}S$

It is clear from Section 6.4.4.1. and 6.4.4.2 that the undercooling and hence the rates of nucleation and growth control the final microstructure of the mixture of FeS and $Fe_{1-x}S$ phases. The difference in microstructures shown in Figures 6.5, and 6.9 arises as a direct consequence of different undercoolings. Figure 6.24 illustrates the undercooling, the supersaturation prior to precipitation and the rates of nucleation and growth of FeS precipitates that occur during the phase transformation.

At 363 K (Figures 6.9a and 6.10), the undercooling was 27 K and the supersaturation concentration C_0-C_e was 0.5 at % Fe. The rate of homogeneous

146

nucleation was low (see Figure 6.24). The heterogenous nucleation rate was somewhat higher. However, the heterogeneous nucleation sites along the sample's edge were exhausted very quickly. The growth rate was very high. The combination of these factors gave rise to a final microstructure of a low density of very large FeS precipitates (see Figures 4.4b and 6.5a).

At 298 K (Figures 4.4a and 6.5h), the undercooling was 92 K and the supersaturation concentration C_0-C_e was 1.29 at % Fe. The growth rate was very low and the homogeneous and heterogeneous nucleation rates were high relative to the growth rate (see Figure 6.24). The heterogeneous nucleation sites again were exhausted very quickly. Direct evidence of high nucleation rates and low growth rate was revealed in the microstructures of Figures 6.5 f,g,h.

6.5 STRUCTURES AND INTERFACES OF FeS and $Fe_{0.92}S$

This section reports the diffraction and high resolution transmission electron microscope studies of prominent structural features of FeS and $Fe_{0.92}S$ and the interface between FeS and $Fe_{0.92}S$. This section is organized into three sub-sections. The first delineates the high resolution transmission electron microscopic study of the troilite 2C structure. The second sub-section describes evidence of local ordering of iron vacancies in $Fe_{0.92}S$ crystals. The third sub-section examines the interfaces between the FeS precipitate and the matrix $Fe_{0.92}S$. At this point, we remind the reader that high resolution transmission electron microscopy is a very powerful technique for studying defects and interfaces. It can also be used for qualitative investigation of structures of materials. It, however, does not have the precision of x-ray or neutron diffraction techniques. This section describes only the prominent structural features of FeS and $FeO_{.92}S$, but not the exact structures .

6.5.1 HRTEM STUDY OF FeS

A series of image simulations was carried out in order to:

1) establish the most favorable conditions for direct imaging of the troilite structure in the JEM 4000EX and the MIT JEM 200CX microscope.

2) assess the sensitivity of high resolution transmission electron microscope images to small structural changes.

6.5.1.1 EXPERIMENTAL DETAILS

The microscopy was carried out using an ASU JEOL JEM 4000EX microscope. All samples were ion-thinned to electron transparency at 123 K.

The image simulation of the troilite structure was carried out using the SHRLI suites of program and the ASU multislice programs. The input structure of troilite is that of King and Prewitt (1982; see Section 2.4).

The assessement of the sensitivity of high resolution transmission electron microscope images to small structural changes is carried out by comparing the lattice images of the 1C and 2C structures.

6.5.1.2 RESULTS

An important consideration in performing high resolution transmission electron microscopy is the selection of projected direction. Appropriate projected structure should be selected to optimize the amount of information contained in the lattice image. There are two important criteria involved in this selection . They are:

1) structural information contained in the projected structure.

2) distances between atoms. Ideally, the interatomic distances should be greater than the point resolution of the electron microscope.

Since the weak phase object point resolution of the ASU JEM 4000EX microscope is 1.7Å, an obvious choice of direction for high resolution electron microscopy is the [1$\bar{2}$10] direction. Figures 6.25a,b show the projections of the NiAs (1C) and troilite 2C structures along the [1$\bar{2}$10] direction ([100] for the 1C sructure and [120] for the 2C structure). In this direction the projected sulfur atoms are arranged in an ABAB sequence. The projected iron atoms align into columns along the [0001] direction and rows along the [0$\bar{1}$10] direction. The small displacements of the iron and sulfur atoms in the troilite structure can be seen clearly in Figure 6.25b. The iron-iron or sulfur-sulfur distance is 2.9Å and the iron-sulfur distance is 1.7Å.

Figures 5.7 and 6.26 are respectively through-focus and through-thickness series of image simulation of the 1C and 2C structures along the [1$\bar{2}$10] direction . The electron optical parameters are that of the ASU JEM 4000EX microscope. The lattice images from these figures indicate that the iron and sulfur atoms can be resolved only when the thickness is one unit cell thick (0.34nm for 1C and 1.0 nm for 2C structures) and the focus is at "optimum" setting (-49.6nm). When the thickness is greater than one unit cell the strong dynamical interaction between the high energy electron and the sulfur and iron atoms smears out the atom projection and therefore renders impossible resolution of the iron-sulfur distance. The smeared projection images of iron and sulfur atoms form wavy patterns. These wavy images exist in a wide range of thickness and focus. Figure 6.27 shows a high resolution transmission electron microscope image of the troilite 2C structure along the [120] |[1$\bar{2}$10] direction. The inset calculated image (with focus setting of -33.6nm and 2.5nm thick) matches reasonably well with the experimental image. The arrow

149

indicated in Figure 6.27 shows a discontinuity at the iron site indicating a highly vacant iron column.

An important conclusion drawn from Figure 6.26 is that at 1.7 $\overset{o}{A}$ WPO point resolution and in the [120]|[1$\bar{2}$10] direction the images are not sensitive to the small atomic displacements. The images of the 1C and 2C structures are virtually indistinguishable over a wide range of focus and thickness.

An alternative suitable for high resolution electron microscopy is the [0$\bar{1}$10] direction. In this direction the iron and sulfur atoms of the 1C structure line up into rows and columns (Figure 6.28a). The iron-iron or sulfur-sulfur distance is 1.7 $\overset{o}{A}$. The iron-sulfur distance is 1.45$\overset{o}{A}$. The displacements of the iron and sulfur atoms in the troilite structure are quite pronounced (Figure 6.28b). The atoms are displaced in such a way that "holes" can be seen in the troilite projected structure. These holes form a zig-zig-zag-zag sequence along the c-direction.

Figures 6.29 and 6.30 are respective through-focus and through-thickness series of image simulation of the 1C and 2C structures along the [0$\bar{1}$10] direction. These image simulations show significant differences in contrast among the lattice images of the 1C and 2C structures. Figure 6.29 confirms that the 1.7$\overset{o}{A}$ distance between the iron-iron or sulfur-sulfur atoms can be resolved for a wide range of focus settings and thicknesses. The zig-zig-zag-zag sequence of the "holes" in the troilite projected structure is observed at optimal (-49.6 nm) focus setting (Figure 6.30). Note that the image contrast varies significantly as a function of focus.

A through-focus series of image matching was carried out for the troilite structure. Figure 5.11 shows reasonably good agreement between experimental and calculated images.

When the interatomic distances in the projected structure are smaller than the point resolution, the interpretation of high resolution transmission electron micrographs becomes formidable. The contrast of the image usually contains little

150

information about the actual atomic locations. Figure 6.31 shows a through-focus and through-thickness series of image simulation of the 2C structure along the $[0\bar{1}10]$ direction. The electron optical parameters are those of the MIT JEM 200CX. The simulated images bear no resemblance to the projected structure.

In this section we have established that the $[0\bar{1}10]$ direction as a more suitable direction for direct imaging of the troilite and 1C structures. The interpretation of high resolution electron microscopic images is far from straightforward despite a resolution of 1.7Å. In most of the above simulations, it is evident that important structural features can be directly recognizable only under very restricted imaging conditions and for very thin crystals. The interpretation of images beyond the resolution limits of a particular microscope is reliable only when it is accompanied by image simulation.

6.5.2 LOCAL ORDERING OF IRON VACANCIES IN $Fe_{0.92}S$

In this section, we present diffraction and high resolution transmission electron microscopic results suggesting that iron vacancies locally order in the iron planes.

6.5.2.1 EXPERIMENTAL DETAILS

Electron microscopy was carried out using an ASU JEM 4000EX and two MIT JEM 200CX electron microscopes. The TEM samples were ion thinned with the specimen stage held at 123 K.

6.5.2.2 RESULTS

Evidence indicating that the iron vacancies in $Fe_{0.92}S$ crystals order in the iron planes comes from the x-ray and electron diffraction patterns of the [0001] pole. The reflections labelled IC shown in Figures 6.2 and 6.3 can be associated with the ordering of the iron vacancies depicted in Figure 2.10. The extent in which the vacancies order within the iron plane and the possibility of superstructure formation were investigated by high resolution transmission electron microscopy with the incident beam parallel to the $[0\bar{1}10]$ and $[1\bar{2}10]$ directions. Figure 6.32 shows a lattice image of the IC phase. The incident beam is parallel to the $[1\bar{2}10]$ direction. The inset is a calculated image of a structure that has highly-vacant iron columns (in this case, we use the 3C structure). The focus and thickness values for the experimental and calculated images are -33.6 nm and 5nm respectively. The calculated image shows that the contrasts of the highly-vacant iron columns are bright (the vacancy columns are located at the discontinuities of the wavy patterns). Observed in Figure 6.32 are numerous columns of iron vacancies (see arrows in Figure 6.32). The vacancy columns do not form superstructure. The area labeled IC in Figure 6.33 is lattice image of $Fe_{0.92}S$. The incident beam is parallel to the [0110] direction. This area also shows no evidence of superstructure. The diffuse scattering in the optical diffraction (inset diffraction pattern) taken from the IC regions agrees with that in the electron diffraction pattern (Figure 6.3b).

6.5.3 STRUCTURE OF $FeS/Fe_{1-x}S$ INTERFACE

The structure of the $FeS/Fe_{1-x}S$ interface was investigated in order to:

1) determine the coherency of the interface.

2) determine the sharpness of the tip of the FeS precipitate.

This study was carried out using high resolution transmission electron microscopy. The instruments employed in this investigation were the ASU JEM 4000EX and the MIT JEM 200CX microscopes.

6.5.3.1 RESULTS

Figure 6.34 is a high resolution electron micrograph of a mixture of FeS and $Fe_{1-x}S$ phases. Figure 6.33 shows the $FeS/Fe_{1-x}S$ interface of an area near the tip of a precipitate. As expected, the interface is perfectly coherent because of the very small difference in lattice parameters between the 2C and 1C phases along the $[1\bar{2}10]$ direction. Figure 6.34 shows some very small FeS precipitates. The precipitate's width can be less than two unit cells long. Figure 6.23 is a high resolution electron micrograph of an FeS precipitate that is embedded in the $Fe_{1-x}S$ matrix. The lattice (1.7Å) of the IC phase cannot be imaged because of the limited pass band of a 3.1Å WPO point resolution electron microscope. The lattice image of the 2C phase was formed mainly from the interference between the 2C superstructure reflections and the transmitted beam. The tip of the FeS precipitate is quite sharp. At the tip, the width is 11.75Å (one unit cell wide). Away from the tip of the FeS precipitate, the $FeS/Fe_{1-x}S$ interface is quite smooth. Near the tip of the FeS precipitate, the interface becomes rougher. Note that the tip is asymmetric. This is due to the interference of a nearby precipitate. The lattice image of Figure 6.23 is in good agreement with the simulate images at optimum focus setting (-102.4 nm) shown in Figure 6.31.

6.6 SUMMARY AND DISCUSSION

Major conclusions in this chapter are:

1) the high temperature 1C phase transforms into an 1C phase at lower temperature. The phase transformation appears to be first order.

2) at T_{α}, the $Fe_{1-x}S$ (1C) phase decomposes to FeS (2C) phase and an iron-poor $Fe_{1-x'}S$ (1C) (x < x') phase.

3) the 1C phase has an incommensurate superstructure. The positions of the superstructure reflections vary with composition and temperature. The iron vacancies in the 1C phase appear to order locally in the iron planes.

4) the phase separation mechanism of reaction $Fe_{1-x}S$ (1C) --> FeS (2C) + $Fe_{1-x'}S$ (1C) (x < x') is nucleation and growth.

5) the growth rate of the length of FeS precipitates obey a linear rate law. The growth rate appears to be controlled by the interfacial reaction.

6) the growth rate of the side walls of FeS precipitates is linear initially and eventually becomes parabolic. The growth mechanism in the parabolic regime appears to be a diffusion-controlled reaction.

7) the dependency of the growth rate on undercooling agreed qualitatively with that predicted by the continuous growth model.

8) the $FeS/Fe_{1-x}S$ interface is coherent. The tip of the FeS precipitate is almost atomically sharp. Away from the tip, the $FeS/Fe_{1-x}S$ interface is smooth.

9) the "intermediate" pyrrhotite appear to be artifactual. The diffraction pattern of $Fe_{1-x}S$ that is undergoing a phase transformation is identical or similar to that of the "intermediate" pyrrhotite.

The solvus separating the 1C phase from the two-phase field 2C and 1C is in fairly good agreement with those of Sugaki and Shima (1977) and Yund and Hall (1968) (Figure 6.35). It is unclear why Nakazawa and Morimoto (1970) and Sugaki

154

and Shima (1977) did not observe the $1C$ phase. The 5C and 7C structures observed by Yund and Hall and Carpenter and Desborough are clearly those of the quenched $1C$ phase. The transformations of FeS reported by King and Prewitt (1982) are consistent with our phase diagram. King and Prewitt also observed the extra reflections of the $1C$ phase (Figure 6.2a); they, however, concluded that these reflections are those of the high temperature stoichiometric MnP structure. Since these $1C$ phase reflections were also observed at room temperature in this study, it is possible that the crystal used by King and Prewitt in the heating experiment is not stoichiometric FeS but rather iron poor $Fe_{1-x}S$.

Conclusions by Putnis (1975) that stoichiometric FeS decomposes spinodally to two compounds with compositions lying on either side of the stoichiometric composition are obviously incorrect. The microstructure observed by Putnis is the manifestation of a nonstoichiometric $Fe_{1-x}S$ sample that was ion thinned at room temperature. The sample's temperature was raised above T_α during ion thinning and it was effectively quenched to room temperature afterward. Our results clearly demonstrate that the transformation mechanism cannot be inferred from the microstructure alone.

Crystals used by Sparks et al. (1962) and Thiel and Van den Berg (1968, 1970) appear to be the nonstoichiometric $Fe_{1-x}S$ ($0<x<0.08$). They observed the transformation $Fe_{1-x}S \dashrightarrow FeS + Fe_{1-x'}S$ ($x < x'$)!.

The fact that the diffraction patterns of $Fe_{1-x}S$ that is undergoing a phase transformation are similar or identical to those of the intermediate compounds raises serious doubts about the genuine nature of these compounds. Many reports on the intermediate compounds used synthetic crystals. The synthetic techniques used in these reports lacked the careful control of the sulfur partial pressure and hence composition. $Fe_{1-x}S$ with composition near $Fe_{0.92}S$ will not phase separate to FeS and iron poor $Fe_{1-x}S$ due to a low chemical driving force. It appears that the

155

intermediate compounds reported in the literature are either the $\underline{C}$ phase or the $\underline{IC}$ phase that is experiencing a phase transformation.

Average composition of the two phase mixture is 49.14 at % Fe.

TEMPERATURE (KELVIN)	ANNEALING TIME	DIFFUSION COEFFICIENT* (m^2/sec)	$X = \sqrt{Dt}$ (nm)	WEIGHT FRACTION OF $Fe_{1-x}S$	COMPOSITION OF $Fe_{1-x}S$ (at % Fe)
298	6 years	1.1×10^{-22}	144.3	40.00	47.85
338	25 hours	7.5×10^{-21}	25.9	44.72	48.07
359	8 hours	4.6×10^{-20}	36.4	53.70	48.40
366	5 hours	8.1×10^{-20}	38.1	61.19	48.59
390	2 hours	4.7×10^{-19}	58.3	95.60	49.10

(*) Diffusion data are from Condit et al. (1974)

Table 6.1. Composition and thermal history of data used in the construction of solvus separating the 1C phase to the 2C and iron poor 1C phases
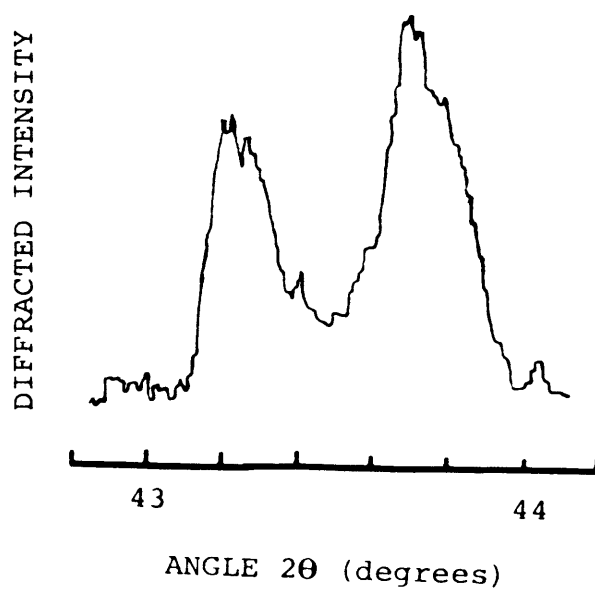
Figure 6.1. Power x-ray diffraction pattern of $Fe_{1-x}S$ showing two distincts peaks at $2\theta_B = 43.2 \pm 0.1^0$ and $2\theta_B = 43.7 \pm 0.1^0$.

Figure 6.2. Precession photographs of pyrrhotite taken about (a) [0001],
(b) [1$\bar{2}$10], (c) [0$\bar{1}$10] directions. The strong reflections correspond to
the NiAs-type substructure.
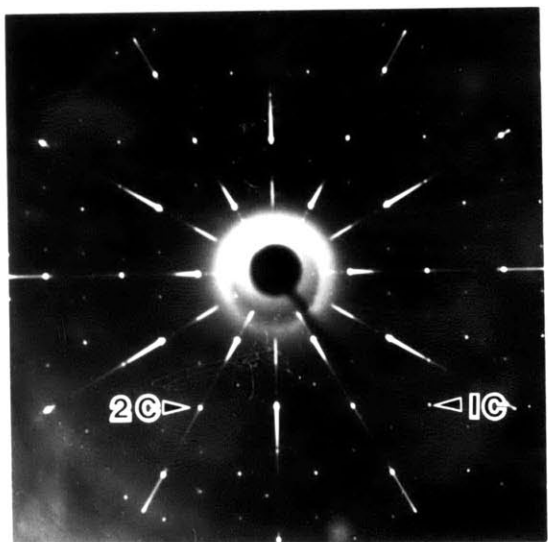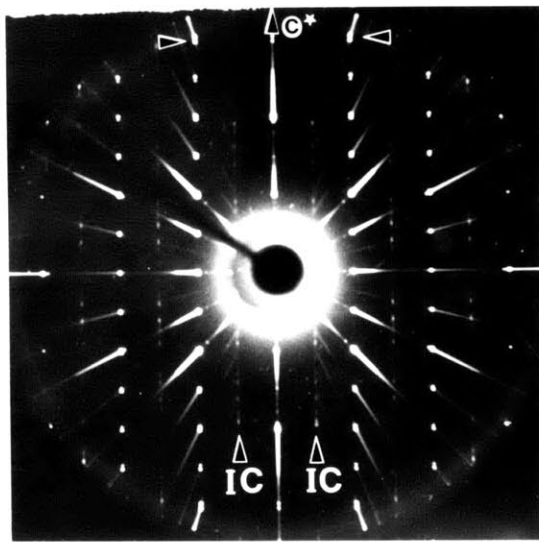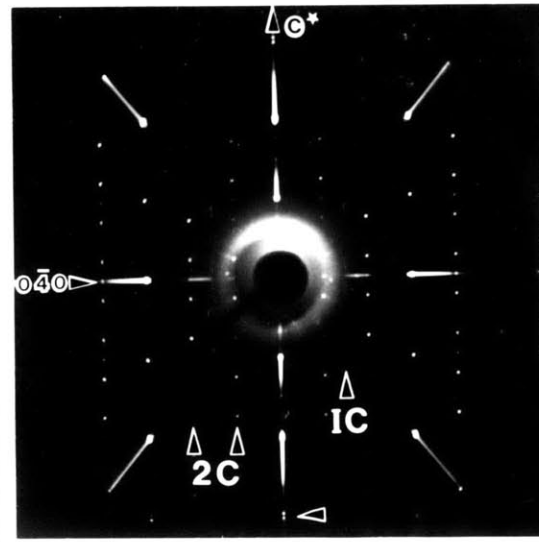
(a)   (b)   (c)

Figure 6.3. Electron diffraction patterns of $Fe_{1-x}S$ taken about (a) [0001],
(b) [$1\bar{2}10$] and (c) [$0\bar{1}10$] directions.
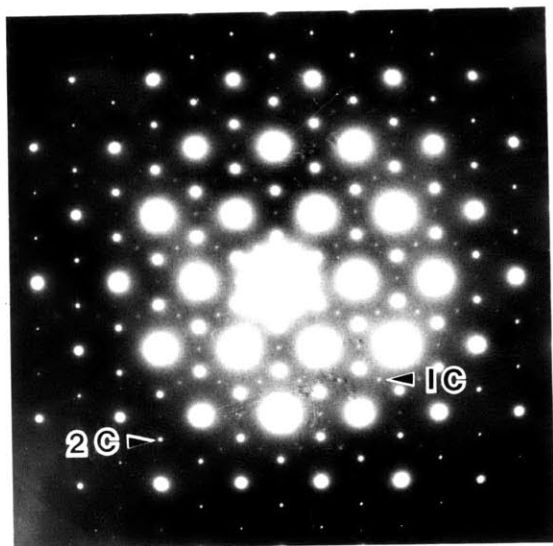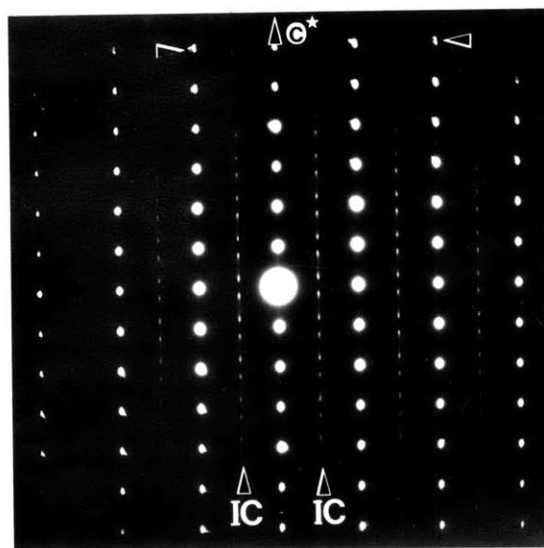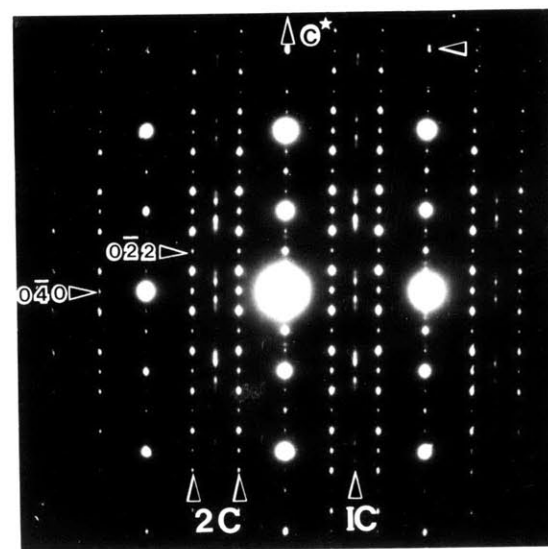
(a)   (b)   (c)
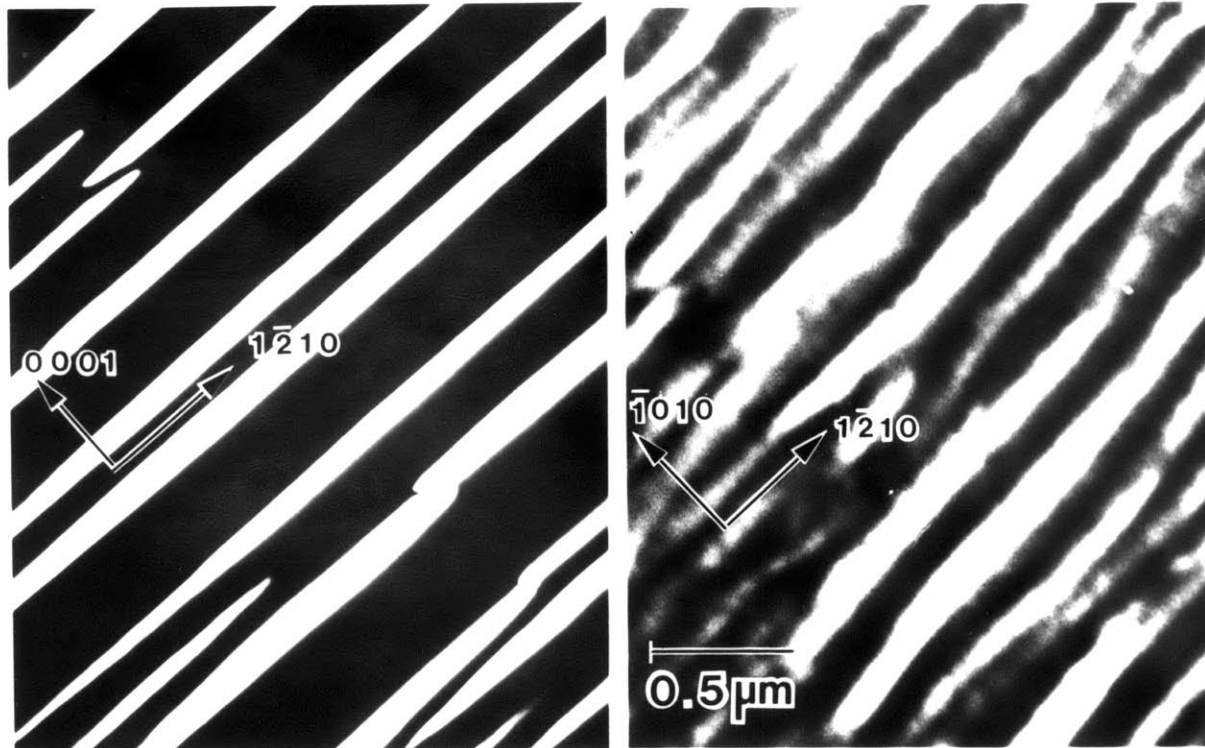
Figure 6.4. Dark field images formed by superstructure reflections of the troilite phase.

Figure 6.5. Evolution of composite structure of FeS and $Fe_{1-x}S$ as a function of temperature.

HEATING ⟶

298K   338K   365K   378K

0.2 μm
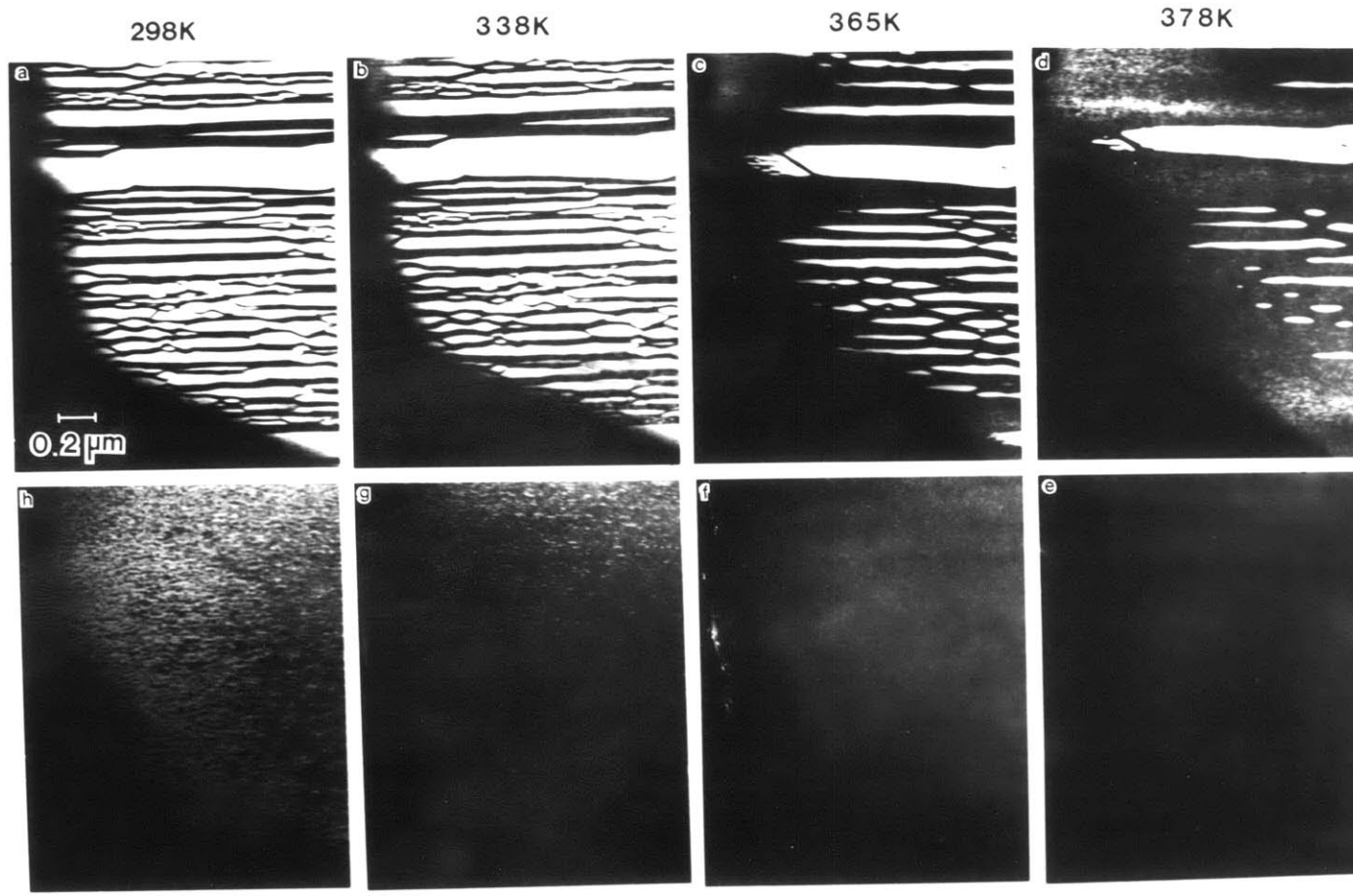
298K-7HRS   298K-1HR   298K   390K

⟵ COOLING
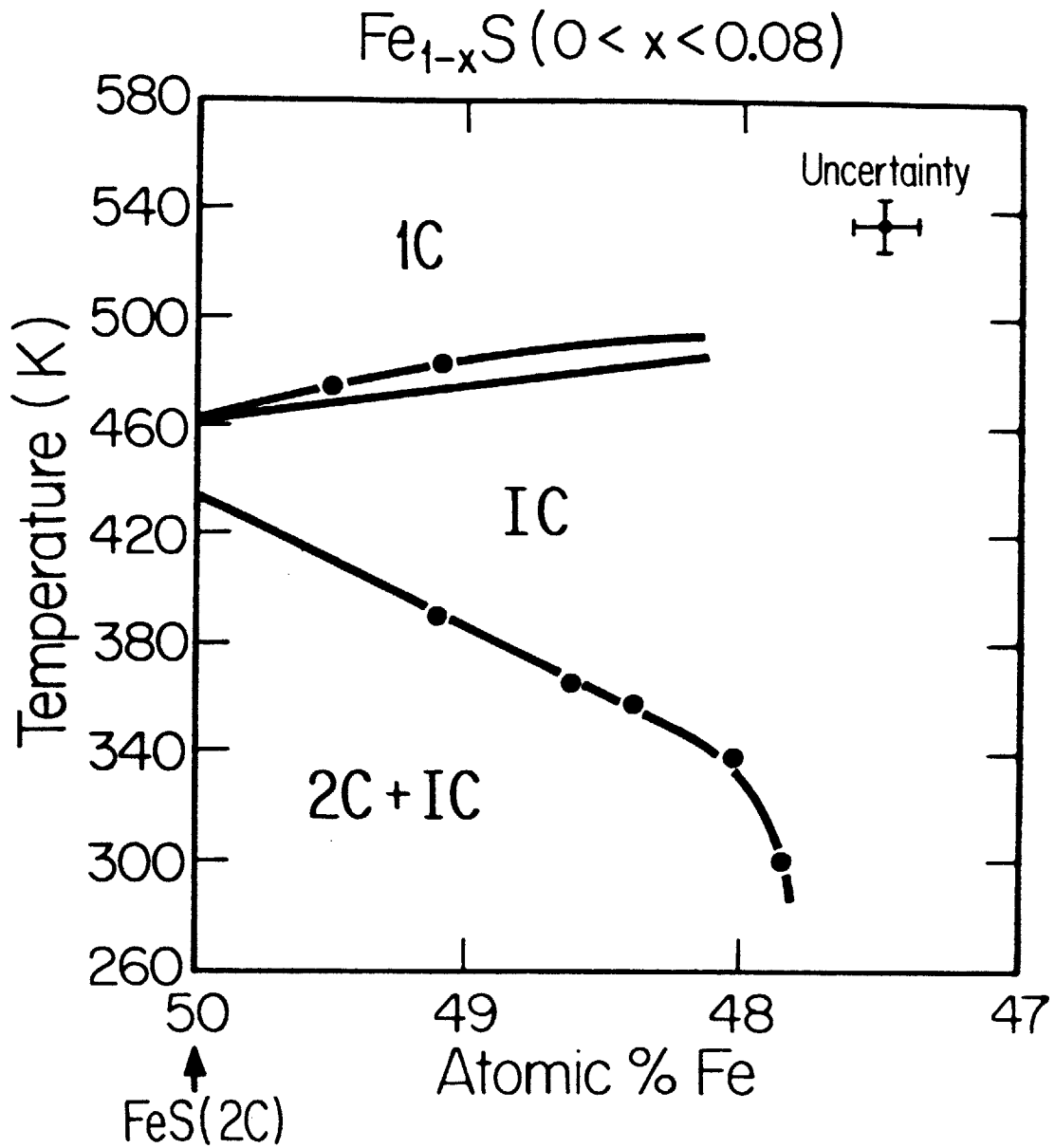
Figure 6.6. Phase diagram of the FeS–Fe$_{0.92}$S system constructed from the results of this study.

Figure 6.7. Selective area diffraction patterns of $Fe_{1-x}S$ or a mixture of FeS and $Fe_{1-x}S$ at seven different temperatures. The incident beam direction is parallel to $[0\bar{1}10]$ direction.

HEATING →

298K   338K   365K   390K   493K

$\triangle c^*$ a

2C   IC

b

c

d

IC   IC

e

1C-NiAs

j

i

h

g

f

298K-7HRS   298K-1HRS   298K   353K   368K
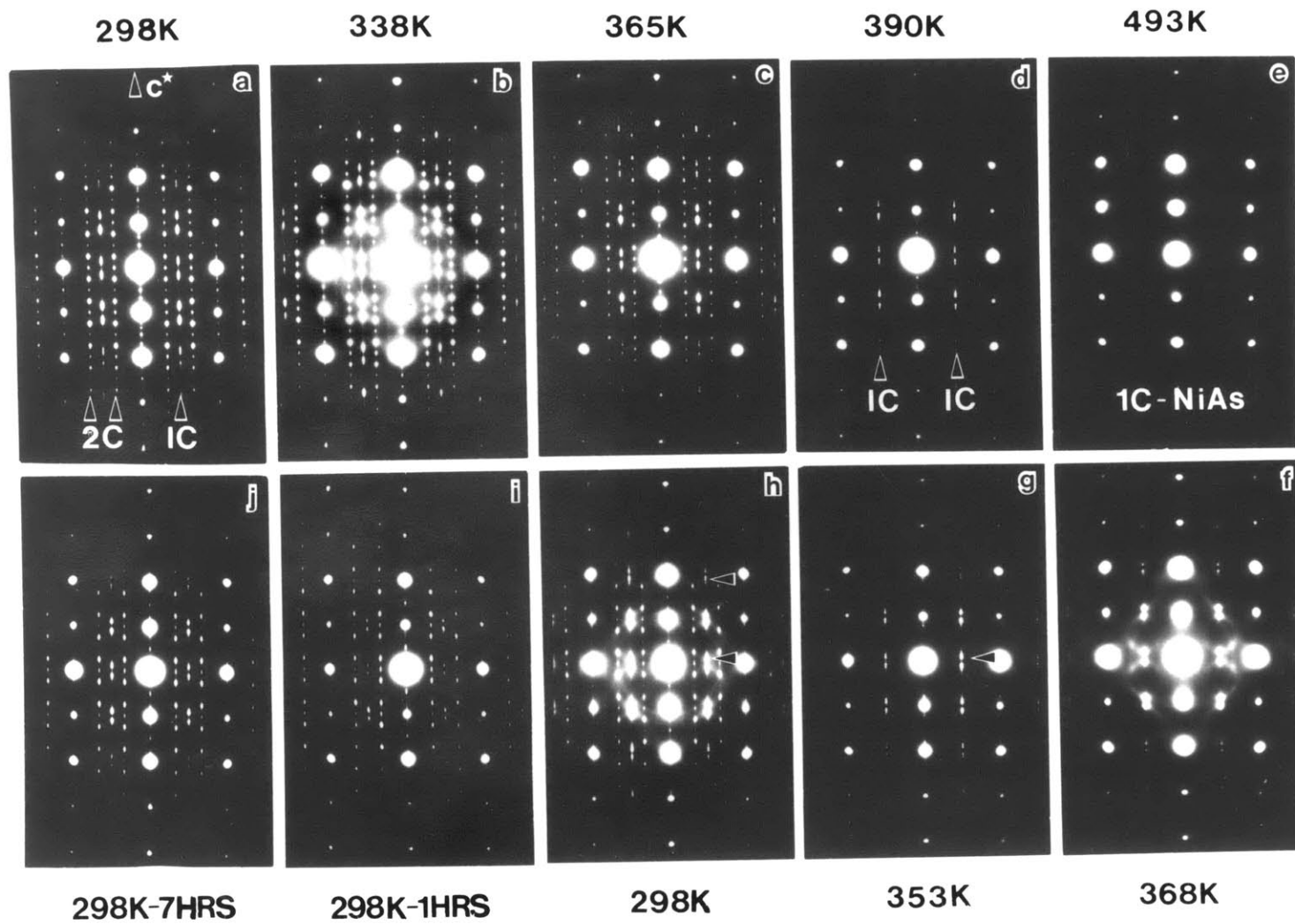
← COOLING

Figure 6.8. Selective area diffraction patterns of $Fe_{1-x}S$ or a mixture of FeS and $Fe_{1-x}S$. The incident beam direction is parallel to $[1\bar{2}10]$ direction.
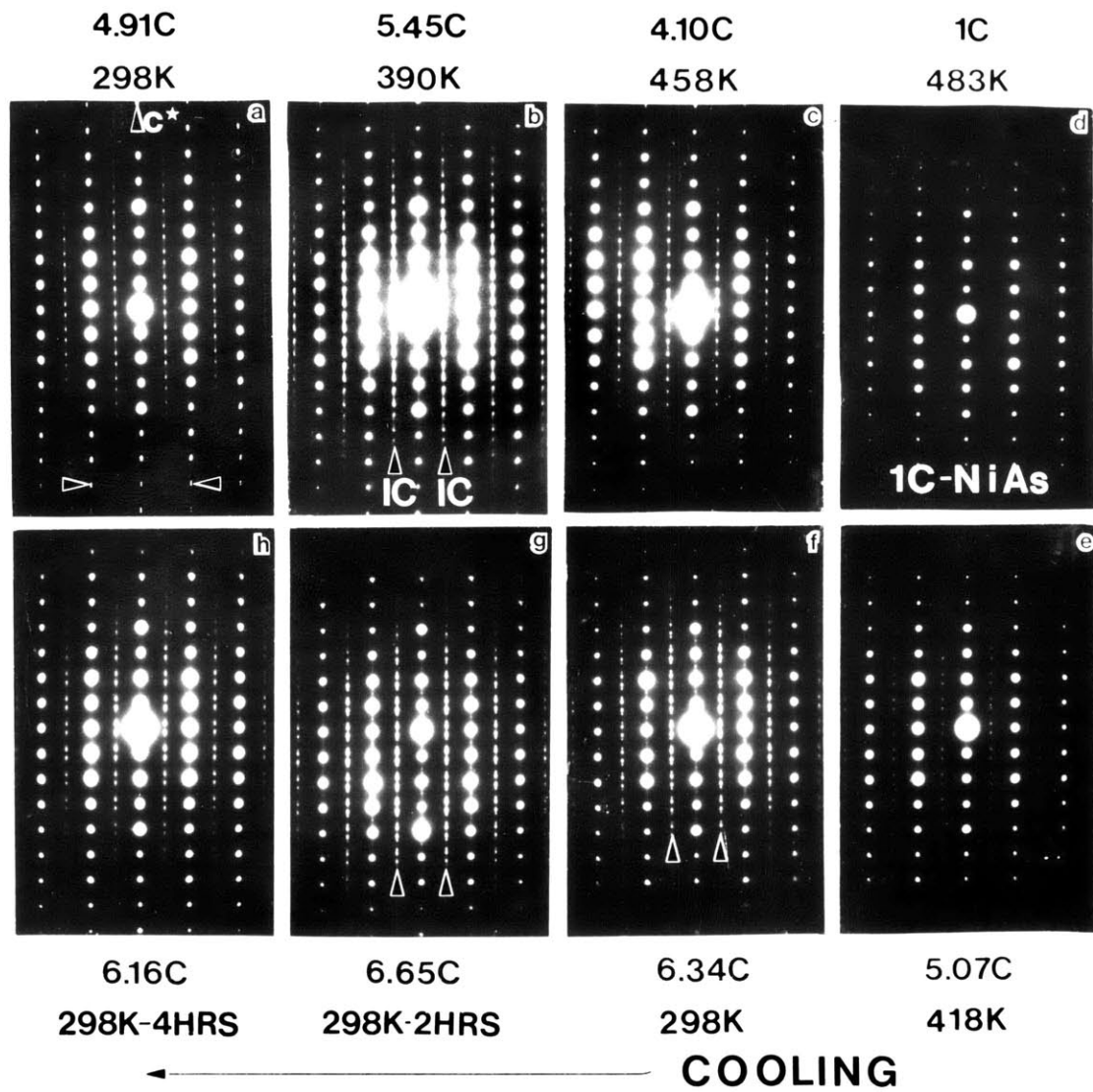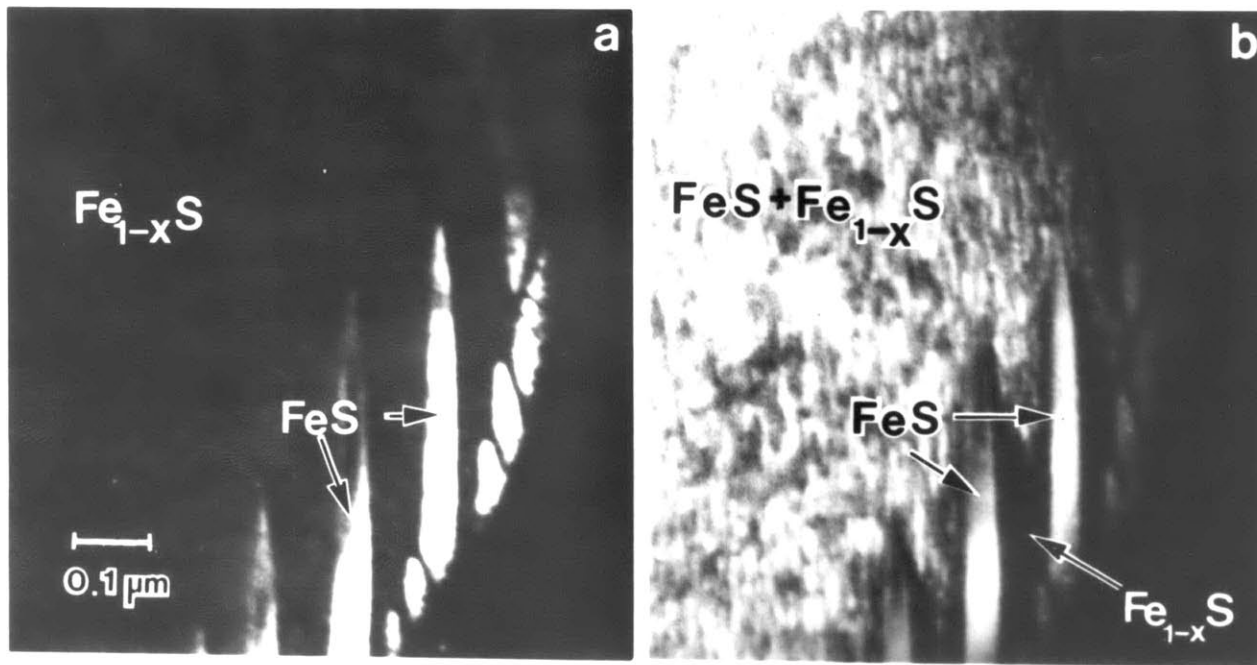
Figure 6.9. Microstructures of a mixture of FeS and $Fe_{1-x}S$. (a) the sample was held at 363 K for about 10 minutes. The undercooling was 27 K. (b) micrograph taken after the sample was at room temperature for seven hours.
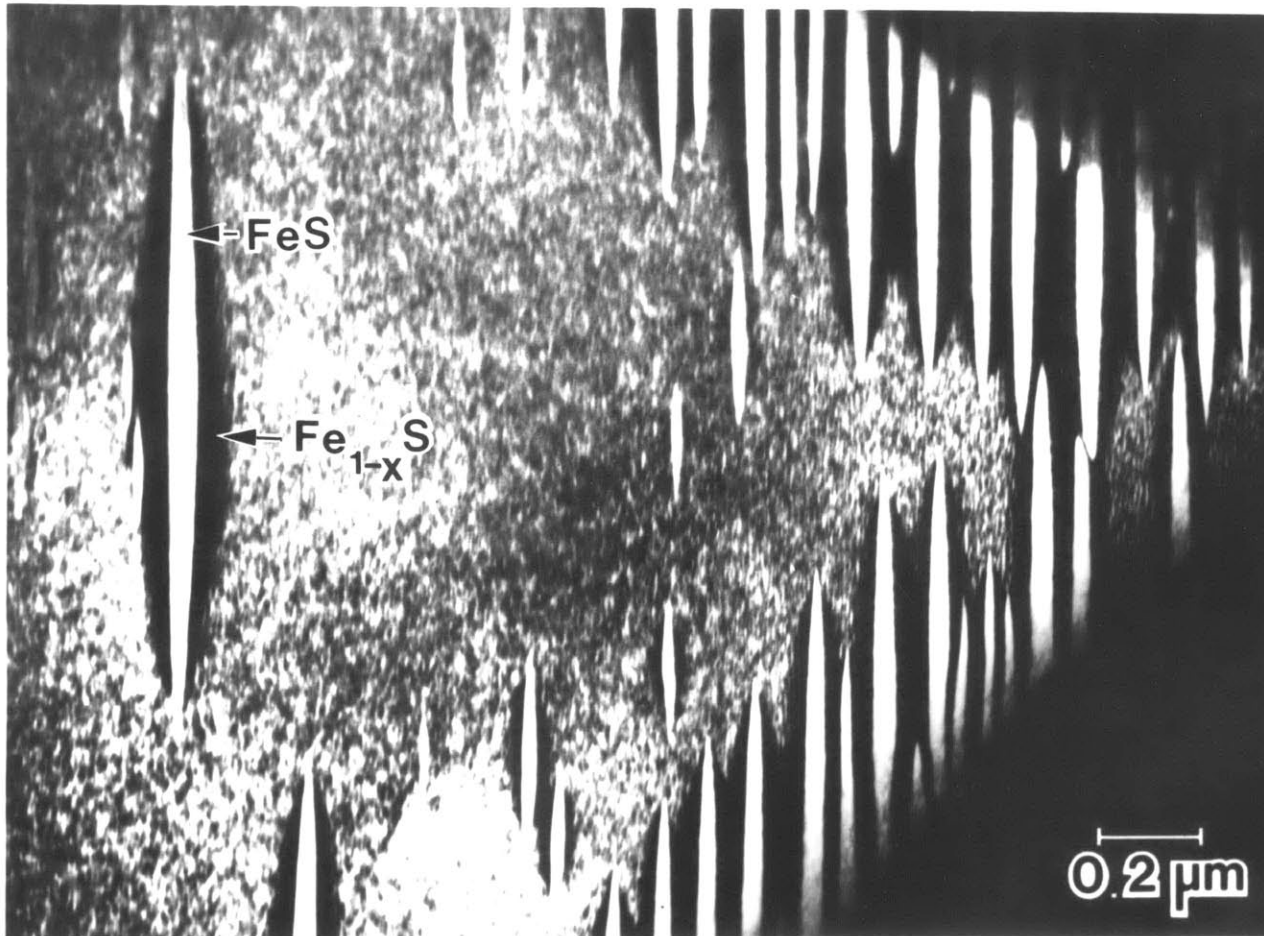
Figure 6.10. Microstructure of a mixture of FeS and $Fe_{1-x}S$. The sample was held at 363 K for ten minutes and then cooled to room temperature.
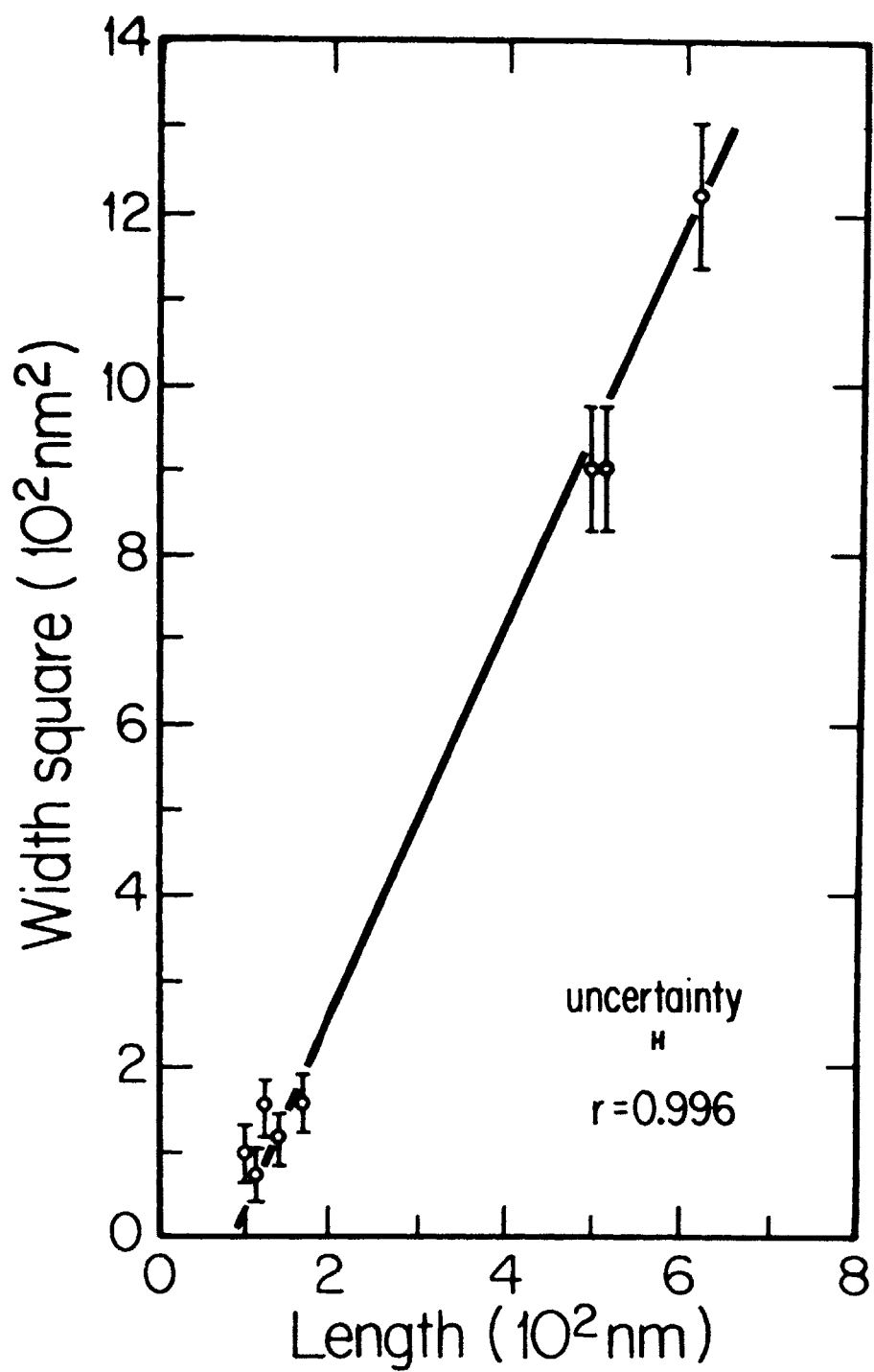
Figure 6.11. Square of maximum width of FeS precipitates versus their length.
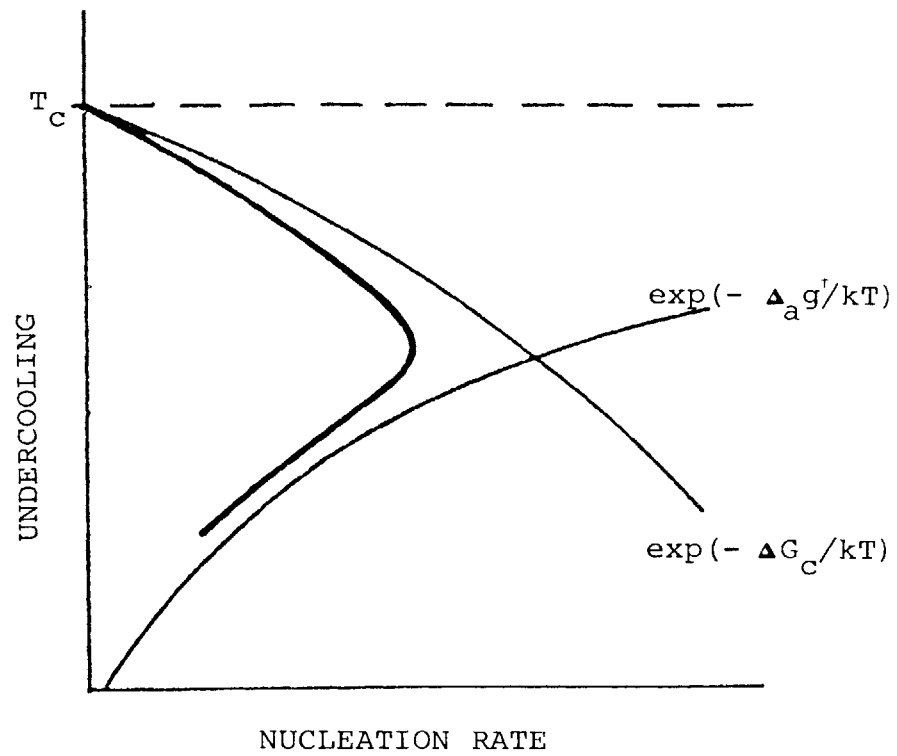
Figure 6.12. Schematic sketch of the rate of nucleation as a function of undercooling.

174
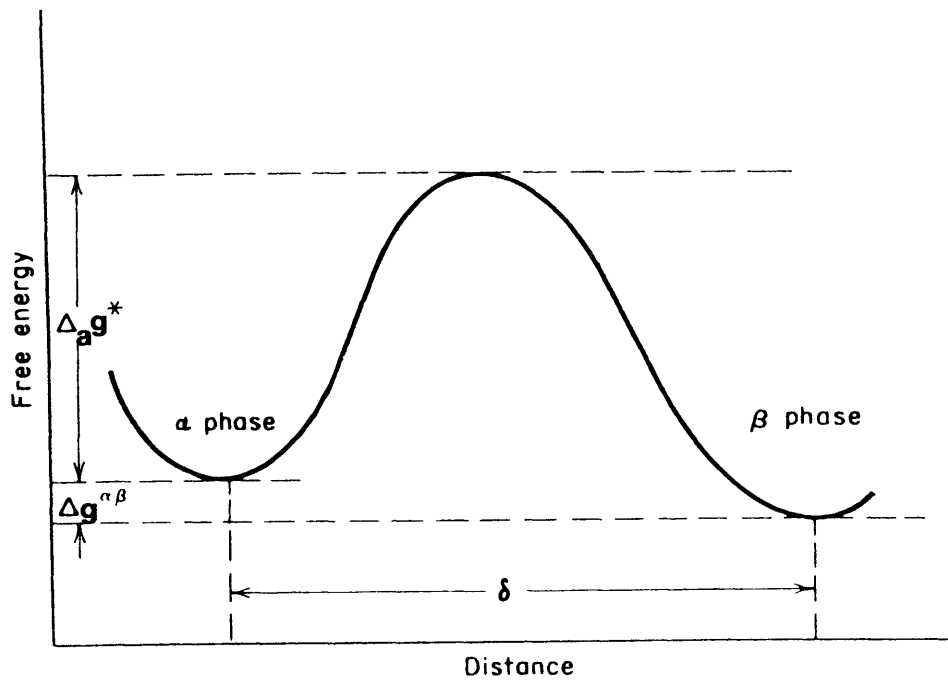
Figure 6.13. An activation energy barrier must be overcome when atoms move from α phase to β phase.
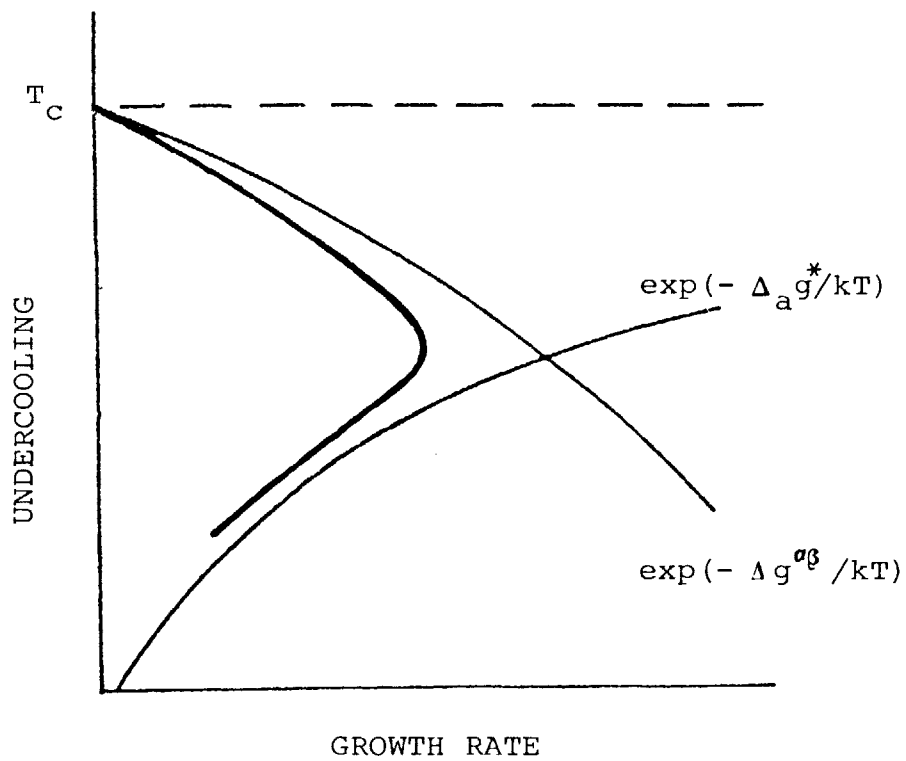
Figure 6.14. Schematic sketch of the rate of growth as a function of undercooling.
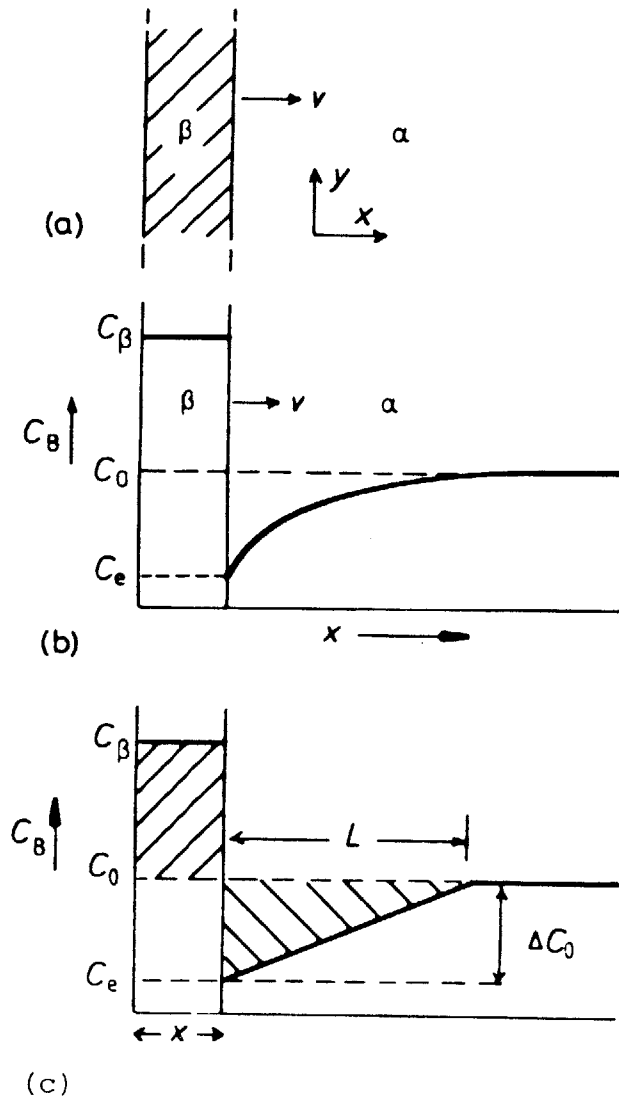
Figure 6.15. (a) diffusion-controlled thickening of a precipitate plate (b) concentration profile of a precipitate plate in a matrix (c) a simplification of the concentration profile (after Porter and Easterling, 1981).

Figure 6.16. Nucleation of FeS precipitates at undercoolings of (a) 24 K, (b) 37 K, (c) 44 K, (d) 92 K.
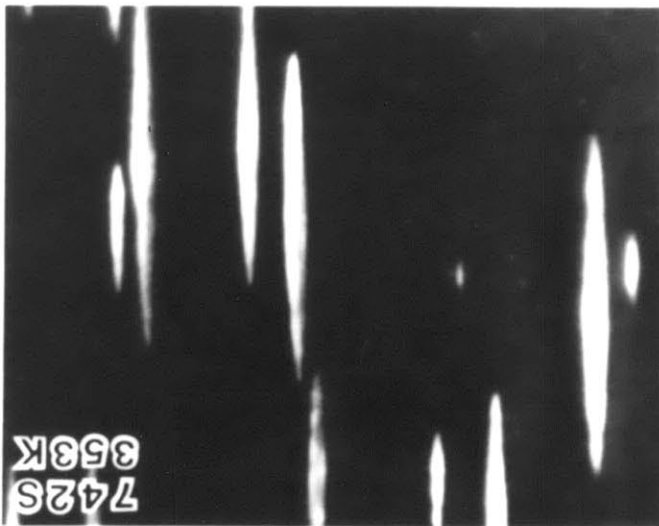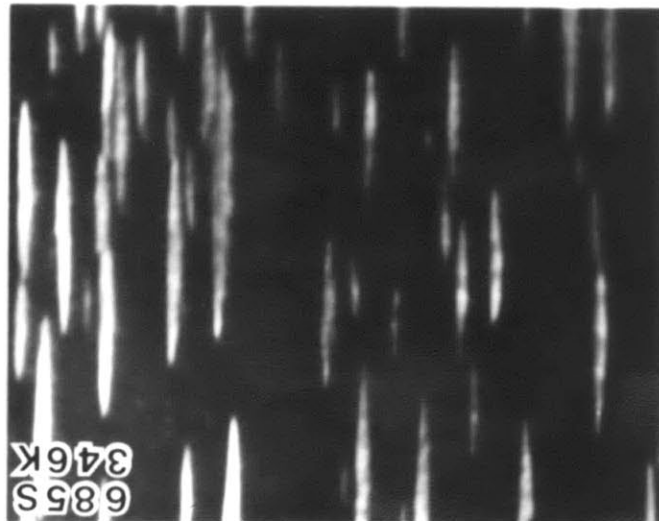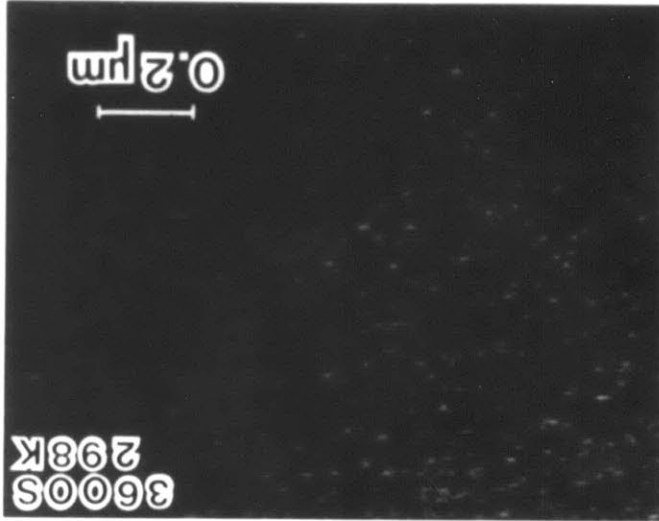
Figure 6.17. Growth of a FeS precipitate as a function of time at 366 K.

a	X seconds
b	X + 150 s
c	X + 380 s
d	X + 620 s
e	X + 860 s
f	X + 1170 s
g	X + 1470 s
h	X + 1830 s

0.4 µm
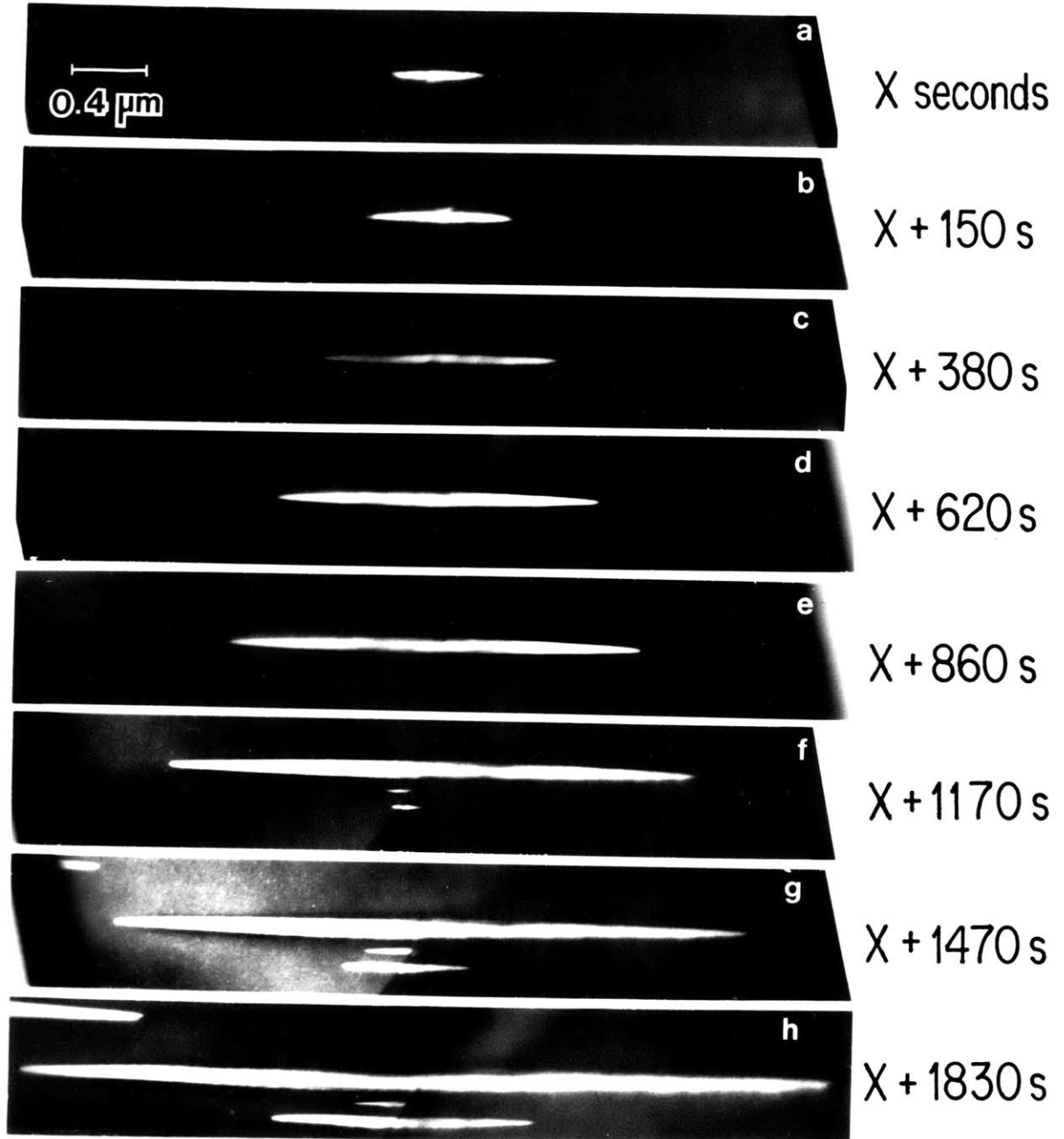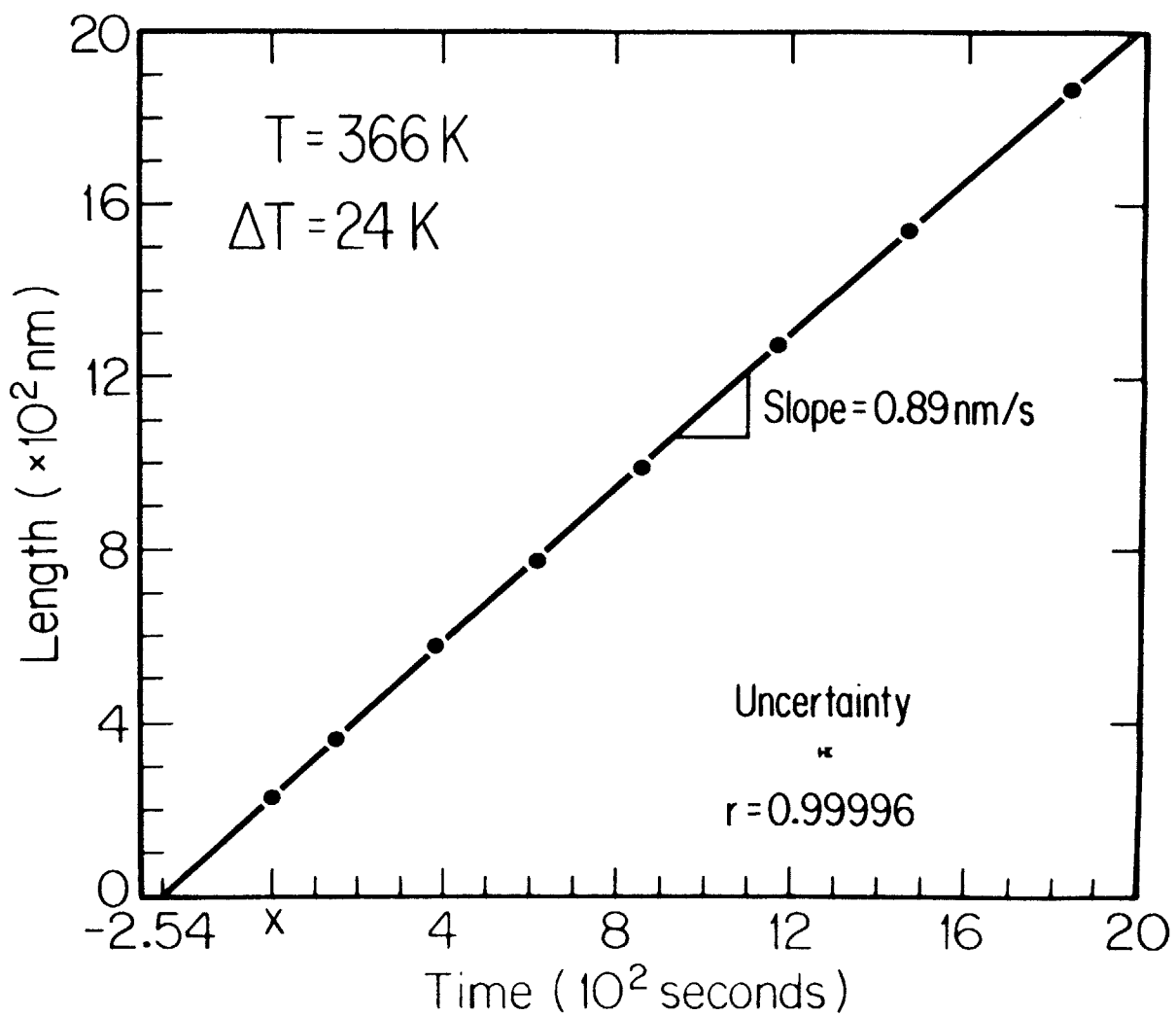
Figure 6.18. Length of a FeS precipitate versus time at 366 K.
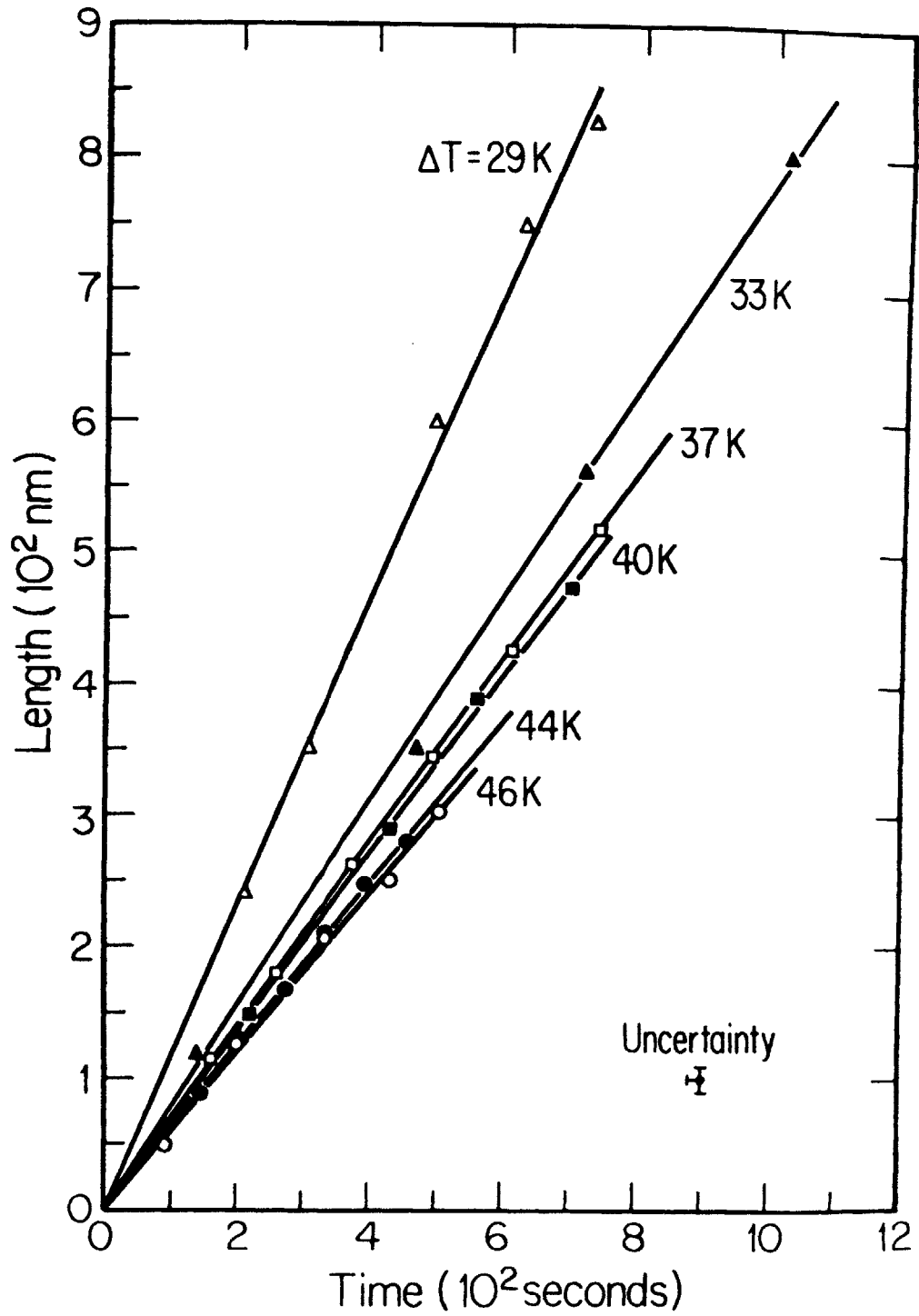
Figure 6.19. Length of FeS precipitates versus time at six different undercoolings.
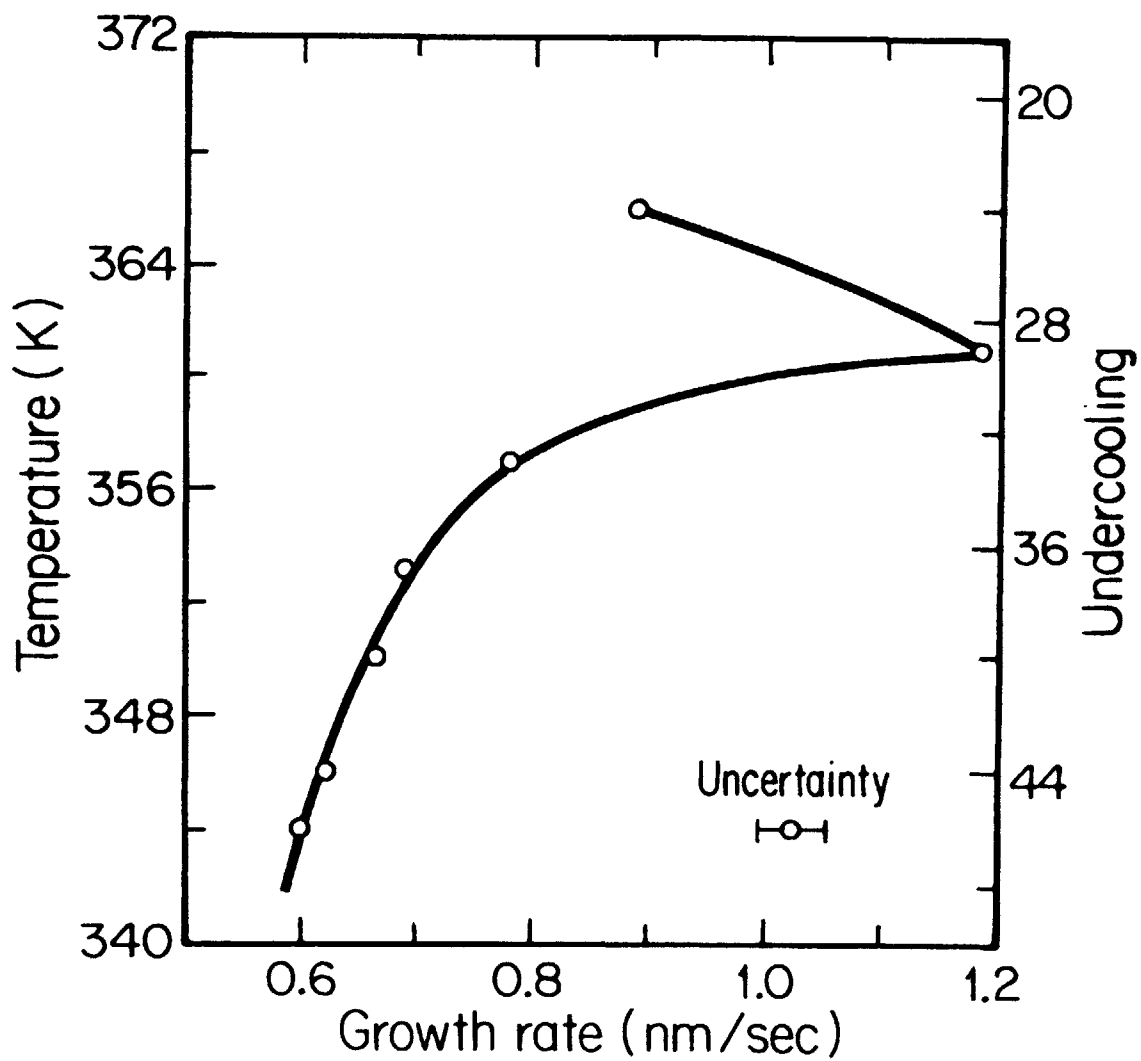
Figure 6.20. The rate of growth of length of FeS precipitates as a function of undercooling.
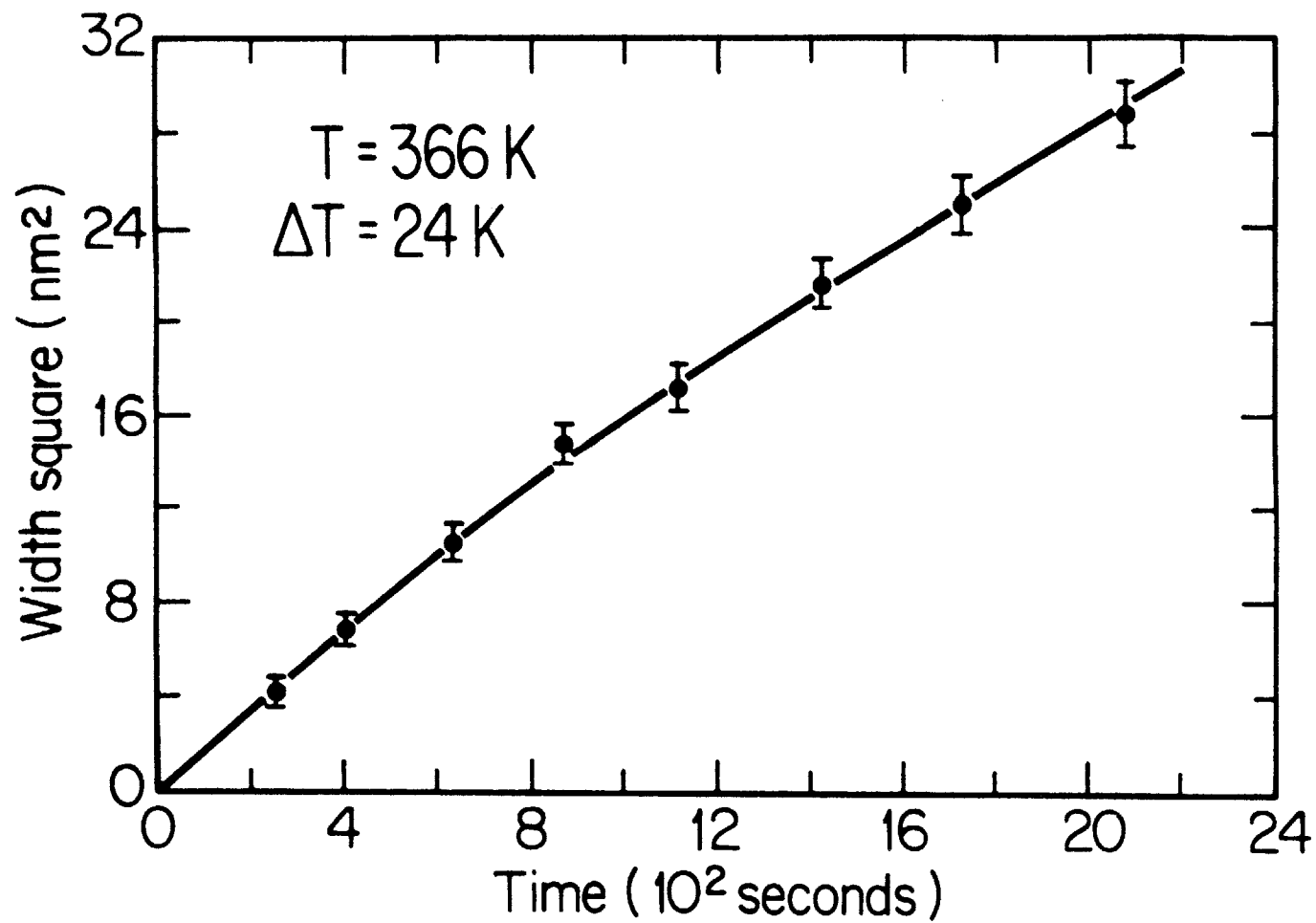
Figure 6.21. Square of maximum width of FeS precipitates as a function of time.
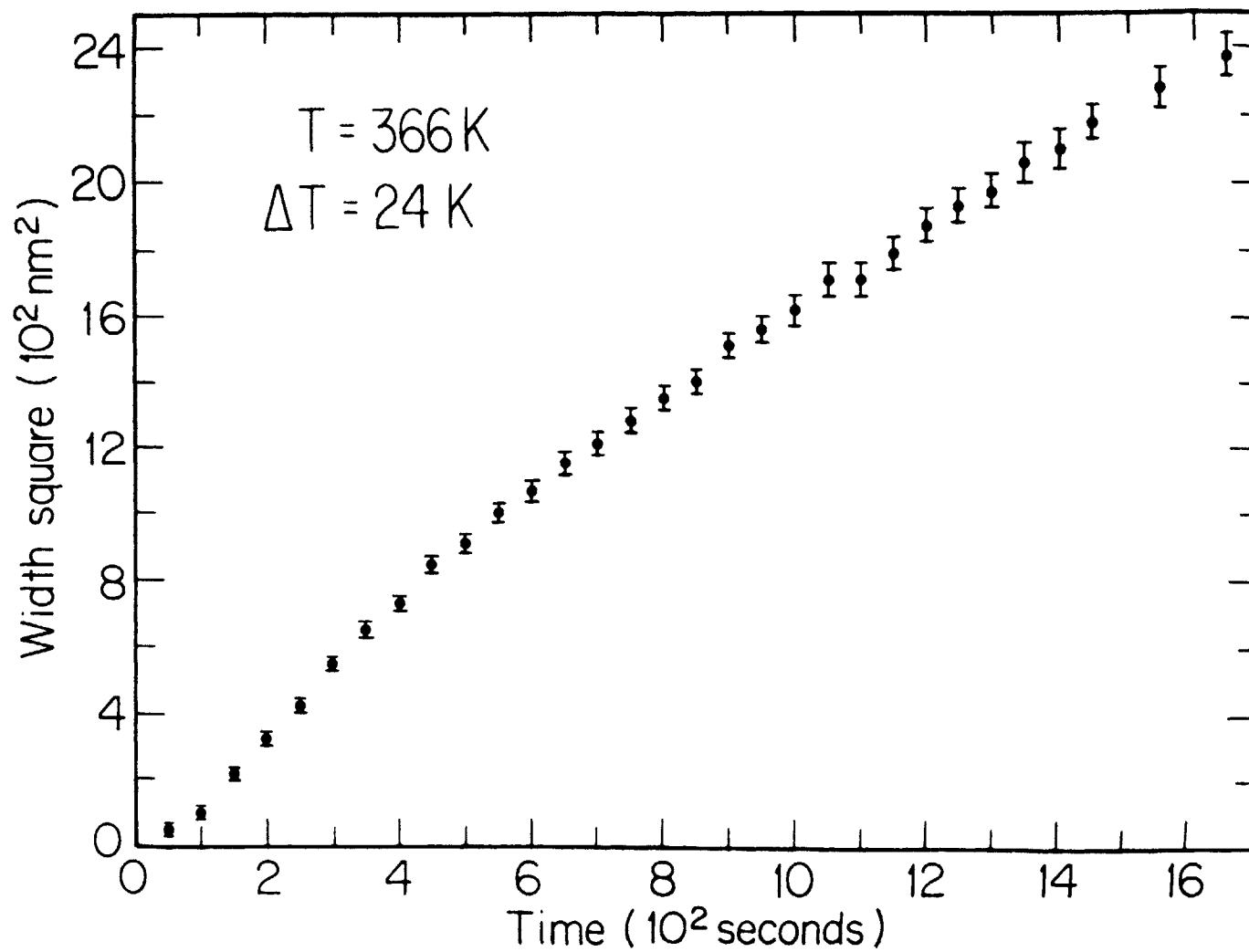
Figure 6.22. Square of width of FeS precipitate as a function of time.
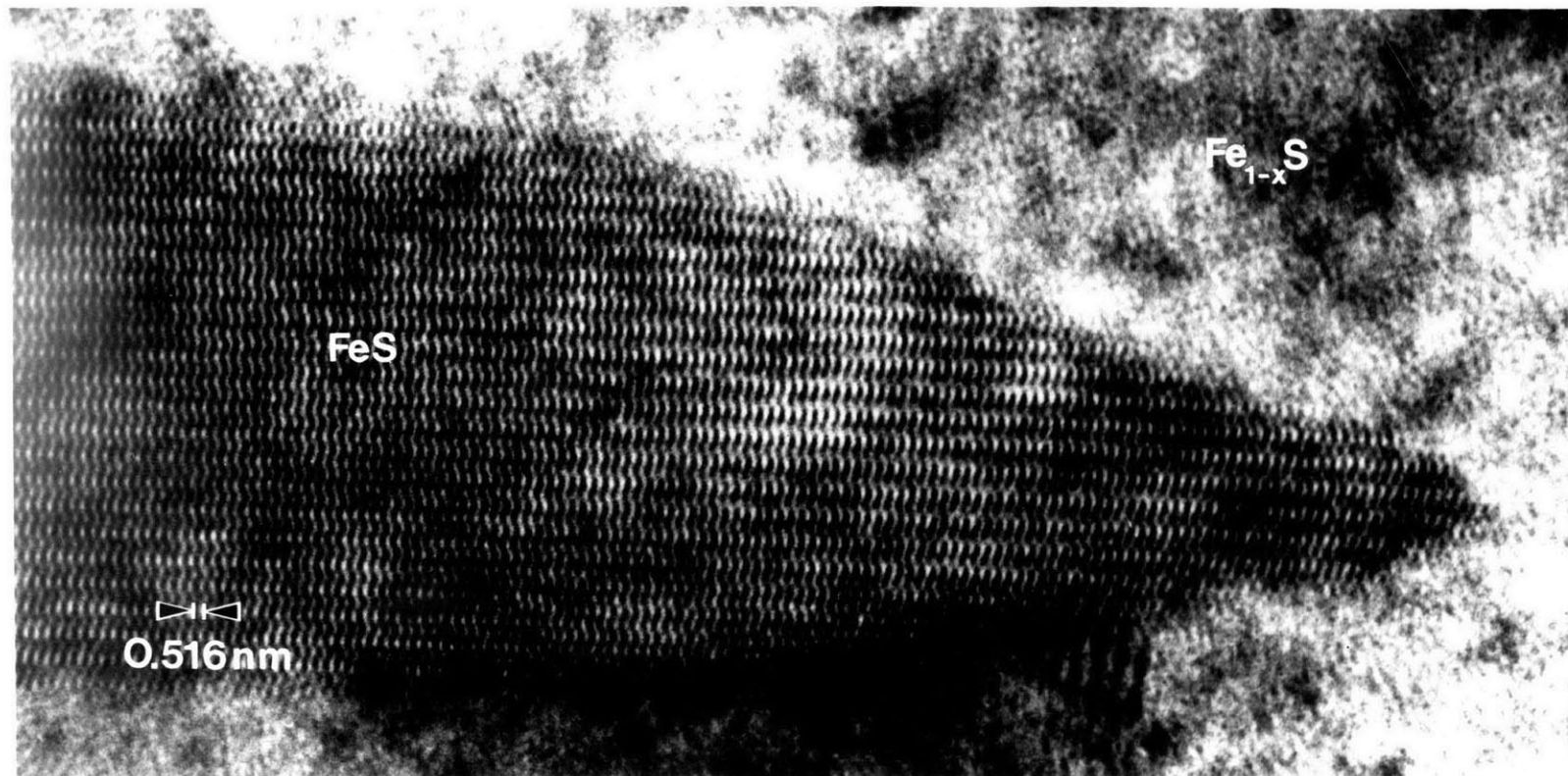
Figure 6.23. Lattice image of a FeS precipitate in $Fe_{1-x}S$ matrix (MIT JEM 200CX).
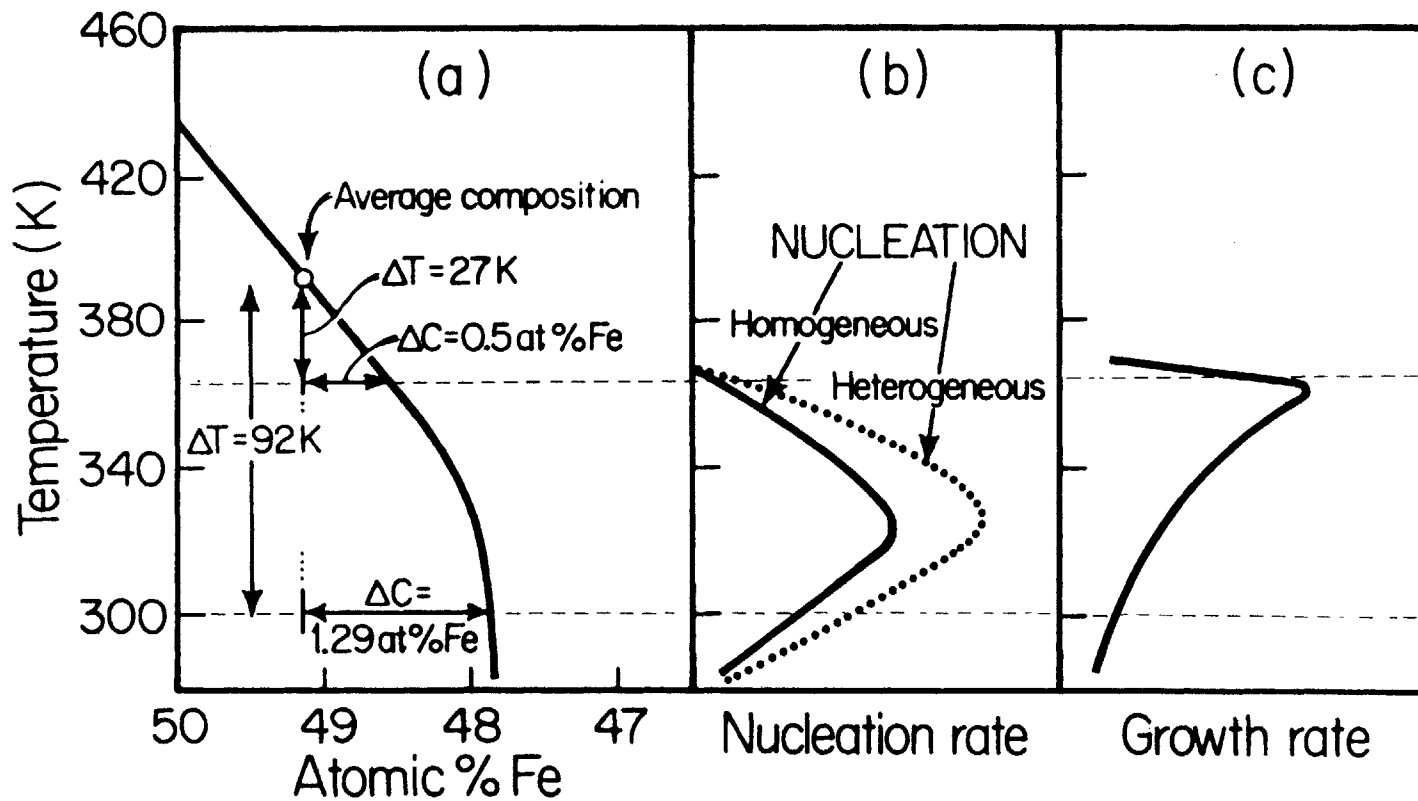
Figure 6.24. (a) undercooling and supersaturation prior to precipitation. Rates of (b) nucleation and (c) growth of FeS precipitates occurring during phase transformation.
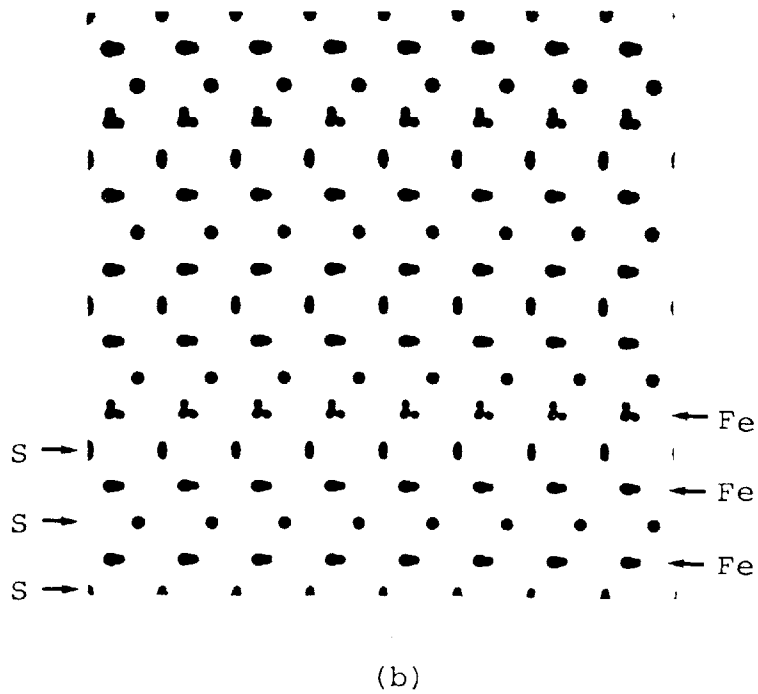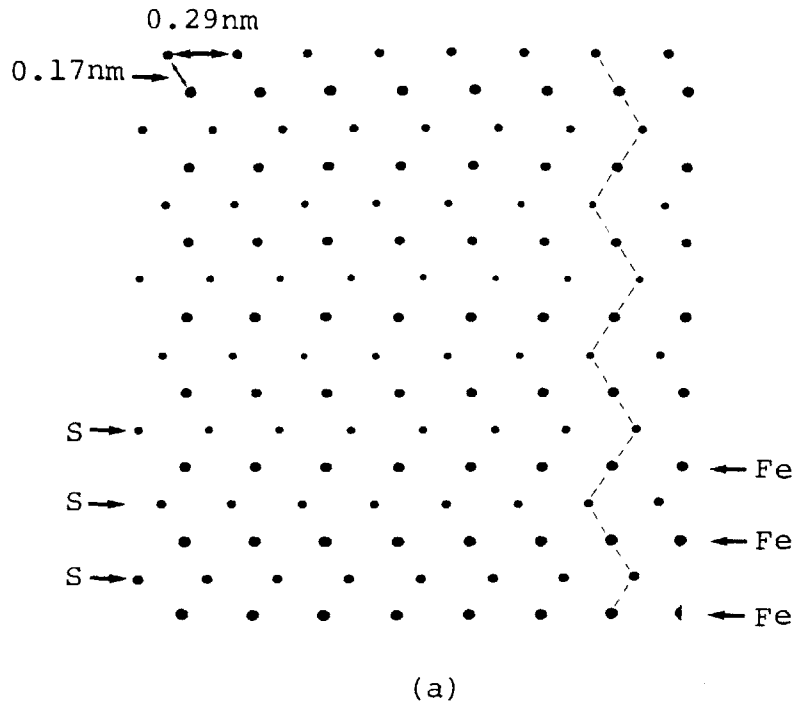
Figure 6.25. Projections of the (a) NiAs (1C) and (b) troilite (2C) structures along the [1$\bar{2}$10] direction.

Figure 6.26. A through-focus and through-thickness series of image simulation of troilite (2C) structure with the incident beam parallel to the $[120]\|[\bar{1}210]$ direction. The microscope parameters are those of the ASU JEM 4000EX.
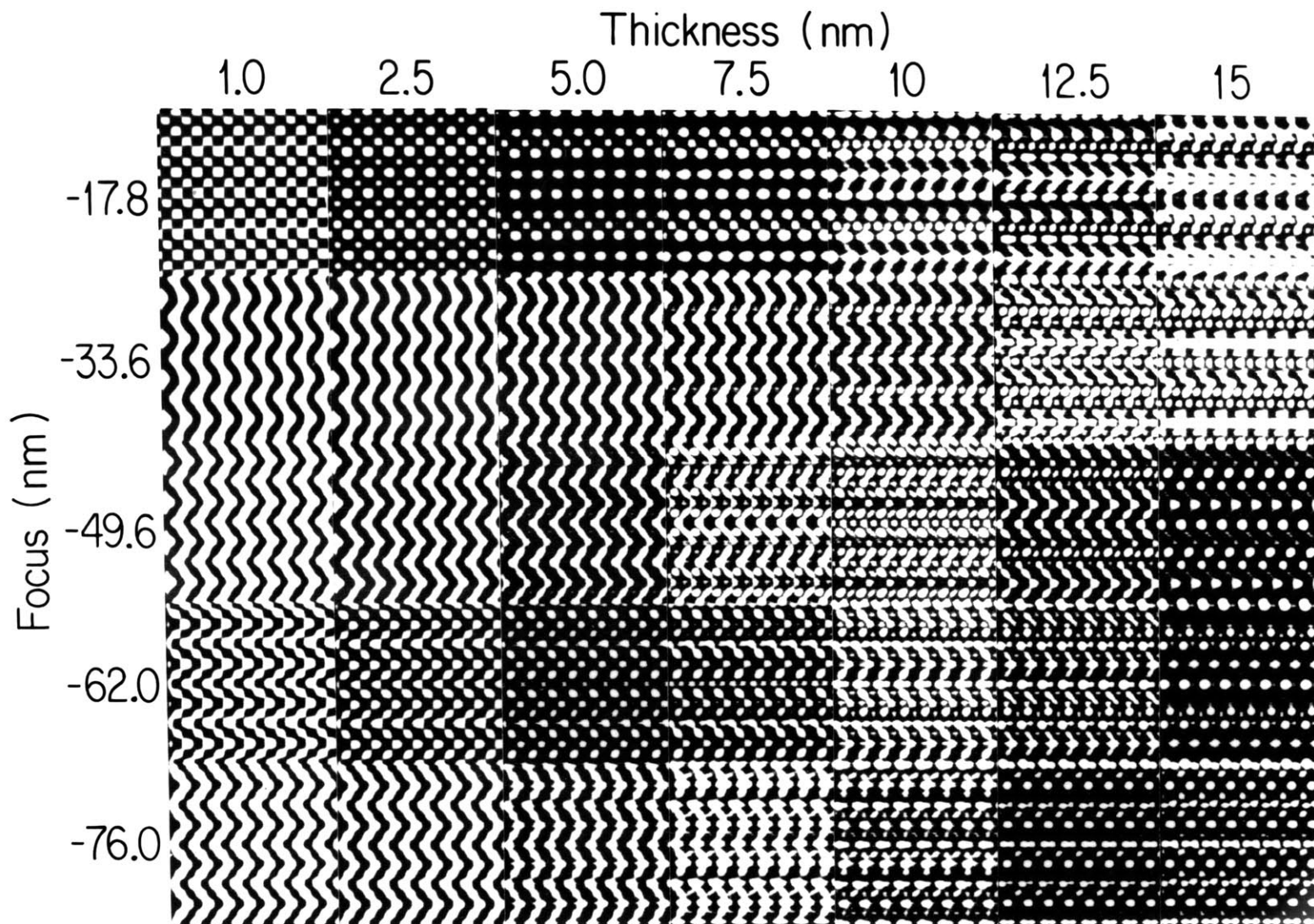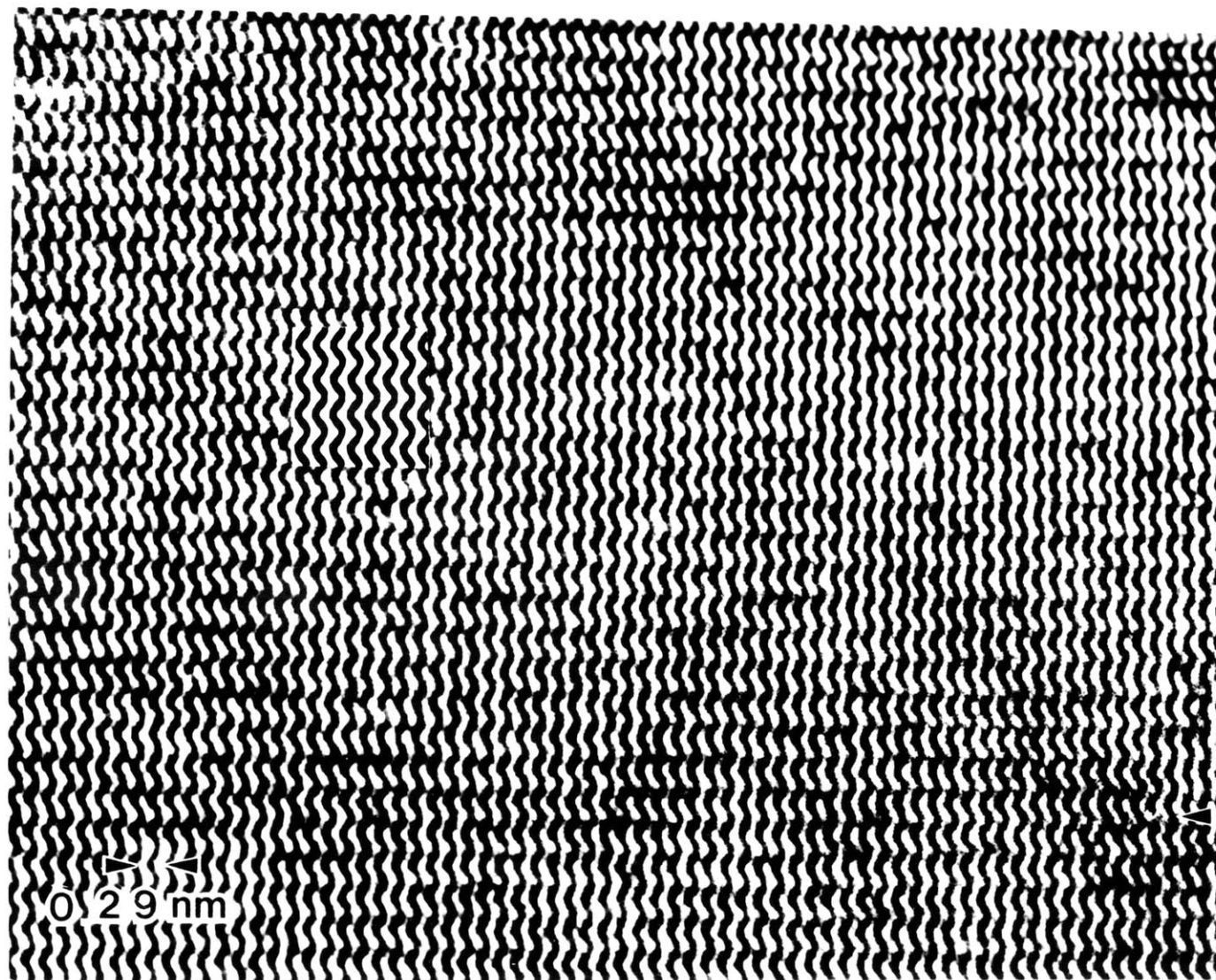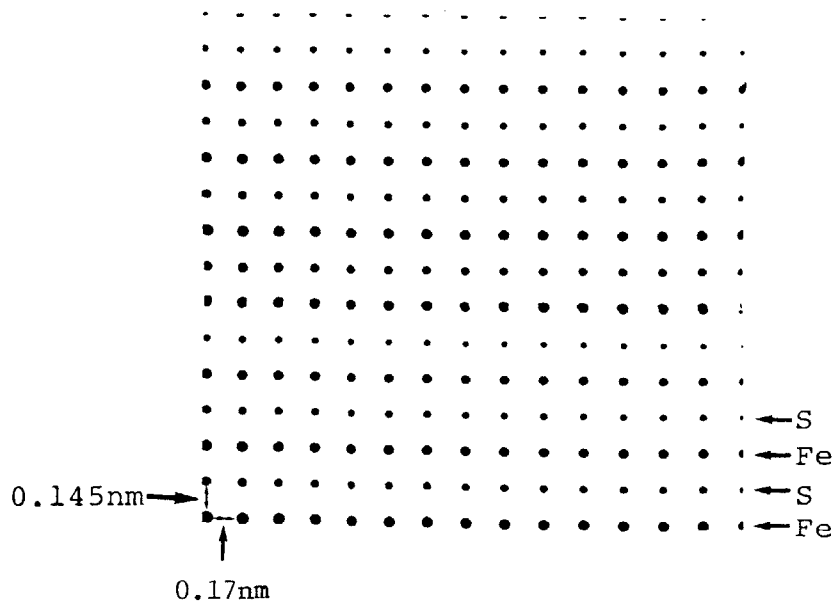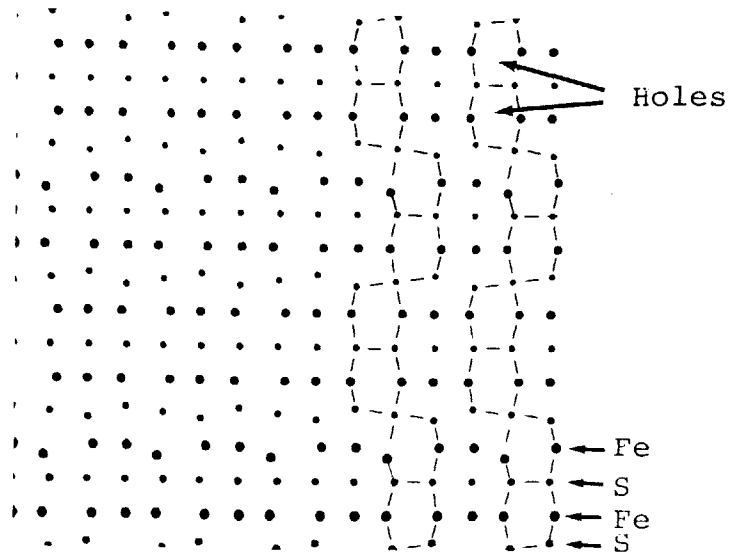
Figure 6.27. Lattice image of troilite with the incident beam parallel to the [120] | [1$\bar{2}$10] direction. Inset is calculated image with focus setting of -33.6 nm and 2.5nm thick (ASU JEM 4000EX).

0.29 nm

0.145nm →

0.17nm

(a)

Holes

(b)

Figure 6.28. Projections of the (a) NiAs (1C) and (b) troilite (2C) structures along the $[0\bar{1}10]$ direction.

Figure 6.29. A through-focus and through-thickness series of image simulation of NiAs (1C) structure with the incident beam parallel to the $[120] | [0\bar{1}10]$ direction. The microscope parameters are those of the ASU JEM 4000EX.
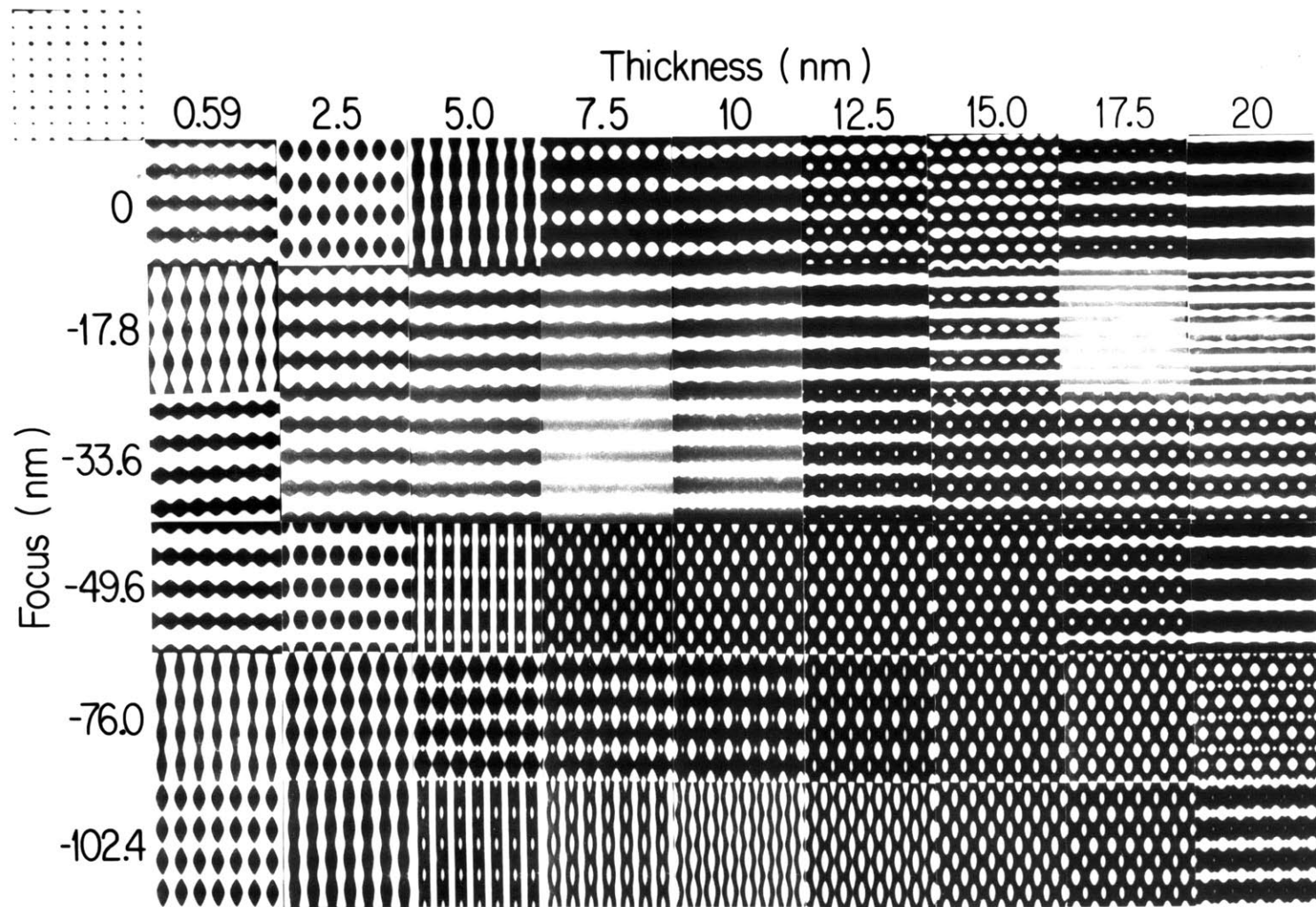
Thickness (nm)

Figure 6.30. A through-focus and through-thickness series of image simulation of troilite (2C) structure with the incident beam parallel to the $[100]|[0\bar{1}10]$ direction. The microscope parameters are those of the ASU JEM 4000EX.
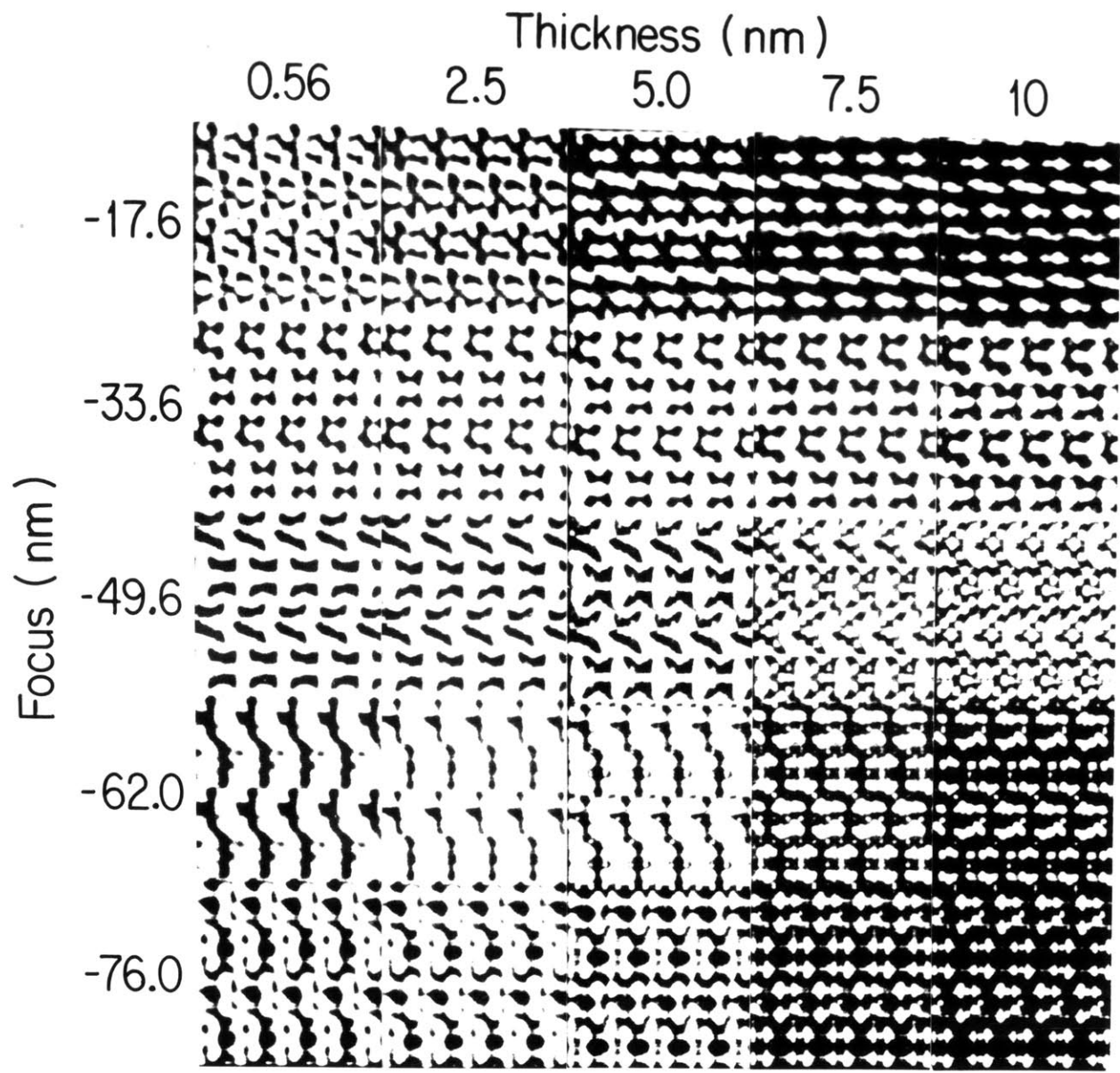
Thickness (nm)

0.56   2.5   5.0   7.5   10

Figure 6.31. A through-focus and through-thickness series of image simulation of troilite (2C) structure with the incident beam parallel to the $[100]|[0\bar{1}10]$ direction. The microscope parameters are those of the MIT JEM 200CX.
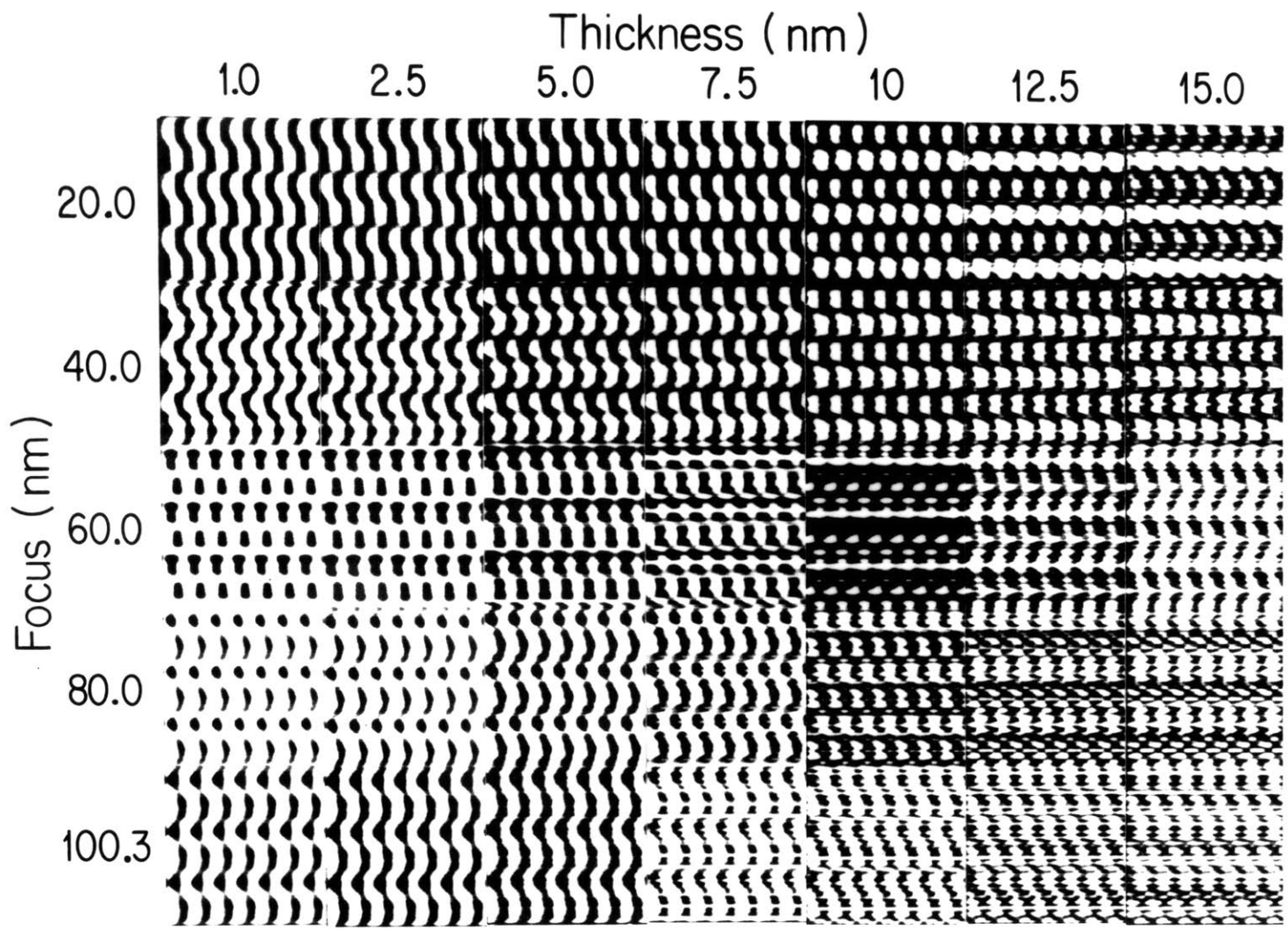
Figure 6.32. Lattice image of $Fe_{0.92}S$ (1C). The incident beam is parallel to the [1̄210] direction. Inset is calculated image of the 3C structure. (ASU JEM 4000EX)
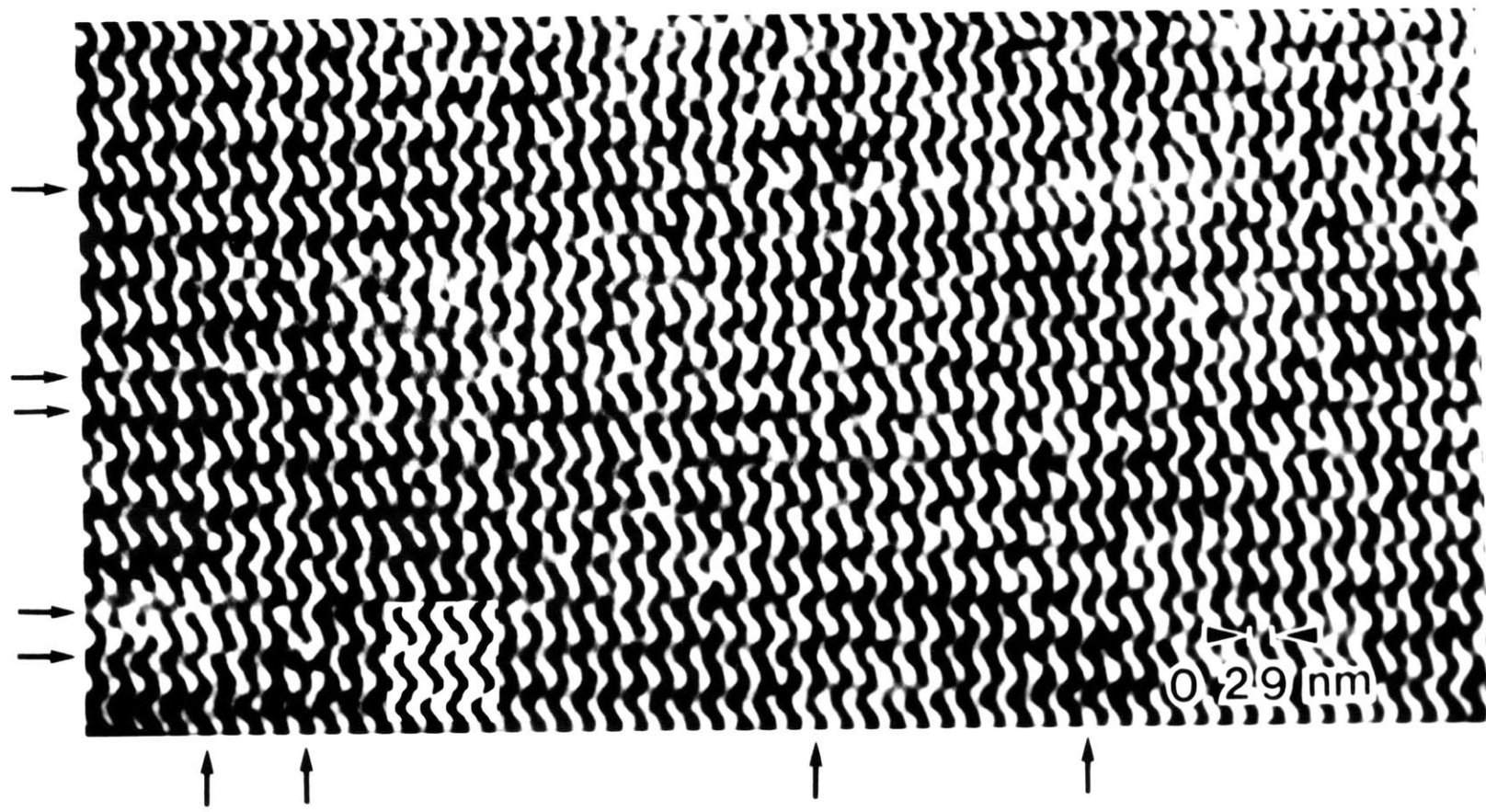
0.29 nm

Figure 6.33. Lattice image of FeS (2C) and $Fe_{0.92}S$ (1C). The incident beam is parallel to the [01̄10] direction. The coherent $FeS/Fe_{0.92}S$ interface is from an area near the tip of the FeS precipitate.
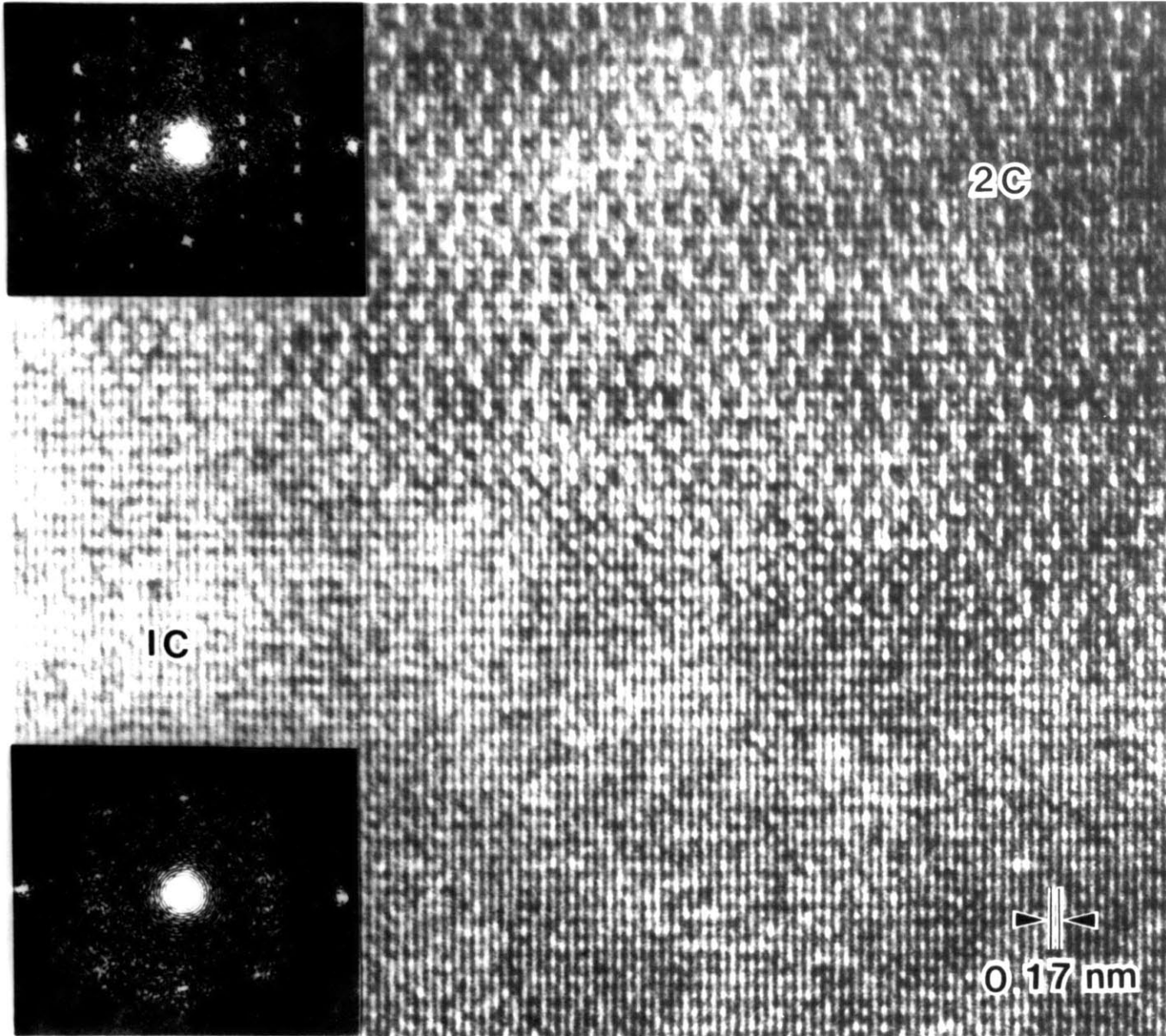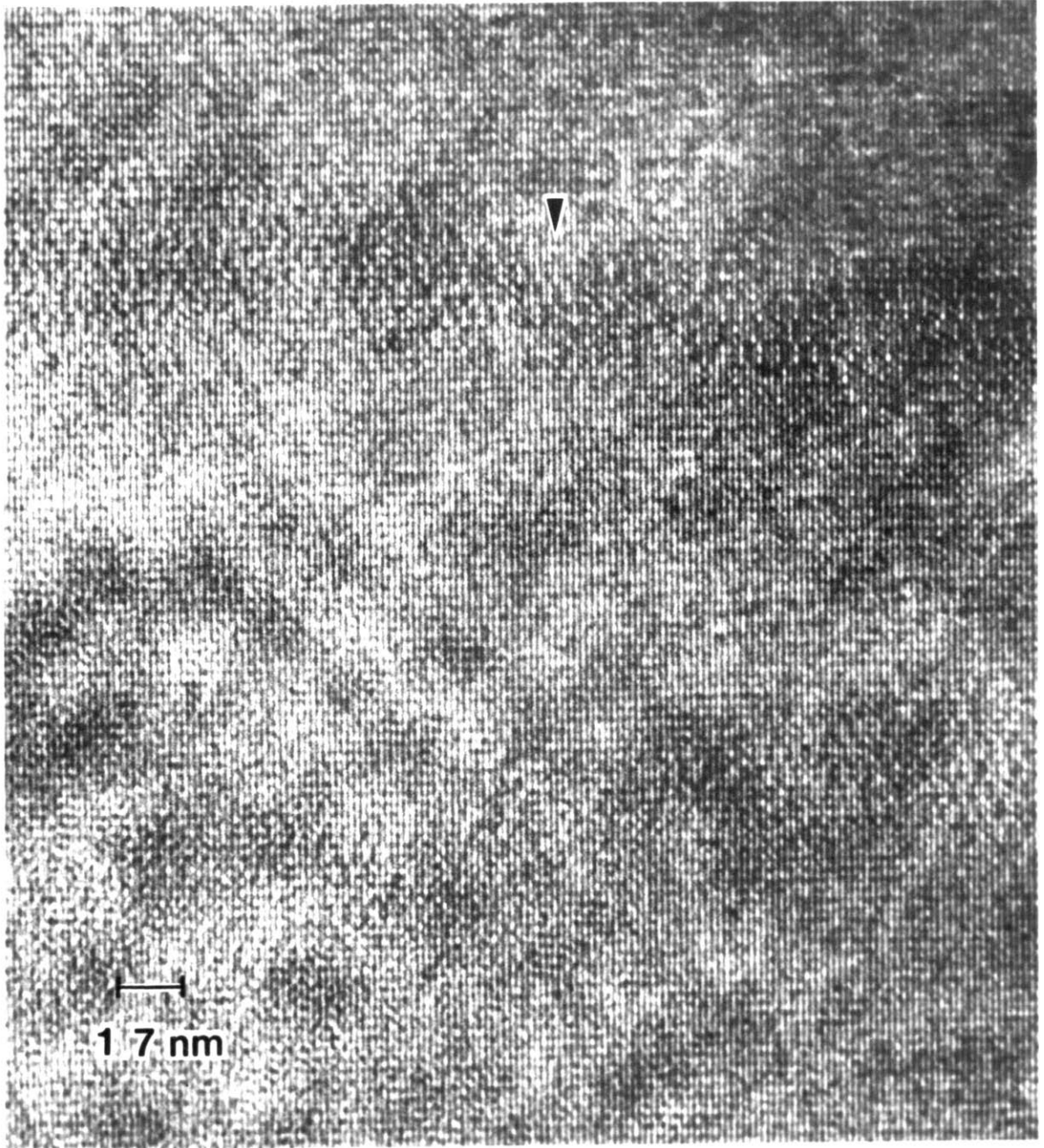
2C

IC

0.17 nm

Figure 6.34. Lattice image of a mixture of FeS and $Fe_{0.92}S$ showing very small FeS precipitates.
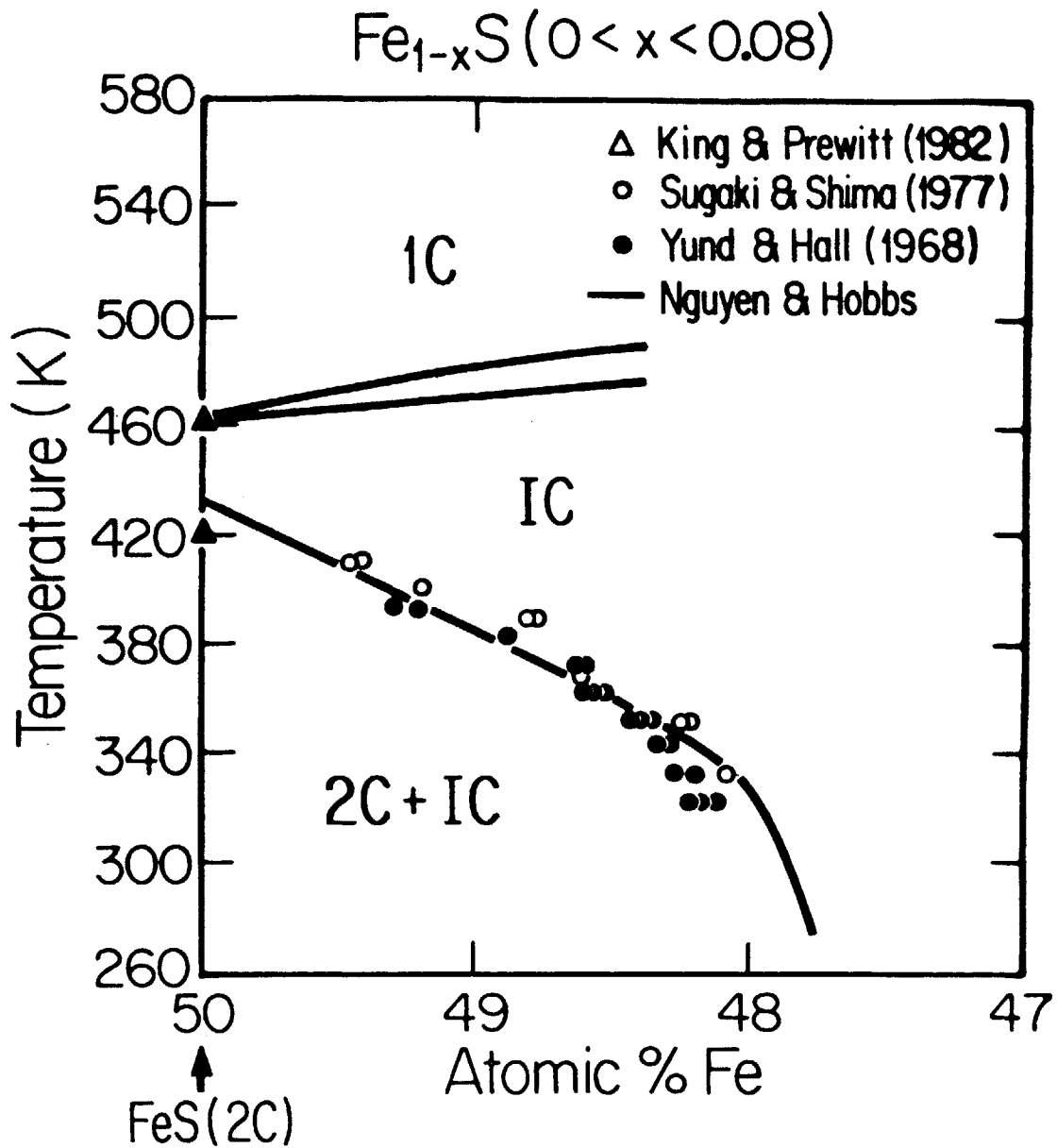
1 7 nm

Figure 6.35. The solvus separating the IC phase from the two-phase field (2C and IC) is in good agreement with those of Sugaki and Shima (1977) and Yund and Hall (1968).

References

Carpenter, R. H. and Desborough, G. A., Amer. Mineral. 49, 1350-1365 (1964).

Christian, J. W., The theory of Transformations in Metals and Alloys, 2nd ed., Pergamon, 1975.

Evans, H., Science 167, 621-623 (1970). 124-134 (1968).

King, H. E. and Prewitt, C. T., Acta Cryst. 38, 1877-1887 (1982).

Morimoto, N., Recent. Prog. Nat. Sci. Japan 3, 183-206 (1978).

Nakazawa, H. and Morimoto, N., Proc. Japan Acad. 46, 678-683 (1970).

Porter, D. A. and Easterling, K. E., Phase Transformation in Metals and Alloys, Van Nostrand Reinhold Company, New York, 1981.

Putnis, A., Phil. Mag. 31, 689-95 (1975).

Spark, J. T. et al., J. Phys. Soc. Japan 17 (Suppl. 1), 249 (1962).

Sugaki, A. and Shima, H., Tokohu Univ. Sci. Rept., ser 3, 13, 147-163 (1977).

Thiel, R. C., Phys. Stat. Sol. 40, K17 (1970).

Thiel, R. C., and Van den Berg, C. B., Phys. Stat. Sol. 29, 837 (1968).

Yund, K. A. and Hall, K. T., Mat. Res. Bull. 3, 779-784 (1968).

CHAPTER 7

PHASE RELATIONS, STRUCTURES AND DEFECT STRUCTURES OF $Fe_{1-x}S$, $0.08<x<0.125$

Results of chapter 7 will be reported at a later date. A portion of these results has been published in a paper by Nguyen and Hobbs (in Electron Microscopy of Materials, ed. W. Krakow, D. A. Smith and L. W. Hobbs, Mat. Res. Soc. Symp. Proc., 31, 291-302 (1984)).

CHAPTER 8

SUMMARY

The major conclusions of this work are:

1) the high temperature IC phase transforms into an $\underline{IC}$ phase at lower temperature. The phase transformation appears to be first order.

2) at T_α, the $Fe_{1-x}S$ $(\underline{IC})$ phase decomposes to FeS (2C) phase and an iron-poor $Fe_{1-x'}S$ $(\underline{IC})$ $(x < x')$ phase.

3) the $\underline{IC}$ phase has an incommensurate superstructure. The positions of the superstructure reflections vary with composition and temperature. The iron vacancies in the $\underline{IC}$ phase appear to order locally in the iron planes.

4) the phase separation mechanism of reaction $Fe_{1-x}S$ $(\underline{IC})$ -- FeS (2C) + $Fe_{1-x'}S$ $(\underline{IC})$ $(x < x')$ is nucleation and growth.

5) the growth rate of the length of FeS precipitates obey a linear rate law. The growth rate appears to be controlled by the interfacial reaction.

6) the growth rate of the side walls of FeS precipitates is linear initially and eventually becomes parabolic. The growth mechanism in the parabolic regime appears to be a diffusion-controlled reaction.

7) the dependency of the growth rate on undercooling agreed qualitatively with that predicted by the continuous growth model.

8) the $FeS/Fe_{1-x}S$ interface is coherent. The tip of the FeS precipitate is almost atomically sharp. Away from the tip, the $FeS/Fe_{1-x}S$ interface is smooth.

9) the "intermediate" pyrrhotite appear to be artifactual. The diffraction pattern of $Fe_{1-x}S$ that is undergoing a phase transformation is identical or similar to that of the "intermediate" pyrrhotite.

CHAPTER 9

SUGGESTION FOR FUTURE RESEARCH

The following suggestions arise from the results of this thesis:

1. The position of the solvus separating the 1C phase from the $\underline{IC}$ phase can be determined more accurately using high resolution x-ray diffraction.

2. The behavior of the superstructure reflections as a function of composition and temperature is a subject of considerable interest. High resolution x-ray diffraction should be used to study the incommensuration of the structure of $\underline{IC}$ phase. The quantative information on the positions and intensities of the superstructure reflections may lead to meaningful structural models of the incommensurate structures.

Biographical Sketch

The author was born in Bien Hoa, Viet Nam on July 24, 1958. He left Viet Nam on April 30, 1975 and came to the United State of America on July 1, 1975. He became an US citizen on November 19, 1981. The author finished his high school education at Xavier in New York City. He graduated fron Boston College in 1981 with a Bacholor of Science degree in Mathematics and Physics. In the fall of 1981, he entered the graduate school at MIT in the Department of Materials Science and Engineering. The author is presently a reserach staff member of the IBM Almaden Research Center.

Honors

Phi Betta Kappa.

Scholar of the College, Boston College 1981.

Presidential Scholar of the Elecron Microscopy Society of America, 1984.

IBM pre-doctoral fellow, 1985-1986.